SCANNING TRANSMISSION ELECTRON MICROSCOPY OF TAGGED PROTEINS IN WHOLE EUKARYOTIC CELLS

By

Madeline Jayne Dukes

Dissertation

Submitted to the Faculty of the

Graduate School of Vanderbilt University

in partial fulfillment of the requirements

for the degree of

DOCTOR OF PHILOSOPHY

in

Chemistry

May, 2011

Nashville, Tennessee

Approved:

Dr. Darryl J. Bornhop

Dr. Niels de Jonge

Dr. B. Andes Hess

Dr. David W. Piston

Dr. Sandra J. Rosenthal

Dedicated to:

My parents, Larry W. Clark and Victoria L. Whitesell-Clark

ACKNOWLEDGEMENTS

I am very grateful to my advisors Dr. Niels de Jonge and Dr. Darryl Bornhop for their guidance during my graduate studies. Niels, thank you so much for taking me on as your full time student, and thus giving me the opportunity to pursue electron microscopy research, as well for the energy, enthusiasm, and time that you have invested in mentoring, and developing me as a scientist. I would also like to thank the other members of my committee: Dr. David Piston, Dr. Sandra Rosenthal, and Dr. B. Andes Hess for their time and guidance during the course of my research.

I am of course enormously grateful to the members of the de Jonge lab, Dr. Diana Peckys, Dr. Ranjan Ramachandran, Dr. Jean-Pierre Baudoin, and Elisabeth Ring for their contributions, help, and support in my research. I am also indebted to the members of the Bornhop group, particularly Dr. Bernard Anderson, Dr. Lynn Samuelson, Nancy Tiller.

I would also like to thank Steve Head and Dr. Gertjan Kremers, and Dr. Jay Jerome for his invaluable guidance in regards to biological electron microscopy.

To my undergraduate professors, specifically: Dr. Stephen Hudson, Dr. Rebecca Hanckel, Dr. A.K. Bonette, Dr. Jeryl Johnson, Dr. Todd Ashby, and Dr. Timothy Saxon, thank you for providing me with your guidance and encouragement.

I would like to thank my family and friends for their support and encouragement. First my husband, Albert, you are decidedly the best “perk” of graduate school, thank you for keeping me sane, proof reading the many documents I’ve given you, letting me bounce my ideas off you, and for feeding the pets in the morning so that I can have those fifteen extra minutes of sleep! You are the best! Mom and Dad, thank you for all the

time (and money) you invested in my education. Without you I would not be where I am today. Albert and Pinkey Dukes, thank you so much for all of your love and encouragement.

Finally I would like to thank the funding sources and institutions that made this work possible: Vanderbilt University Department of Chemistry, Vanderbilt University School of Medicine, Vanderbilt Institute of Chemical Biology, National Institute of Health: R01-GM081801, VUMC Cell Imaging Shared Resource (supported by NIH grants CA68485, DK20593, DK58404, HD15052, DK59637 and EY08126), Protochips Inc for liquid specimen holder and silicon microchips, Laboratory Directed R&D Program of Oak Ridge National Laboratory (ORNL,) and The SHaRE User Facility, which is sponsored by the Division of Scientific User Facilities, Office of Basic Energy Sciences, U.S. Department of Energy.

LIST OF TABLES

LIST OF FIGURES

LIST OF SYNTHETIC SCHEMES

LIST OF ABBREVIATIONS

2D ....Two-Dimensional

3D ....Three-Dimensional

ADF .... Annular Dark Field

BSA .... Bovine Serume Albumin

CCD ....Charge Coupled Device

CLEM .... Correlative Light and Electron Microscopy

CPD .... Critical Point Dryer

DIC .... Differential Interference Contrast

DMEM ....Dulbecco's Modified Eagle Medium

DMSO .... Dimethyl Sulfoxide

DNA..... .....Deoxyribonucleic Acid

DO3A..... .....1,4,7,10-tetraazacyclododecane-1,4,7- triacetate

DO3A..... ..... 1,4,7,10-tetraazacyclododecane-1,4,7,-triacetic acid

DOTA ....1,4,7,10-tetraazacyclododecane-1,4,7,10-tetraacetic acid

EGF..... ..... Epidermal Growth Factor

EGFR .... Epidermal Growth Factor Receptor

EM ....Electron Microscope/Microscopy

FP..... ..... Fluorescent proteins

FWHM .... Full Width Half Max

HMDS..... .....Hexamethildisalazane

HPLC ....High Performance Liquid Chromotography

LM ..... Light Microscopy

MI ..... Molecular Imaging

NIR ..... Near Infrared

NMR ..... Nuclear Magnetic Resonance

PALM ..... Photoactivated Light Microscopy

PBS ..... Phosphate Buffered Saline

PLE ..... Photoluminescence Excitation

PSF..... Point Spread Function

QD ..... Quantum Dot

QY ..... Quantum Yield

SEM..... Scanning Electron Microscope/Microscopy

SiN..... Silicon Nitride

SNR ..... Signal to Noise Ratio

STED ..... Stimulated Emission Depleted Microscopy

STEM..... Scanning Transmission Electron Microscope/Microscopy

STORM..... Stochastic Optical Reconstruction Microscopy

tbuDO3A..... tri-tert-butyl 1,4,7,10-tetraazacyclododecane-1,4,7- triacetate

TEM..... Transmission Electron Microscope/Microscopy

TFA..... Trifluoroacetic Acid

UV ..... Ultraviolet

Z..... Atomic Number

TABLE OF CONTENTS

Page

CHAPTER I

INTRODUCTION AND BACKGROUND

> "For the limits to which our thoughts are confined, are small in respect of the vast extent of Nature itself; some parts of it are *too large* to be comprehended and some *too little* to be perceived. And from thence it must follow, that not having a full sensation of the Object, we must be very lame and imperfect in our conceptions about it, and in all the propositions which we build upon it; hence we often take the *shadow* of things for the substance, *small* appearances for *good* similitudes, *similitudes* for *definitions*; and even many of those which we think to be the most solid definitions, are rather expressions of our own misguided apprehensions then of the true nature of the things themselves. ....."
>
> -- Robert Hooke, *Micrographia*, 1665

1.1 Imaging biological systems

Establishing the reliability, or the accuracy, with which an image represents its subject, is a fundamental concern in all disciplines of microscopy.[1-4] Microscopy of biological systems is particularly challenging due to the complexities and interdependence of the individual components.[5,6] The role that an individual macromolecule or protein performs cannot be fully realized outside the context of its native environment.[6-10] Thus, in order to develop an accurate understanding of such cellular function it is necessary to elucidate the distribution and organization of the protein and surrounding assemblies which form the machinery of the cell. Although, in the ideal circumstances, images would be obtained without perturbing the subject or its environment, this is not typically feasible. Biologically specific labels or tags, such as fluorescent dyes or nanoparticles must be introduced to render the subject of interest visible. Cellular processes must be immobilized prior to imaging—either by

freezing[6,11,12] or chemical fixation,[3,5,13,14] which can lead to the formation of artifacts. In addition, many microscopy techniques require additional sample processing to withstand the radiation necessary to record an image. Such processing alters the sample's native state, and increases the potential for artifacts or distortions within the sample.[7,15] Thus, in order to elucidate what Robert Hooke termed as "the true nature of things," in a biological system it is necessary to develop new imaging methodologies that maintain or closely preserve a sample's native state while providing a resolution of a few nanometers.

The requirements for imaging cellular systems are dictated by the system or subject to be imaged. Ideally, in order to image a system under its native conditions, the microscopy technique employed would fulfill all eight of the requirements listed in Table 1; however, current microscopy methods meet these requirements at the expense of resolution.[16]

Table 1: Imaging Requirements[16]

1	3D imaging
2	In natural liquid environment, i.e., not frozen
3	Single particles, i.e., no crystals
4	Protein assemblies
5	Time-resolved
6	Intracellular, not only surface
7	Reproducibility
8	Fast imaging

This trend, shown in Figure 1, highlights the decline in resolution as more of the requirements in Table 1 are realized by given microscopy techniques. For instance, although light microscopy (LM), meets the most requirements, it has the poorest

resolution (≥ 200 nm). Conversely, although X-ray crystallography obtains angstrom (Å) resolution, it is restricted to crystallized specimens and is therefore not a viable candidate for to image proteins in their native, cellular environment. Additionally, as the number of requirements that a technique fulfills decreases, the more severe is the change in the sample relative to its native state. Thus, new methodologies are needed to fill the gap in resolution and imaging requirements in order to image individual proteins under biologically relevant conditions.

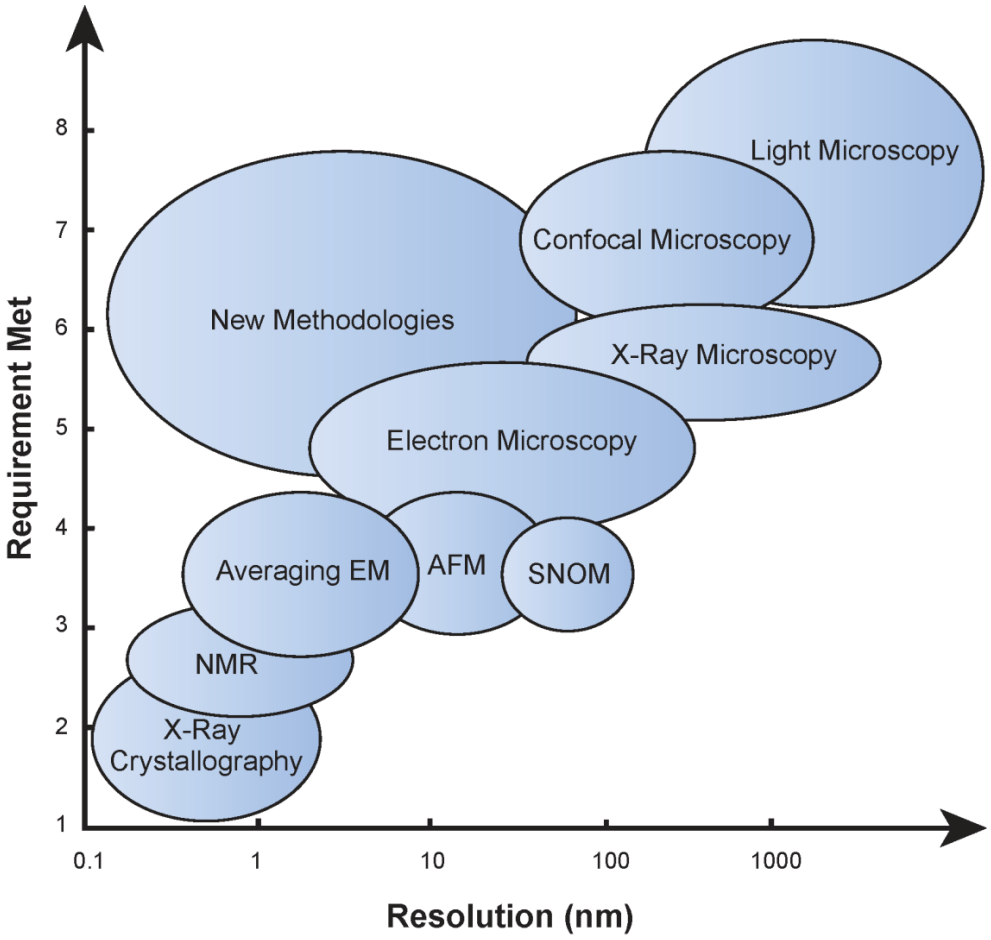

Figure 1: Resolution versus parameters for conventional imaging/microscopy techniques. In general, techniques which meet larger a number of imaging parameters have lower resolution. Adapted from de Jonge *et. al.* [16]

1.2 Resolution

The obtainable resolution of LM is inherently limited by diffraction. The diffraction limit, (d_{min}), described by Ernst Abbe, shown in equation **1,** defines the minimum lateral distance between two objects that is necessary to be able to resolve them,[17] where λ_0 is the wavelength of light in a vacuum and NA stands for the numerical aperture of the condenser and objective lenses.[17,18] In practice the diffraction limit be may be approximated as $\lambda / 2$.

$$d_{min} = \frac{1.22\lambda_0}{NA_{obj} + NA_{cond}} \approx \frac{\lambda}{2} \qquad (1)$$

Because ultraviolet (UV) light due damages biological specimens, and typically requires impractical optics, longer wavelengths ($\geq$ 400 nm) are typically employed in LM. Thus diffraction limits the obtainable resolution of LM techniques to ~ 200 nm and above.[2,19]

The resolution of LM can be improved through super-resolution techniques[19-23] such as photoactivated localization microscopy (PALM),[24-27] stochastic optical reconstruction microscopy (STORM),[28-31] which determine the position single particles (*i.e*. fluorescent dye or protein) with high precision, as well as stimulated emission depletion (STED), which selectively quenches fluorophores, thus constricting the centroid of the signal.[19,32-36] These methods yield resolutions of 50 nm, or as high as 10-20 nm for extended imaging times. Essentially, resolution is improved at the expense of imaging speed, and the number of features which can be imaged in a single

sample is restricted due to the limited availability of fluorophores with suitable optical properties and resistance to photobleaching.[37]

Unlike LM, which utilizes photons to image an object, electron microscopy uses electrons to form the image, and is thus capable of attaining sub-angstrom (Å) resolution. The wavelength (λ_0) of an electron can be calculated using de Broglie's hypothesis, shown in equation **2**, where h is Planck's constant, m_0 is the mass of the electron at rest, v is the velocity of the electron, and c is the speed of light in a vacuum.

$$\lambda = \frac{h}{m_0 v}\sqrt{1 - \frac{v^2}{c^2}} \qquad (\mathbf{2})$$

Thus, for a 100 keV electron, its corresponding wavelength is 4 pm.[1] Because the wavelength of an electron is approximately 5 orders of magnitude smaller than a wavelength of light, the theoretical limit of diffraction for an electron microscope is 0.02 Å. However, due to lens imperfections, this limit has not been achieved with current electron microscopes, and the actual resolution is much lower, closer to 1Å.[1]

1.3 Principles of Electron Microscopy

1.3.1 The Electron Microscope

The electron microscope was developed in 1931 by Ernst Ruska.[38] Generalized schematics of two types of electron microscopes, the transmission electron microscope and the scanning electron microscope are shown in Figure 2.

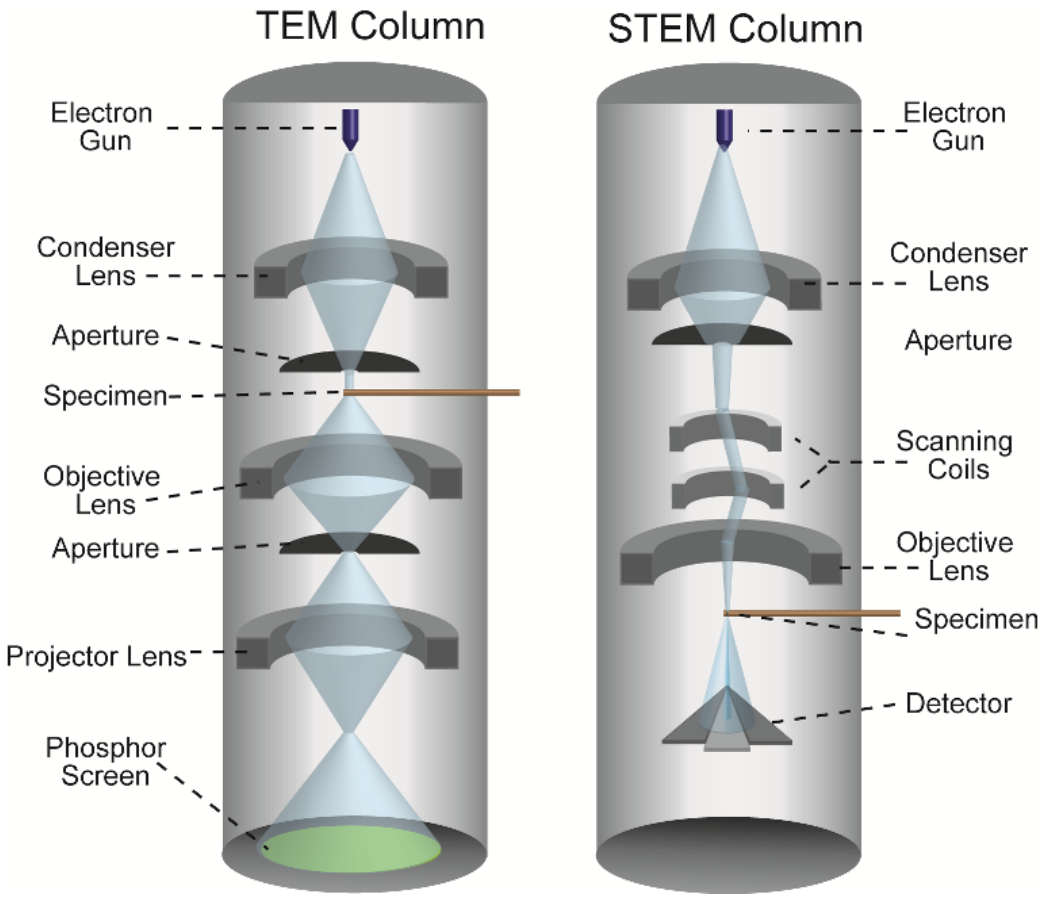

Figure 2: Schematics comparing the electron beam paths (blue) of a transmission electron microscope (TEM) and a scanning transmission electron microscope (STEM). Images are not to scale.

In both systems the electron gun, emits a beam of electrons into an evacuated column. The beam's path is controlled by a series of magnetic lenses and apertures. In the transmission electron microscope the specimen is located between the condenser and objective lenses. Electrons that pass through the sample are dispersed by the projector lens onto a phosphor viewing screen (or camera). In a scanning transmission microscope, the beam passes through the condenser lens and aperture, where it is manipulated by a pair of scanning coils which direct the beam through the objective lens and onto the sample. The scanning coils condense the diameter of, and control the position of the beam, as it is rastered across the sample.

1.3.2 Interactions of Electrons with Matter

Electrons can interact with matter several ways, as depicted in Figure 3, and a variety of microscopy techniques have been developed which exploit the information that can be obtained from the different types of interactions.[1]

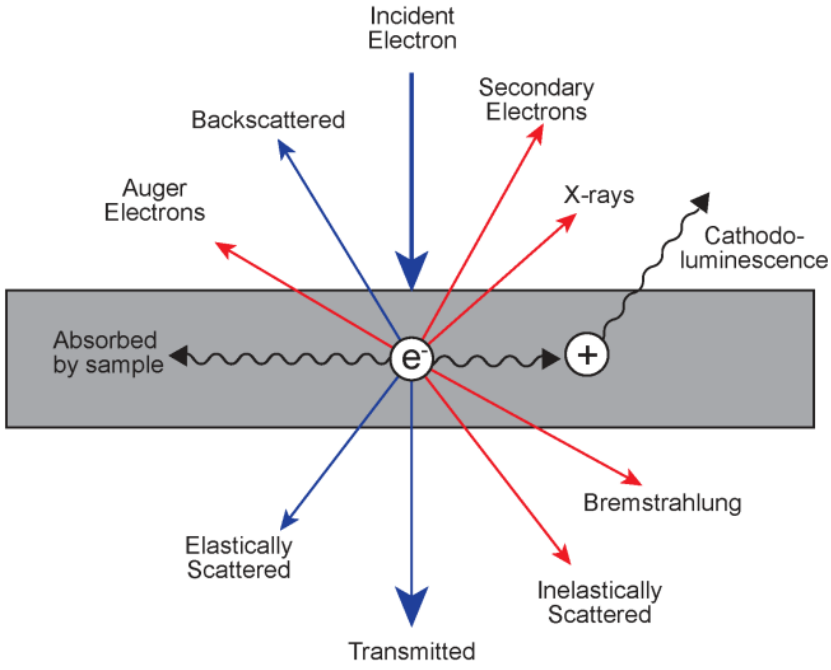

Figure 3: Electron-sample interaction. Adapted from Williams and Carey[1]

The electron may interact with and be absorbed by the sample itself, be transmitted through the sample, or it may be scattered (deflected by an angle (β)) upon interaction with the sample. Deflection of the electron can occur with or without a corresponding loss of energy. Electrons which loose energy when deflected through the sample are inelastically scattered, while those that do not undergo a loss of energy are elastically

scattered.[1] It is these later scattering events which form the primary signal in scanning transmission electron microscopy (STEM).

Elastically scattered electrons may be detected by the angle at which they are scattered. Electrons which pass through the sample (transmitted) at an angle, β, are detected by either a bright field or annular dark field (ADF, usually a ring shaped scintillation detector to which a photomultiplier is attached) detector as shown in Figure 4.

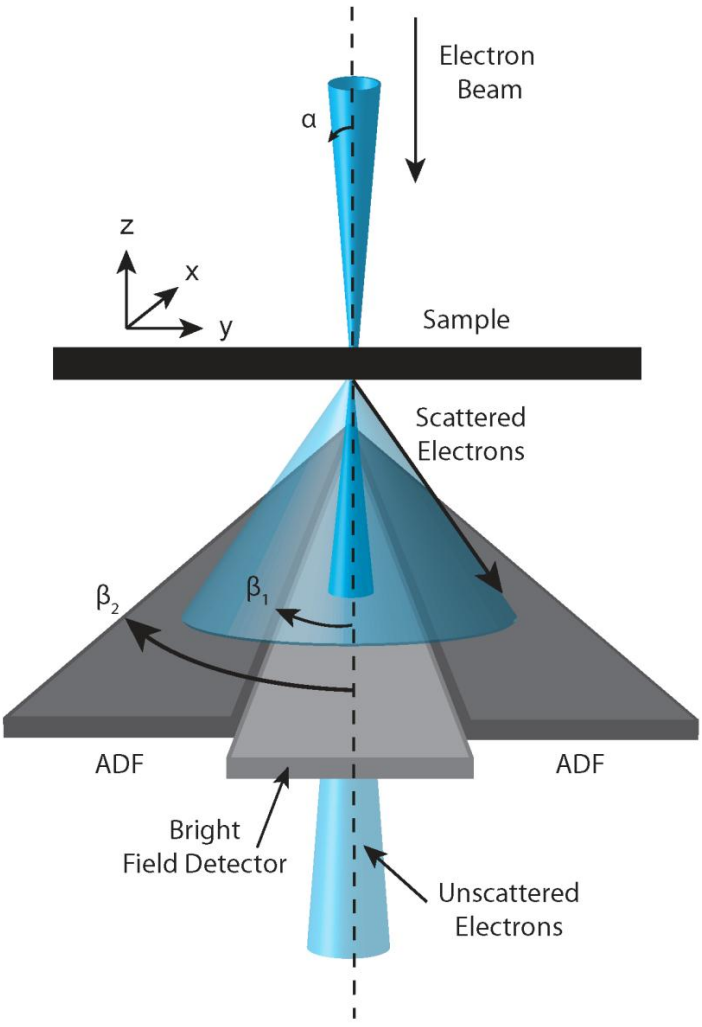

Figure 4: Schematic of electrons scattered onto bright field and annular dark field (ADF) detectors. Electrons enter the sample with a semiangle of α, where they are either scattered or transmitted

(unscattered) through the sample. If the exit angle by which the electrons are scattered is between β_1 and β_2 (inner and outer detector semiangles, respectively), they are detected by the ADF detectors. Electron that scatter at angles < β_1 are detected by the bright field detector. Image is not to scale. Adapted from Demers *et. al.*[39]

The mean free path (*l*), or average distance an electron travels between scattering events is inversely related to the atomic number (Z) of the atom off which it is scattered. Thus a higher proportion of these electrons are scattered onto the ADF detector by a high-Z material relative to a low-Z material. This dependency on Z results in contrast which varies by $\approx Z^2$ (Z-contrast). Because the electron beam in a scanning transmission electron microscope is rastered across the sample, the signal reaching the ADF detector is position sensitive, enabling individual atoms to be differentiated by the change in contrast within a composite material.[39,40] Thus, electrons which pass through the sample without interacting are not detected, improving the signal-to-noise ratio (SNR).

Other emission events that occur, in addition to scatter, include the emission of secondary electrons, auger emission, x-ray emission, bremstrahlung radiation, and cathodoluminescence. These later events are utilized in analytical EM techniques to identify signatures of specific elements

1.5 Preparation of Biological Specimens for Electron Microscopy

The resolution, and overall quality, of an EM images is highly dependent on the characteristics of the sample,[41] and is influenced by factors such as its structural preservation, thickness, and electron density.

Preservation of the native 3D structure of a biological specimen is a primary concern in sample preparation.[2,3,7,15,42,43] The aqueous environment of biological

specimens is unsuitable for EM applications due to the high vacuum of the electron microscope. Therefore, cell samples must typically be chemically fixed and dried, or frozen prior to imaging to avoid evaporation. Water is typically removed by exchanging it with ethanol, which is known to extract nonpolar components such as lipids.[3] Following dehydration the sample is either embedded in resin to retain its 3D structure and sectioned, or dried by a process called critical point drying, which prevents the sample from collapsing. Distortion of the structure during the drying or embedment processes can often occur, particularly if residual water remains trapped in the sample.[2]

Freezing the sample in vitreous ice eliminates both chemical fixation, and avoids the artifacts introduced by drying.[41,44,45] However, obtaining reliable formation of vitreous ice requires substantial practice and specialized equipment.[44]

Much like phase contrast in the light microscope, the density differences among cellular features such as organelle membranes, can be visualized in the electron microscope. Samples embedded in transparent, vitreous ice utilize this type of TEM phase contrast mechanism.[5,41,44,45] Although highly detailed images of the cellular ultrastructure are obtained using cryo-prepared samples, the low electron doses ($1\text{-}2\ e^-/Å^2$)[44] required limit the obtainable resolution.

Contrast can also be added to a sample by staining it with salts containing heavy metals salts such as osmium, uranium, and lead. These stains bind preferentially to different cellular components increasing contrast in those regions.[2,3,46]

Although both cryo-EM and heavy metal staining produce detailed images of ultrastructure, molecular tags are required to identify a specific protein, or cellular

component.[47] Because an individual protein is not discernable from the surrounding cellular material, it must be tagged to distinguish it from the background. Cellular labels employed in EM must be of sufficient size and electron density to ensure adequate an adequate SNR. Gold nanoparticles are electron dense, available in multiple sizes, and can be electrostically passivated with biological material, such as antibodies. Thus, gold-antibody complexes (immunogold) are the conventional label used in EM.[48] However, the size of the gold-antibody complex can lead to steric hindrance between closely spaced epitopes, and thus lead to artificially low label density. Additionally, antibodies and gold nanoparticles cannot pass through the cell membrane, making it is necessary to either permeabolize the membrane, or label the cell after fixation and sectioning—both of which disrupt the native environment of the cell.[2,49]

1.6 Three Dimensional Electron Microscopy

Electron microscopy images of the 3D distributions of proteins and cellular structures are typically acquired using tilt-series electron tomography.[44,45,50-55] Multiple images of the sample are recorded over a series of tilt angles, from which a 3D reconstruction is produced. However, because transmission electron microscopy (TEM) is limited to thicknesses less of $\leq$ 500 nm ($\leq$ 1μm, if energy filtering techniques are employed[50,56,57]), the sample thickness that the electron beam sees increases as the tilt angle increases, thus limiting the area that can be imaged in any one sample. Thus it is not possible to image a whole cell directly using tilt series tomography. Reconstruction of a single cell using multiple semi-thin, serially sectioned is extremely

laborious and time consuming. A complete series of cellular sections must be obtained without damage to any one individual section, and each section must be individually imaged and reconstructed via tilt series tomography then aligned to produce a 3D dataset of the entire cell.[16] Thus a considerable amount of time and labor must be invested to obtain a single sample.[55]

1.7 Imaging Tagged Proteins in Whole Cells Using STEM

Recently, STEM of thick biological specimens has been reported, utilizing both tomographic and focal series methodologies.[16,39,46,58-62] Unlike TEM, STEM can be used to image thick specimens. The ADF detector in the STEM is sensitive to Z-contrast, thus it is possible to image specific, electron dense, labels inside a thick layer of low-Z material, such as tissue or water. The low-Z material (Figure 5a) which has a long mean free path length, $l_{\text{low-Z}}$, relative to high Z-materials, has a much lower probability of high-angle elastic scattering resulting in a low ADF signal. In contrast, the high-Z material (Figure 5b) has a much smaller mean free path length, $l_{\text{high-Z}}$, thus more electrons are elastically scattered at high angles, resulting in increased signal at the detector. It is this differential in the mean free path length of the scattered electrons that enables an object composed of a high-Z material, such as gold, to be visible within a thick object composed of low-Z material, such as water.[63] Figure 5 depicts such high angle electron scattering for both low and high-Z materials. The low-Z material (Figure 5a), due to a larger value of l, scatters fewer electron at angles sufficient for them to be detected by the ADF detector. Conversely, high-Z materials (Figure 5b)

scatter electrons much more efficiently onto the ADF detector, resulting in a larger signal.

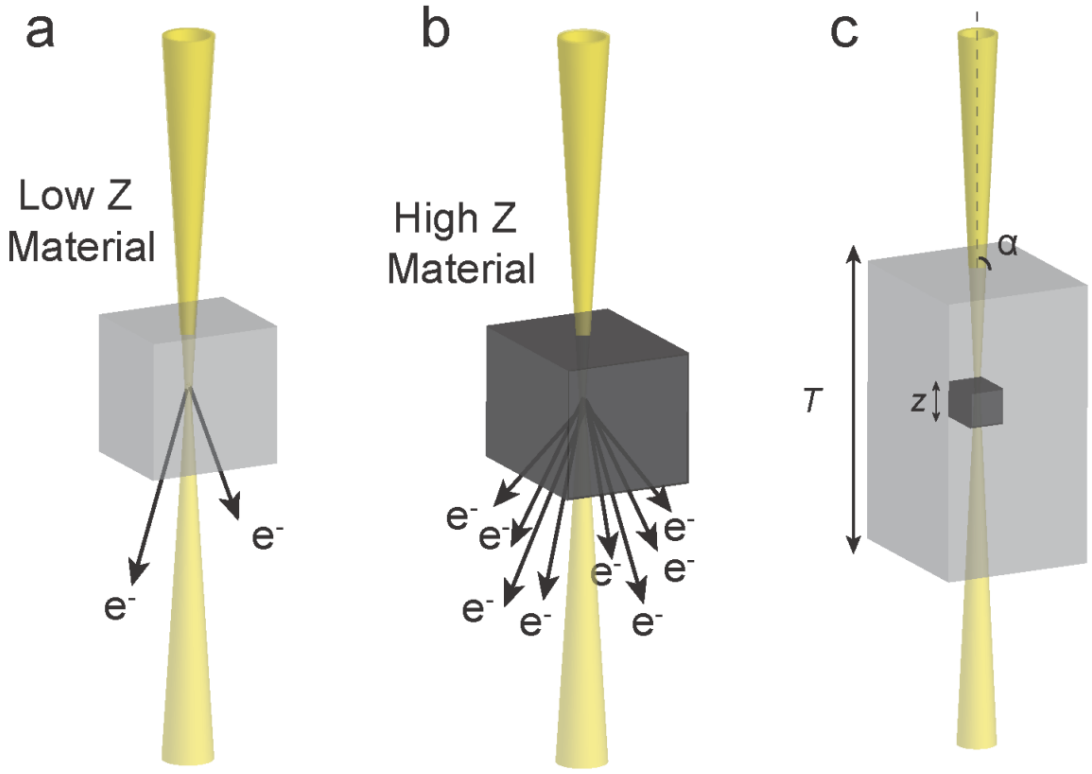

Figure 5: High angle elastic scattering leading to Z-contrast. (a) Low-Z material. (b) High-Z-material. (c) High-Z material within a thick layer of low-Z material.

For the situation shown in Figure 5c, in which a small high-Z particle is located within a thick low-Z material, the total signal collected by the ADF detector can be calculated using equation **3**.[63] Equation **3** gives the total number of electrons detected by the ADF detector, where N is the number of electrons, z is the thickness (*i.e.* size) of the high-Z object, T is the thickness of the low-Z material, and $l_{\text{Low-Z}}$ and $l_{\text{High-Z}}$ are the mean free path length of electrons scattered by low-the Z and high-Z materials, respectively.[1,64]

$$\frac{N_{\text{signal}}}{N_0} \cong 1 - e^{\left[-\left(\frac{z}{l_{\text{Low-z}}}+\frac{T-z}{l_{High-Z}}\right)\right]} \qquad (\mathbf{3})$$

It must be noted, however, that **3** is only valid for situations in which $T - z \approx T$, and both $z/l_{\text{high-Z}}$ and $T/l_{\text{low-Z}}$ are small numbers. Thus, when z is a nanoparticle (typically 10 nm or less) and T is 5-10 µm (such as a layer or liquid or cellular material) the approximation holds. The minimum detectable size of a nanoparticle (z) within a thick material is given in (**4**):

$$z = 5l_{\text{high}}\sqrt{\frac{2T}{N_0 l_{\text{low-Z}}}} \qquad (\mathbf{4})$$

Thus, a 1.9 nm diameter gold nanoparticle, whose elastic scattering mean free path length (l_{gold}) is 73 nm, will be visible in a 10 µm layer of water (l_{water} = 10.5 µm) with a signal to noise ratio of 5.

1.8 Correlative Light and Electron Microscopy

Advances in both instrumentation and labeling techniques have led to the development of correlative imaging strategies which utilize either multiple or multi-modal molecular probes.[57,65 66-71] Electron microscopy images can be correlated with LM images to localize tagged proteins at a resolution of a few nanometers.[72] Correlative imaging, unlike super-resolution fluorescence imaging, is not constrained to a small subset of available labels.[35,37,73] Rather, the sample is imaged by LM, then the same coordinates are imaged again with EM; each technique providing complementary

information.[74-76] Because conventional fluorophores are not visible in the electron microscope, many correlative techniques tag the feature of interest with two separate labels. In addition to the fluorophore, an electron-dense label, such as an antibody conjugated gold nanoparticle[50] is introduced. However using two separate probes introduces several sources of error. The binding affinities of the two tags may be different, resulting in non-uniform labeling of the two tags.[50] Additionally, common secondary antibodies, such as IgG, which link the gold nanoparticle to the primary antibody are large (12 nm for IgG) , thus the location of the gold tag may not be consistent with the protein's actual cellular location.[77] As an alternative to multiple labels, several modified, transgenically expressed fluorescent proteins have been developed to visualize these proteins using EM without introducing a second label. These include tags which photooxidze to electron dense polymers or bind fluorescently tagged biaresnical labels.[75,78] However, these methods require secondary treatment of of the sample, *i.e*. photooxidation, or addition of biarsenical fluorescein, after fluorescence imaging to render them visible for electron microscopy.

A single, bi-modal probe, which contains both fluorescent and electron dense components, may be employed as well. Correlative probes, such as dye-conjugated gold nanoparticles[79] and quantum dots (QDs)[65] are visible with both LM and EM and thus avoid the discrepancies introduced by multiple probes.[50]

1.9 Overview

The objective of this dissertation is to develop electron microscopy methods to image nanoparticle-tagged proteins in whole cells. Chapter II introduces optical

properties of lanthanide chelates and their potential as a cell permeable probe for electron microscopy applications. Chapter III describes a novel correlative approach capable of imaging whole eukaryotic cells in a layer of liquid with fluorescence microscopy and with STEM. Thus, the native state of the proteins was preserved.

Chapter IV describes a methodology to stabilize whole eukaryotic cells for 3D-focal series imaging using STEM. A quantitative method was developed to analyze the stability of the ultrastructure after electron beam irradiation using TEM. Focal series of gold nanoparticles in whole cells were obtained of both thin and thick cellular regions using an aberration-corrected STEM, and a 3-D dataset was generated without tilting the specimen. The data was deconvolved allowing the positions of the nanoparticles to be localized with a precision of 2.5 nm

CHAPTER II

SYNTHESIS AND CHARACTERIZATION OF LANTHANIDE CHELATE BIMODAL MOLECULAR PROBES

SECTION I:

COUMARIN AND ACRIDINE FUNCTIONALIZED MACROCYCLIC LANTHANIDE (III) CHELATES WITH THE POTENTIAL FOR TWO PHOTON EXCITATION

2-1.1 Introduction

The optical properties of lanthanide ions are well suited for molecular imaging applications. They have a large Stokes shift,[80] their emission spectrum is sharp and narrow, and they exhibit a wide range of lifetimes, from μsec for neodymium and ytterbium up to milliseconds for europium and terbium.[81] Lanthanide (III) ions have inherently low extinction coefficients (< 10 $M^{-1}cm^{-1}$),[82,83] therefore, chromophores with a high extinction coefficient are typically used as sensitizing agents or antennae.[81] While the exact mechanism of energy transfer (through bond or through space) is still under debate,[84,85] typically during sensitization, the absorbed energy induces population of the triplet state of the antenna molecule, followed by a transfer of energy to the lanthanide (III) ion. The excited electrons then decay via a radiative process leading to emission of a photon.[86] Typical antennae, such as quinoline, phenthrideine, coumarin, and others, increase the molar extinction coefficient of the lanthanide ion to a value of 1000-4000 $M^{-1}cm^{-1}$, an increase of three orders of magnitude over the ion alone.[80]

Lanthanide chelates have attractive properties for biological and clinical applications. The ion-chelate complex is stable at physiological pH, non-toxic, and has good aqueous solubility.[87] Ligands such as diethylenetriaminepentaacetic acid (Magnevist™) and 1,4,7,10-tetraazacyclododecane-1,4,7,10-tetraacetic acid (Dotarem TM), coordinated to the lanthanide ion, gadolinium, are routinely employed in the clinic as MRI contrast agents. [88] In addition to their clinical safety and high aqueous solubility, the optical properties of lanthanide chelates are also desirable. Antenna sensitized, luminescent lanthanide chelates are resistant to photobleaching and have long luminescent lifetimes.[82] The long luminescent lifetimes of lanthanide ions have been utilized in many assays[89,90] by allowing the signal to be temporally separated from the background.[83]

Our group and others [91-93] have demonstrated that biologically targeted lanthanide imaging agents can be used to monitor and potentially diagnose diseases. While these compounds have shown initial promise, they require ultraviolet (UV) excitation (λex). In addition to tissue damage and increased tissue autofluorescence, UV light has low (< 1mm) tissue penetrability.[94] In contrast, near infrared (NIR) wavelengths between 650 and 900 nm are poorly absorbed by water, hemoglobin, and other tissue components, and thus are able penetrate more deeply.[95] The relative transparency of tissue to NIR wavelengths results in less tissue autofluorescence and a lower background signal.[83] Because the lanthanide chelates are antenna sensitized, the excitation wavelength can be tuned by changing the antenna. Utilizing an antenna with a large two-photon absorbance cross-section permits excitation using NIR wavelengths via a two photon absorbance process ($2\lambda_{ex}$).

Here we present the results of using coumarin and acridine chromophores as sensitizers for lanthanide (III) ions, and their potential for two-photon using NIR excitation. The lanthanide-chelate, 1,4,7,10-tetraazacyclododecane-1,4,7-triyl) triacetate, was modified using several coumarin compounds for the sensitization of europium. An analogous chelate was also prepared containing an acridine molecule for sensitization of lower energy lanthanide ions such as ytterbium and neodymium. Because the absorbance of acridine is red shifted relative to the coumarin, it is expected to be a more robust candidate for two photon excitation in the NIR. The length and presumed flexibility of the antenna moiety may allow it to coordinate with the lanthanide ion more effectively, and thus improve energy transfer between the antenna and the lanthanide ion as shown by the spectral data.

2-1.2 Results and Discussion

Three coumarin and one acridine antenna (Figure 6) were coupled to 1, 4, 7, 10-tetraazacyclododecane-1, 4, 7- triacetate (DO3A), a well known chelator of lanthanide (III) ions

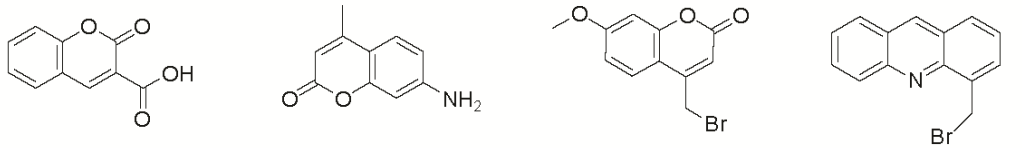

Figure 6: Antennae Used to Sensitize Lanthanide (III) Ions

The three coumarin antennas that were studied have excited energy states that are sufficient to sensitize lanthanide ions which emit in either the visible (europium) or near infrared (NIR) (ytterbium and neodymium) spectral region.

2-1.2.1 Synthesis

Coumarin-3-carboxylic acid, 7-amino-4-methyl coumarin, and 4-(bromomethyl)-7-methoxy coumarin, were coupled to a t-butyl protected ligand, tri-tert-butyl 2,2',2''-(1,4,7,10-tetraazacyclododecane-1,4,7-triyl)triacetate (tbuDO3A) [96], using the procedures shown in Scheme 1.

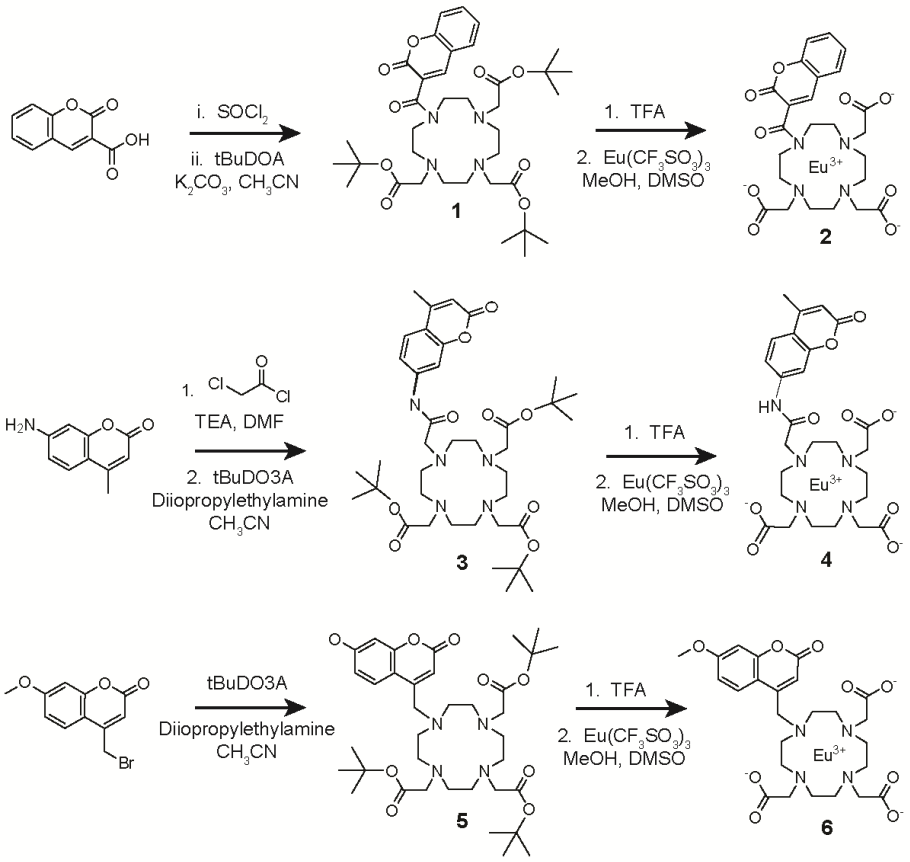

Scheme 1: Synthesis of coumarin sensitized lanthanide chelates

Europium (III),2',2''-(10-(coumarin-3-carbonyl)-1,4,7,10-tetraazacyclododecane-1,4,7-triyl) triacetate (2)

Coumarin-3-carboxylic acid was converted in situ to an acyl chloride with thionyl chloride, and immediately coupled to tBuDO3A, to give 1. The t-butyl protecting groups were removed by hydrolysis with neat trifluoroacetic acid (TFA), after which the TFA was removed via rotary evaporation, and the product was dried under high vacuum. The complete removal of the t-butyl protecting groups was verified by with 1H NMR and the ligand was coordinated with europium (III) by dissolving the ligand in methanol containing a few drops of dimethyl sulfoxide (DMSO). The ligand was stirred with europium triflate ($Eu(CF_3SO_3)_3$) overnight to chelate. The product, europium (III) 2,2',2''-(10-(coumarin-3-carbonyl)-1,4,7,10-tetraazacyclododecane-1,4,7-triyl) triacetate (2) was dissolved in a minimal amount of methanol and triturated with diethyl ether. The precipitate was collected and re-dissolved in DMSO. The product was lyotholized to give a fluffy white powder.

Europium(III) 2, 2', 2'' - (10- (2- ((4-methyl-coumarin)amino)-2-oxoethyl)-1 , 4, 7, 10-tetraazacyclododecane-1, 4, 7 -triyl)triacetate (4)

The second coumarin antenna, 7-amino-4-methyl coumarin, was acylated with chloroacetyl chloride to give a conjugable analogue 7-(2-chloro-N-methyl acetamide)-4-methyl coumarin. This ligand was coupled to t-BuDO3A to give 3. The t-butyl protecting groups were removed via hydrolysis with TFA, and the ligand was chelated with europium, using its triflate salt to yield 4.

Europium(III) 2, 2', 2'' - (10- ((7-methoxy-Coumarin-4-yl)methyl)-1, 4, 7, 10-tetraazacyclododecane-1,4,7-triyl)triacetate (6)

The final coumarin antenna, 7-methoxy-(4-bromomethyl)-coumarin was attached directly to the tBu-DO3A ligand to give 5. Excess starting material was removed using

flash chromatography, and the t-butyl protecting groups were subsequently removed by hydrolysis with TFA. The remaining TFA and volatile hydrolysis products were removed by flowing nitrogen through the sealed reaction vessel until only product remained. Removal of t-butyl groups was verified with NMR and the product was then immediately dissolved in methanol and stirred at room temperature with europium triflate to give 6. The metal-chelator complex was triturated and lyotholized as described above.

2, 2', 2'' - (10-(4-methyl acridine)-1, 4, 7, 10 - tetraazacyclododecane-1, 4, 7-triyl) triacetate (9)

The fourth antenna, 4-(bromomethyl) acridine, 7, was prepared from the acridine precursor and coupled to the DO3A chelator as shown in Scheme 2.

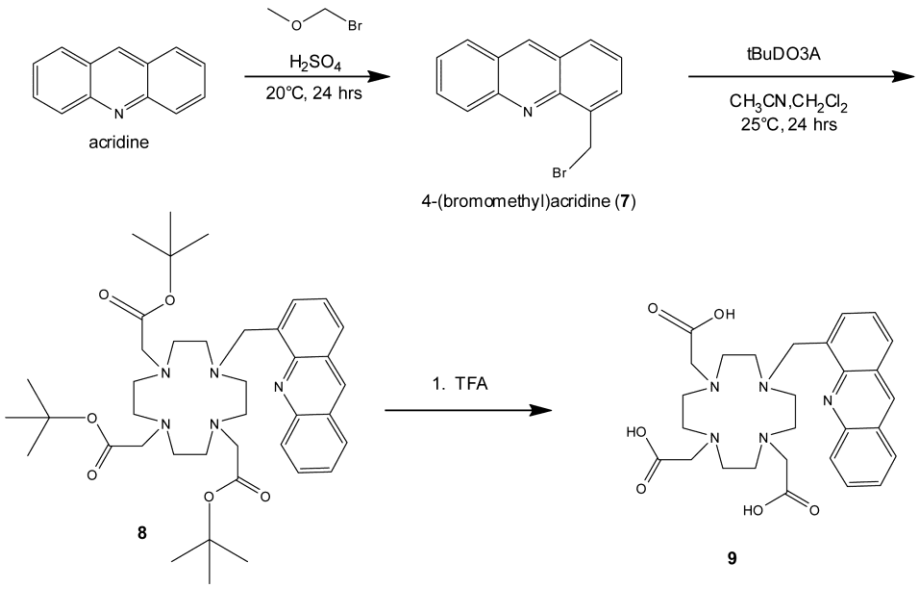

Scheme 2: Synthesis of 4-methylacridine-DO3A

Regioselective bromomethylation of the 4-position of acridine was accomplished using the synthesis described by Chiron and Galy. [97] Acridine was acidified to increase the reactivity of the nitrogen atom using sulfuric acid, then reacted with 1.5 equivalents

of bromo(methoxy)methane. The product, 4-(bromomethyl) acridine was coupled to tBuDO3A to yield 8, and the t-butyl protecting groups were removed via acid hydrolysis with TFA to give 9.

2-1.2.2 Optical Characterization

Fluorescence, photoluminescence excitation (PLE) spectra, and quantum yield (QY) measurements were obtained using ISS PC1 photon counting fluorimeter equipped with a xenon arc lamp.

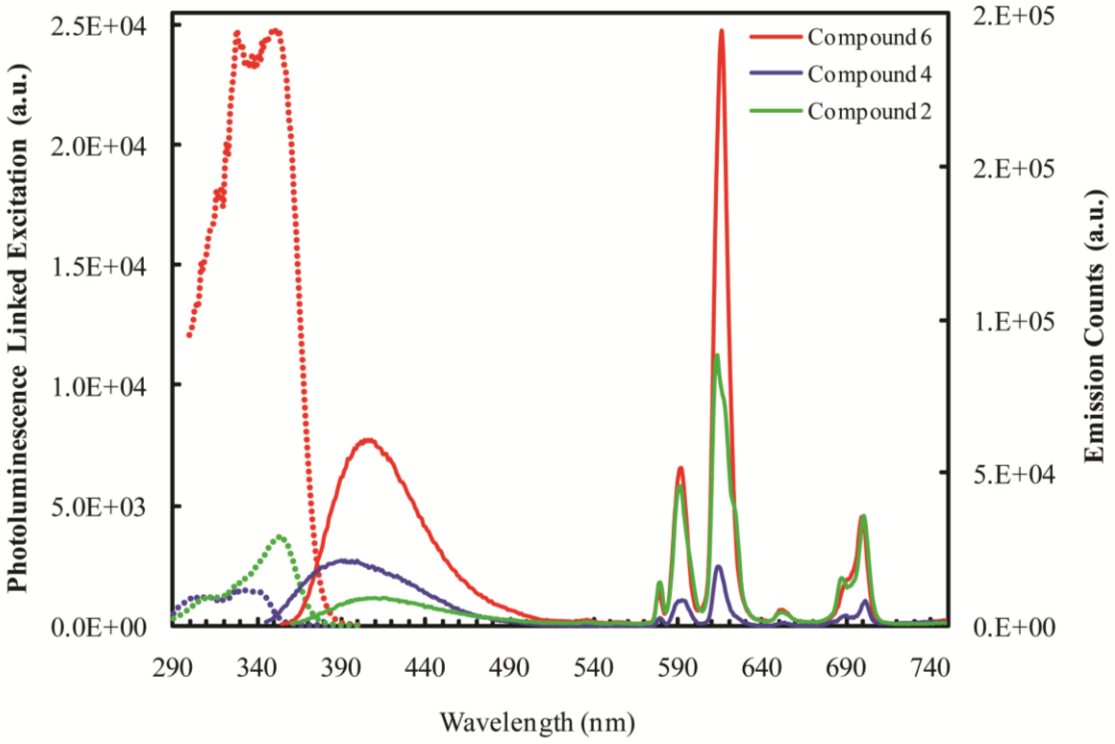

Figure 7: Spectra showing the photoluminescence linked excitation (dashed lines) and emission (solid line) of coumarin sensitized europium (III) chelates (250 µM) in methanol.

The dashed lines in Figure 7 show the PLE spectra for the coumarin sensitized compounds (2, 4, and 6) for to the 615 nm emission line. For fluorescence

measurements (solid line) each compound was excited at the wavelength which produced the strongest emission at the 615 nm. Four additional emission peaks are also observed at 577 nm, 590 nm, 643 nm, 700 nm. For each compound, a broad emission peak is also observed within the 380-440 nm range of the spectra. This peak corresponds to the emission wavelength of the respective coumarin antenna, and is a result of energy that is not transferred to the lanthanide ion. The smaller the ratio of the antennas' fluorescence peak is to the lanthanide fluorescence peak, the more energy is transferred to the lanthanide ion, indicating a more efficient transfer of energy from the sensitizer.

Extinction coefficients (ε) were measured with a PharmaSpec UV-1700 Spectrophotometer and calculated from Beer's Law. Ligand 6, prepared with the antenna 4-(bromomethyl)-7-methoxy coumarin, exhibited the best optical properties as a sensitizer. Its molar extinction coefficient, 8400 $M^{-1}cm^{-1}$, was the largest of the three coumarin antennas studied, and resulted in the strongest 615 nm line emission of the europium ion. Additionally this chromophore is both inexpensive, soluble, and requires no further functionalization prior to conjugation to the chelate. Ligand 2, exhibited very good energy transfer from its coumarin antenna to the europium ion (as evidenced by the low antenna emission), its extinction coefficient was 4172 $M^{-1}cm^{-1}$. Ligand 4 exhibited in the poorest antenna-to-lanthanide energy transfer, since the emission from the antenna (404 nm) is greater than the strongest emission of europium (615 nm). This is not unexpected due to the distance of the antenna from the DO3A cage (four bond lengths compared to two bond lengths). The optical properties of the three coumarin sensitized europium chelates are summarized in Table 2.

Table 2: Optical Properties of Coumarin Sensitized Europium Chelates

Chelate	λ_{Ex} (nm) [a]	ε ($M^{-1}cm^{-1}$)	QY (%)
2	347	4172	0.085
4	357	1533	0.065
6	345 [b]	8438	0.140

[a]photoluminescence excitation,
[b]strong absorbance past 360 nm

For in vivo optical imaging and other biological applications the fluorescent imaging agents must be detectable against the background. Additionally, the necessary excitation and emission signal must be able to penetrate the tissues.[95] Fluorophores which excite and emit at wavelengths within NIR region of the spectrum (650-1000 nm) are the most desirable in vivo applications due to tissue transparency at NIR wavelengths.[82,98] Thus, two photon upconversion of the lanthanide ion using wavelengths larger than 700 nm will increase tissue penetration, and decreases both auto-fluorescence of endogenous species in the cell and damage by UV excitation wavelengths.[99]

Two photon excitation occurs when a species enters an excited energy state by simultaneously absorbing two photons whose wavelength is $2\lambda_{ex}$. Thus, a species which is normally excited using either UV or visible photons, can be excited with NIR light instead. Highly conjugated species, such as coumarin and acridine, exhibit a large two photon cross-section, making them efficient targets for two-photon applications.[100] Two photon excitation has several advantages in biological applications.[99] The longer wavelengths used in two photon excitation impart less damage to cells and tissues, and greater tissue penetration is achieved when using NIR light. Using an antenna that can be

excited by two photon absorption will allow upconversion of europium (III) using wavelengths longer than 700 nm, thus reducing both auto-fluorescence of endogenous species in the cell, and tissue damage caused by UV excitation.

The antenna, 4-(bromomethyl)-7-methoxy coumarin, was the best candidate for two photon excitation since it exhibited the most red-shifted absorbance. Two photon excitation of 2, 2', 2'' - (10-((7-methoxy-2-coumarin-4-yl) methyl)-1, 4, 7, 10-tetraazacyclododecane-1,4,7-triyl) triacetate was performed using a Zeiss LSM510 laser scanning confocal microscope equipped with a Chameleon mode-locked titanium sapphire laser (Coherent).

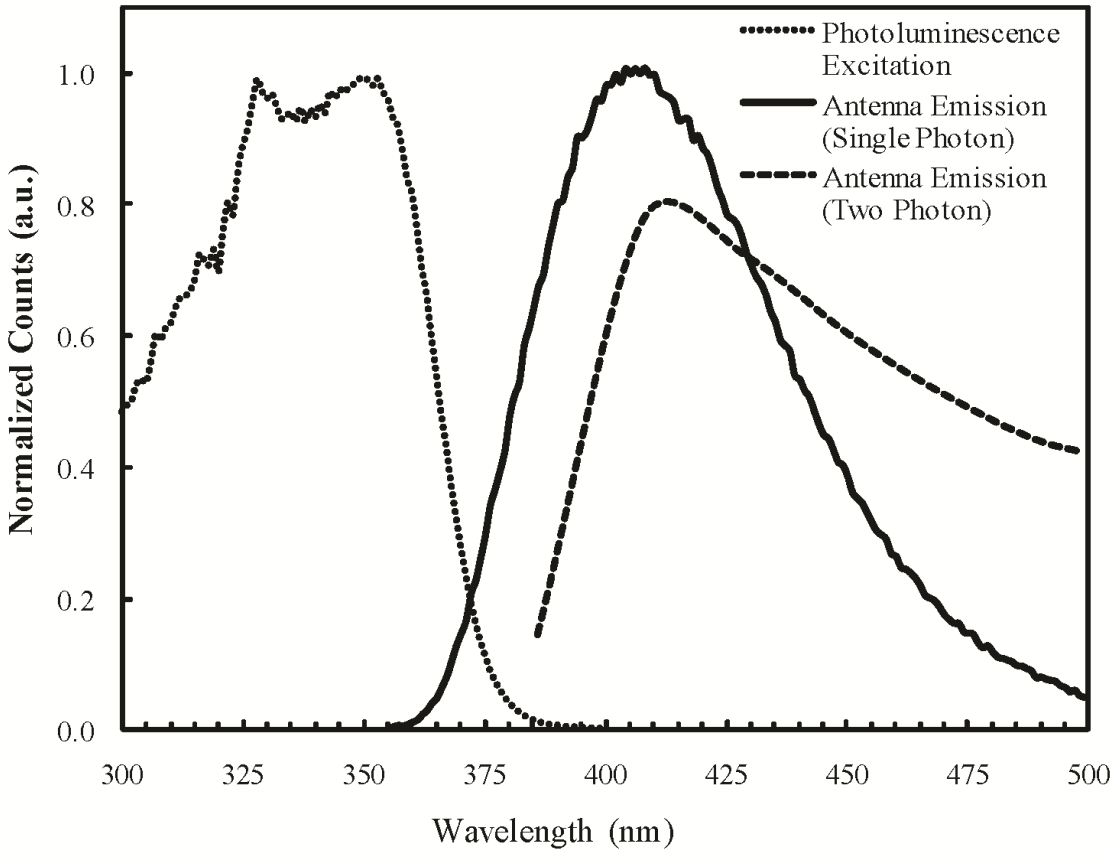

Figure 8: One and two photon excitation of Eu(III)-methoxy-coumarin-DO3A

Although λ_{max} of the ligand was 346 nm, it exhibited enough absorption at 360 nm, as shown in by the dotted photoluminescence excitation spectra in Figure 8, for two photon excitation at 720 nm. The 404 nm emission of the ligand after single photon excitation (shown by the solid line) correlates with emission after two photon excitation at λ= 720 nm (dashed line).

A $3.7x10^{-2}$ M solution of the 4-methyl acridine ligand (9) was made in ethanol, and the absorption (blue) and emission (λ_{ex} = 358 nm) of the ligand was measured. The 4-methyl acridine antenna has a broad emission profile that extends from 300 nm up to 400 nm. The emission profile for compound 9, using λ_{ex} = 358 nm, results in a broad emission band with two distinct emission peaks at 450 and 472 nm. The fluorescence from the lanthanide was not obtained due to insensitivity of the detector for wavelengths longer than 800 nm.

Figure 9 shows the emission of the acridine sensitized ligand, 9, after both single (green), and two photon excitation (dashed lines). The ligand was excited at 750 nm and the emission spectrum was recorded (orange). It was found that excitation with 750 nm light produced a maximum emission centered at 472 nm, the second peak observed after single photon excitation of 9. Two photon excitation, using a longer λ_{ex} of 800 nm, yielded the same emission spectrum as λ_{ex} with 750 nm, but at much lower intensity (red).

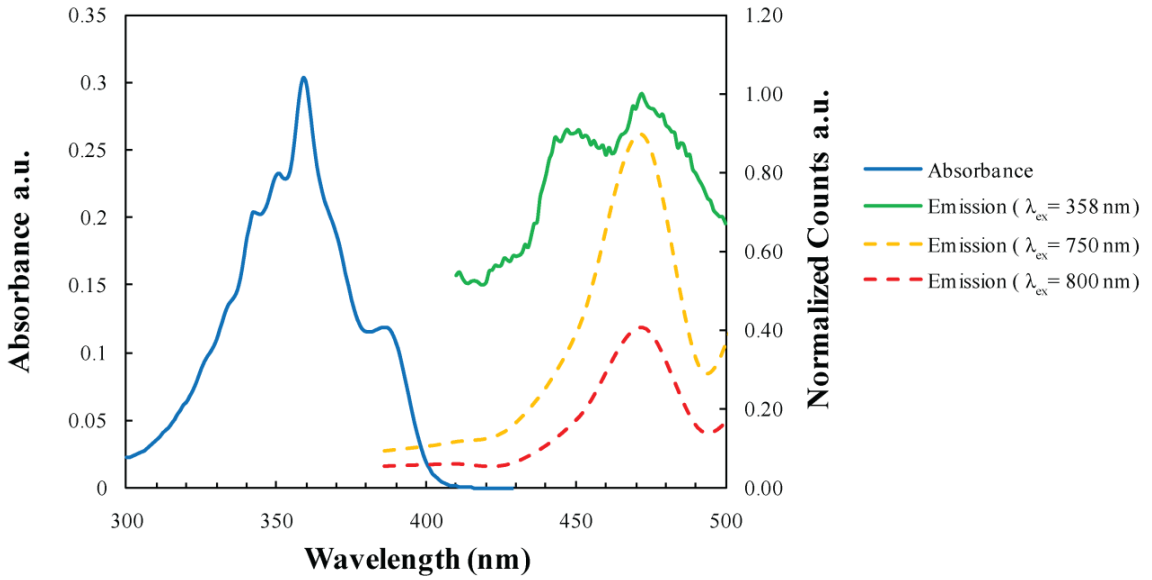

Figure 9: Single and two photon excitation of 4-methyl-acridine-DO3A. The absorbance spectrum is shown in blue and emission after single photon excitation is shown in green. Emission after two photon excitation with an excitation wavelength of 750 nm is shown by the dashed orange line. Acridine fluorescence is still observable after excitation with 800 nm light (dashed red line) although at a lower intensity than was observed with an excitation wavelength of 750 nm.

2-1.3 Conclusions:

The molar extinction coefficient of europium (III) 2,2',2"-(10-(coumarin-3-carbonyl)-1,4,7,10-tetraazacyclododecane-1,4,7-triyl) triacetate (6) at 8400 $M^{-1}cm^{-1}$, increased by 240% relative to our previously published quinoline methyl antenna [101]. The antenna, 7 – methoxy - (4-bromomethyl) - coumarin, is inexpensive, soluble, and requires no further functionalization prior to conjugation to the tetraazacyclododecane backbone. Although 7 – methoxy - (4-bromomethyl) - coumarin showed potential as a two-photon active antenna for the sensitization of europium, its two photon absorbance (720 nm) is at the edge of the capability of the excitation laser.

Utilizing 4-bromomethyl acridine, which is red-shifted relative to 7-methoxy-(4-bromemotheyl) - coumarin, as the sensitizing antenna permitted upconversion with a λ_{ex}

of 750 nm. The ligand, 2, 2', 2" - (10 - (acridin-4-ylmethyl) - 1, 4, 7, 10-tetraazacyclododecane-1, 4, 7 - triyl) triacetate (9) was excited using two photons and resulted in an emission of 472 nm. We expect that this ligand (10) complexed with a NIR emitting lanthanide ion such as ytterbium or neodymium will yield a lanthanide chelate which is both exited and emissive in the NIR, allowing better penetration and signal for in vivo applications.

2-1.4 Experimental Details

Tri-tert-butyl (2, 2', 2"- (10-(coumarin-3-cabonyl) - 1, 4, 7, 10- tetraazacyclododecane diacetate) (1)

Coumarin-3-carboxylic acid, (0.4003 g, 2.1 mmol) was combined with anhydrous thionyl chloride (3 mL, 15 mmol). Dichloromethane was added until the remaining solid dissolved (20 mL). The reaction was stirred at room temperature overnight. The solvent was removed by flowing argon through the sealed reaction then dissolved in acetonitrile (50mL) and combined with tri-t-butyl-tetraazacyclododecane bromide salt (0.8550 g, 1.44 mmol). Potassium carbonate (0.63 grams) was added to the reaction flask. A catalytic amount of potassium iodide was added to the final reaction mixture. The reaction was stirred overnight, filtered, and the solvent was removed via rotary evaporation. The product was purified on silica gel using a Biotoge Flash Chromatography system (eluent: methanol/chloroform gradient beginning at 1% methanol and increasing to 8% methanol over 1,020 mL on a 40+M column). Solvent was removed via rotary evaporation and product, tert-butyl-(coumarin-3-carbonyl)-DO3A (1), was dried under vacuum to give a clear yellow oil. (0.4636 grams, 47% yield)

^{1}H NMR (300 MHz, CDCl3) δ = 1.3 (s, 9H), 1.40 (s, 18H), 2.68(t, 8H), 2.89 (d, 4H), 3.11 (s, 2H), 3.29 (d, 4H), 3.72 (m, 4H), 7.26 (m, 2H), 7.42(m, 2H), 7.78 (s, 2H) ppm.

2,2',2''-(10-(coumarin-3-carbonyl)-1,4,7,10-tetraazacyclododecane-1,4,7-triyl) triacetate

The t-butyl protecting groups of 1 were removed by dissolving tert-butyl-(coumarin-3-carbonyl)-DO3A in 10 mL of neat TFA. The reaction was stirred for five hours. The TFA and hydrolysis products were removed via rotary evaporation and the product was dried under high vacuum for several hours to give coumarin-3-carbonyl-DO3A in > 90% yield.

^{1}H NMR (400 MHz, DMSO) δ = 8.144 (br, 1H,), 7.765 (d, 1H), 7.680 (d, 1H), 7.447 (m, 2H), 3.961-2.985 (22H) ppm.

Europium (III) 2,2',2''-(10-(coumarin-3-carbonyl)-1,4,7,10-tetraazacyclododecane-1,4,7-triyl) triacetate (2)

Coumarin-3-carbonyl-DO3A (0.1534 g, 0.29 mmols) was dissolved in 1.5 mL of methanol and 0.5 mL (0.0497 g, 0.09 mmol). Europium triflate (1.1 eq., 0.0634 grams) and a few drops of DMSO were added to aid solubility. The reaction was stirred overnight at room temperature. Solvent was removed via rotary evaporation and redissolved in a minimal volume of methanol. Diethyl ether was added dropwise to precipitate Eu- coumarin-3-carbonyl-DO3A (2). Solid was isolated by centrifugation to yield 0.0398 grams, 61.8% yield.

2-(4-methyl-coumarin-7-yl) chloroacetamide

To a flame dried 50 mL round bottom flask, 7-amino-4-methyl coumarin (0.1013g, 0.57mmol) and dissolved 5 mL of DMF with triethylamine (0.17 mL, 2 eq). Chloroacetyl chloride was added (0.060 mL, 1.3 eq) and the reaction was stirred for thirty minutes. Solvent was removed by rotary evaporation and recrystallized from acetonitrile and water.

^{1}H NMR (DMSO) δ = 2.402 (3H), 4.324 (2H), 6.292 (1H), 7.506 (1H), 7.761 (2H), 10.731 (1H) ppm.

Tert-butyl-2, 2' 2" - (10- (2- (4-methylcoumarin-7-amino) oxoethyl) - 1, 4, 7, 10-tetraazacyclododecane diacetate (3):

Next, the 2-(4-methyl-coumarin-7-yl) chloroacetamide (0.0469 g, 0.186 mmol) was added to a 50 mL round bottom flask. It was dissolved in 5 mL of DMF and tBuDO3A bromide salt (0.0997, 0.9 eq) was added. Diisopropyl ethyl amine was added (0.055 mL), and the reaction was stirred overnight and the solvent was removed by rotary evaporation. (60 % yield). Conjugation of the antenna to tBuDO3A was verified with LCQ-MS. (M^++Na) = 752.2

Europium (III) - 2, 2', 2" - (10- (2- (4-methylcoumarin-7-amino) oxoethyl)-1, 4, 7, 10-tetraazacyclododecane (4)

Tert-butyl - 2, 2 '2"- (10- (2- (4-methylcoumarin -7-amino) oxoethyl) - 1, 4, 7, 10-tetraazacyclododecane diacetate (0.0469 g) was dissolved in ~10 mL of TFA and stirred at room temperature for 1-2 hours. The TFA was evaporated, and the remaining product was dissolved in 3 mL of methanol. DMSO (1 mL) was added to further solubilize. Europium triflate (0.0394 g, 1 mmol) and triethylamine (0.050 mL) were

added and the reaction was stirred overnight. Solvent was removed by rotary evaporation and the product was precipitated from methanol using diethyl ether to yield 0.0225 grams of product. (> 90% yield).

Tri – tert - butyl 2, 2', 2'' - (10-((7-methoxy-coumarin-4-yl)methyl)-1, 4, 7, 10-tetraazacyclododecane-1,4,7-triyl)triacetate (5):

In a 50 mL round bottom flask 4-(bromomethyl)-7-methoxy coumarin (0.5062 g) was dissolved in 35 mL of DMF. Tri-t-butyl-tetraazacyclododecane bromide salt (0.9868 g, 0.9 eq) was added to the flask. Diisopropyl ethyl amine (0.274 mL), and molecular sieves were added to the flask. The reaction was capped under argon and stirred at 60°C overnight. Solvent was removed by rotary evaporation and the product was purified on silica using a Biotage SPI (R_f = 0.22, chloroform: methanol 85:15 to give 0.8135g (60%) of 5. (M^++H) = 704.4

^{1}H NMR ($CHCl_3$) δ: 1.446 (27H), 2.279 (Broad, 9H), 3.027 (Broad, 15H), 3.871 (3H), 6.351 (1H), 6.821 (1H), 6.911 (1H), 7.767 (1H) ppm.

2, 2', 2'' - (10-((7-methoxy-2-coumarin-4-yl) methyl)-1, 4, 7, 10-tetraazacyclododecane-1,4,7-triyl)triacetate

Compound 5 (0.6998 g, 0.995 mmol) was dissolved in 4 mL of TFA and stirred twenty-four hours in a 10 mL round bottom flask to remove the t-butyl protecting groups. The reaction was dried via rotary evaporation to yield 0.5322 grams of 5 (99% yield). Removal of the t-butyl groups was verified by mass spectrometry and NMR. (M^++H) = 535.5.

^{1}H NMR (DMSO) δ: 2.954 (s, 4H), 3.154 (t, broad,12H), 3.426 (s, 2H), 3.537 (s, broad, 2H), 3.738 (s, 4H), 3.867 (s, 3H), 7.415 (m, 2H), 7.661 (t, 1H), 7.762 (d, 1H) ppm.

Europium (III) 2, 2', 2'' - (10-((7-methoxy-2-coumarin-4-yl) methyl)-1, 4, 7, 10-tetraazacyclododecane-1,4,7-triyl)triacetate (6)

The deprotected ligand (0.0560 g, .105 mmol) was dissolved in 10 mL of methanol and transferred to a 50 mL round bottom flask. Europium triflate (0.0714 g) was added and the reaction was stirred for three days. The solvent was removed by rotary evaporation and the product was precipitated from methanol using diethyl ether to yield 0.0619 grams of product (86%).

4-(Bromomethyl)-Acridine (7)

To a 50 mL round bottom flask was added 1.0072 g (5.62×10^{-3} mol) of acridine. To that was added 20 mL of concentrated sulfuric acid and the reaction vessel purged with dry nitrogen gas. To the stirring orange/red solution was added 0.685 mL (8.39×10^{-3} mol) of bromomethyl methyl ether. The reaction vessel covered with aluminum foil and allowed to stir for 24 hours at room temperature (25°C). The solution was poured into a beaker containing 400 mL of ice, stirred for 30 minutes after which another 100 mL of ice was added. The solution was stirred for an additional 2 hours, washed with chloroform, the aqueous phase collected and the solvent removed. The crude product was purified over silica gel eluted with 7:3 chloroform/hexane to yield 0.2291 g (8.42x10-4 mol) of 4-bromomethylacridine (15% yield).

^{1}H NMR (CDCl3) δ = 5.429 (s, 2H), 7.558 (m, 2H), 7.806 (t, 1H), 7.937 (db, 1H), 7.989 (t, 2H), 8.322 (d, 1H), 8.765 (s, 1H) ppm

2,2',2''-(10-(acridin-4-ylmethyl)-1,4,7,10-tetraazacyclododecane-1,4,7-triyl)triacetate (8)

To a flame dried 50 mL round bottomed flask was added 10 mL of anhydrous acetonitrile. To that was added 0.0501 g ($1.84x10^{-4}$ mol) of 4-bromomethyl acridine followed by 0.1086 g ($1.82x10^{-4}$ mol) of tBu-DO3A. The solution was stirred for 5 minutes followed by the addition of 121.45 µL ($7.35x10^{-4}$ mol) of diisopropylethylamine. One milliliter of anhydrous dichloromethane was added to the solution which was then stirred at room temperature (25°C) for 24 hours. The solvent was removed and the crude yellow solid purified over silica gel eluted with an 8:2 toluene/methanol solution yielding 0.0975 g ($1.38x10^{-4}$ mol) of the dark brown product (75% yield). LCQ-MS = 706.5 (M^++H)

^{1}H NMR ($CDCl_3$) δ = 1.457 (s, 9H), 1.505 (s, 9H), 1.532 (s, 9H), 2.18 (b, 16H), 3.005 - 3.385 (b, m, 8H), 7.642 (t, 2H), 7.772 (t, 2H), 8.245 (d, 2H), 8.693 (d, 2H) ppm

The tert-butyl protecting groups were removed via stirring the protected product with trifluoroacetic acid for 3 hours followed by removal of the remaining solvent to yield the deprotected 2,2',2''-(10-(acridin-4-ylmethyl)-1,4,7,10-tetraazacyclododecane-1,4,7-triyl)triacetate (9) (>99% yield). LCQ-MS = 538.4 (M^++H)

SECTION II:

PRELIMINARY TRANSMISSION ELECTRON MICROSCOPY OF GADOLINIUM LOADED PAMAM DENDRIMERS

2-2.1 Introduction:

Bi-modal molecular probes, probes that are detectable by two different microscopy techniques, can increase the number of parameters and offer high resolution. Fluorescent, electron dense nanoparticles combine the advantages of light microscopy (LM), and the resolution of electron microscopy (EM). Dendrimers, hyper-branched macromolecular nanoparticles,[102] offer a number of advantages as a probe for cellular imaging applications: (1) They are readily internalized by cells,[103,104] (2) they have low toxicity,[103] and (3) they contain multiple functional groups onto which a variety of species can be attached.[102,105] Because the surface of the dendrimer is composed of multiple reactive functional groups, a variety of small ligands and imaging agents can be covalently coupled to the dendrimer scaffold for transport into the cell.[106]

2-2.1.1 PAMAM Dendrimer Molecular Probes

Polyamido-amine (PAMAM) dendrimers are synthesized by iterative additions of methyl acrylate and ethylene diamine, to a central ethylene diamine core, as shown in Scheme 3. Successive iterations are denoted generation-0 (G(0)), generation-1 (G(1)) and so forth for each additional iteration.[103]

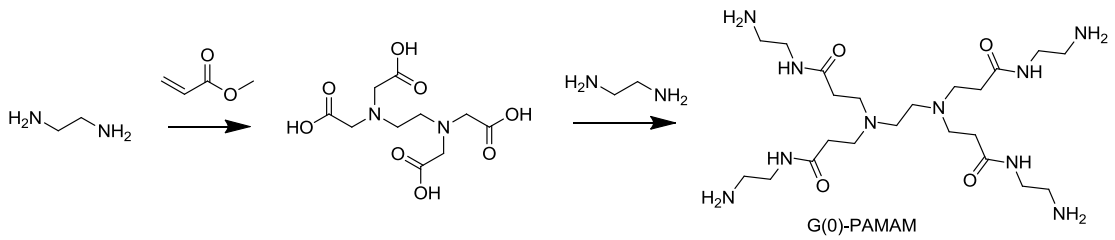

Scheme 3: Synthesis of PAMAM dendrimer

Using standard peptide coupling methodologies, small-molecule ligands, fluorophores, and metal chelators can be covalently anchored to the surface of the dendrimer. A generalized scheme of the synthetic strategy for functionalizing amino-terminated PAMAM dendrimer is shown in Figure 10.

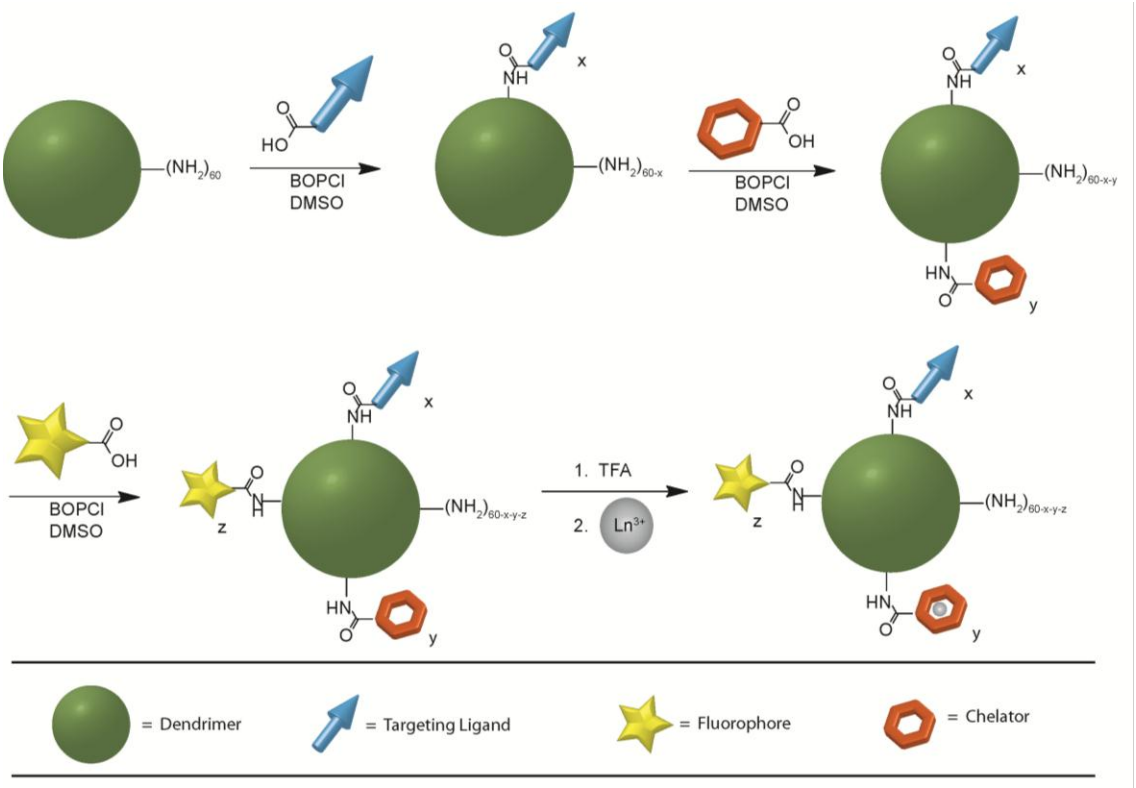

Figure 10: Synthetic Strategy for Dendrimer Functionalization

2-2.1.2 Molecular Targeting of the TSPO Receptor

The 18 kDa translocator protein, TSPO, formerly referred to in literature as the peripheral benzodiazepine receptor, is an isoquinoline binding protein located on the outer mitochondrial membrane.[107] TSPO is responsible for binding and transporting cholesterol into the mitochondria for steroid biosynthesis. TSPO is also capable of binding and transporting other high affinity small molecules such as Ro-5864, PK11195, DAA1106, and DAA1097.[108,109] TSPO is involved in a variety of processes, including steroidogenesis, cell proliferation, mitochondrial respiratory control, chemotaxis, and apoptosis.[70,108,110] In addition to the many roles that TSPO plays in healthy cells, it has been shown to be upregulated in certain cancer cell lines, including colon, breast, and ovarian carcinomas.[108] TSPO is an ideal candidate to study protein expression since it is subject to differential regulation in a variety of diseases. The availability of small molecule ligands further increases its utility for molecular imaging. Our group has synthesized several conjugable analogues of endogenous TSPO ligands[80,111] which have demonstrated their utility for molecular imaging.[70,91,111]

2-2.2 Results and Discussion

2-2.2.1 Synthesis of a TSPO Targeted Bi-modal PAMAM Dendrimer

A TSPO targeted PAMAM dendrimer nanoparticle containing chelated gadolinium and a lissamine fluorophores was prepared as shown in Scheme 4. The synthesis was analogous to our previously reported results with the addition of the DO3A chelators for the attachment of gadolinium ions.[91]

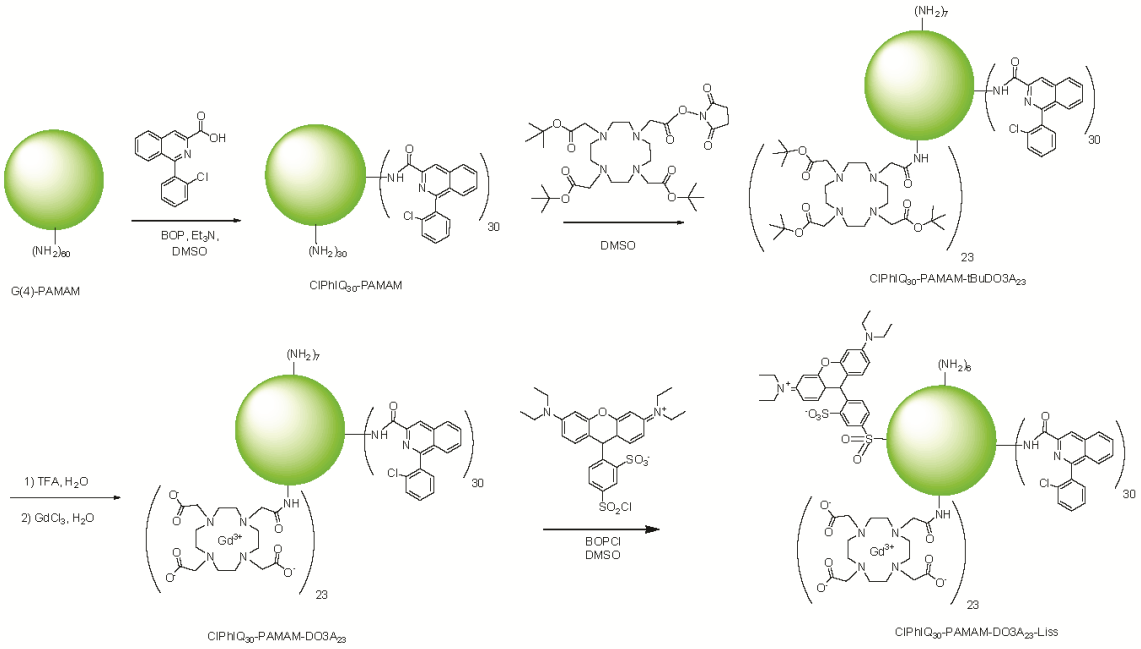

Scheme 4: Synthesis of a bimodal, TSPO targeted PAMAM dendrimer

The TSPO ligand, ClPhIQ acid,[91] was coupled to a generation-4 PAMAM dendrimer using reagent bis(2-oxo-3-oxazolidinyl)phosphinic chloride (BOP) as the coupling agent to give $ClPhIQ_{30}$-PAMAM. The molecule was purified using centrifugal filtration with a 5,000 MW cutoff, and characterized by both NMR and matrix assisted laser desorption ionization (MALDI) mass spectrometry. It was determined that each dendrimer was coupled to an average of 30 ClPhIQ ligands. Next, twenty-three t-butyl protected DO3A chelators were attached to the surface through a reactive succinimide ester to produce $ClPhIQ_{30}$-PAMAM-$tbuDO3A_{23}$. The t-butyl protecting groups were removed by acid hydrolysis in TFA to give $ClPhIQ_{30}$-$PAMAM-DO3A_{23}$ and gadolinium ions were chelated to the DO3A moieties to give the first product, Gd(III)-$ClPhIQ_{30}$-$PAMAM-DO3A_{23}$. To produce the bimodal analogue, a fluorescent dye, lissamine, was

coupled to Gd(III)-ClPhIQ$_{30}$-PAMAM-DO3A$_{23,}$ to give the final product Gd(III)-ClPhIQ$_{30}$-PAMAM-DO3A$_{23}$-Liss.

2-2.2.2 Preliminary Electron Microscopy Studies

The first product, Gd(III)-ClPhIQ$_{30}$-PAMAM-DO3A$_{23,}$ was imaged using transmission electron microscopy (TEM) to determine if the gadolinium ions on the nanoparticle resulted in contrast at the mitochondria. C6 glioblastoma cells were grown to 70% confluence then dosed with a 32 μM solution of Gd(III)-ClPhIQ$_{23}$-PAMAM-DO3A$_{23}$ in media. The cells were incubated with the compound overnight, following which, they were washed with cacadolyte buffer and fixed for one hour in 4% paraformaldehyde. After aldehyde fixation, the cells were post fixed with 1% osmium tetroxide, dehydrated, embedded in resin, sectioned to a thickness of 80 nm and mounted on copper grids. A control sample was also prepared. The cells were imaged on copper grids using a Philips CM20 TEM, and the resulting images are shown in Figure 11.

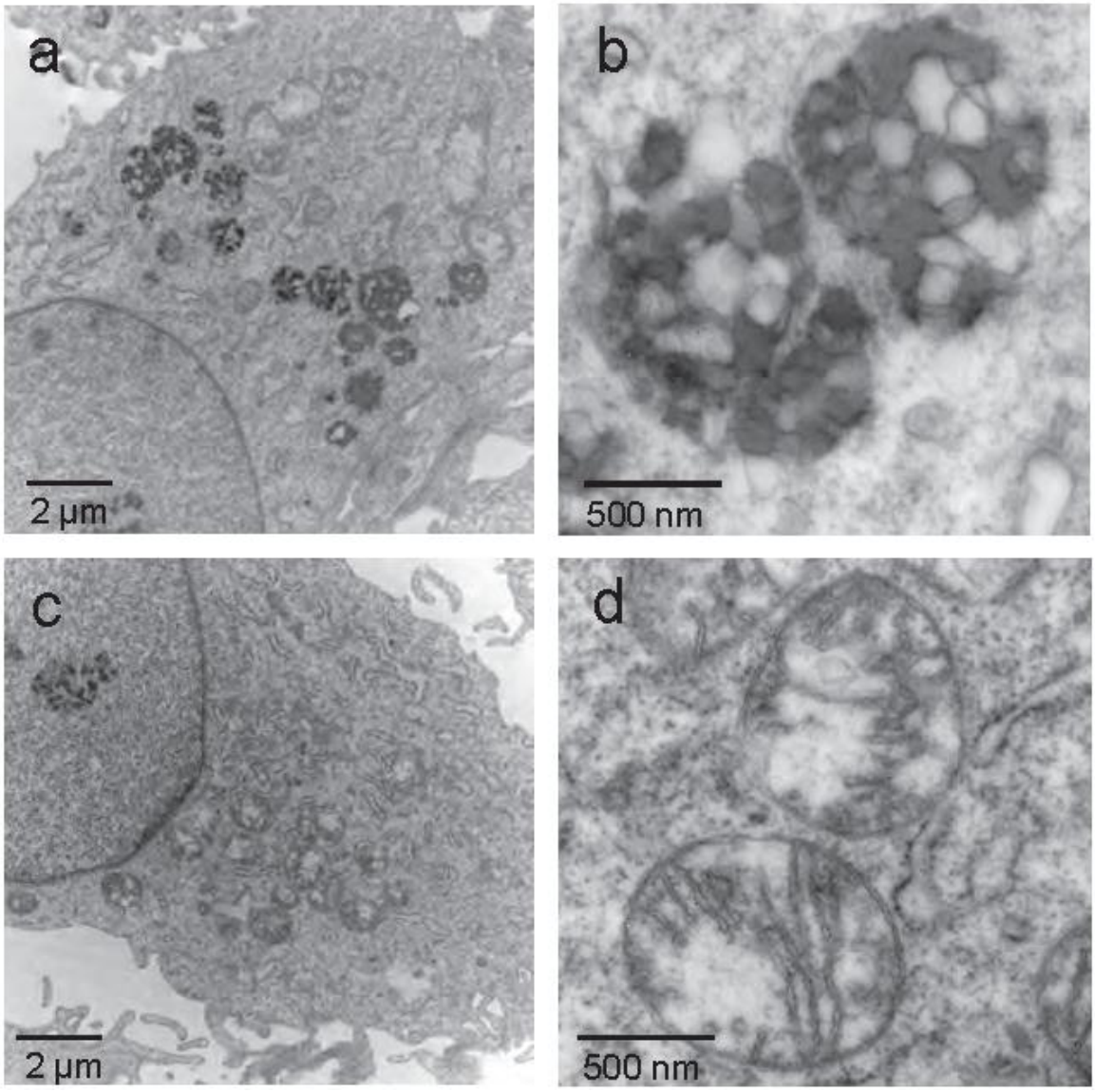

Figure 11: Comparison of TEM images of C6 cells dosed with Gd(III)-ClPhIQ$_{23}$-PAMAM-DO3A$_{23}$ and controls (a) TEM image of a labeled cell. (b). Close up of the mitochondria of the labeled cells. (c) TEM image of a control cell (d) Close of up of the mitochondria of the control cell.
Images: Bernard M. Anderson.

Further analysis using electron diffraction spectroscopy, (EDS) showed that the increased mitochondrial contrast (identified by the square in Figure 12) was due to osmium, not gadolinium.

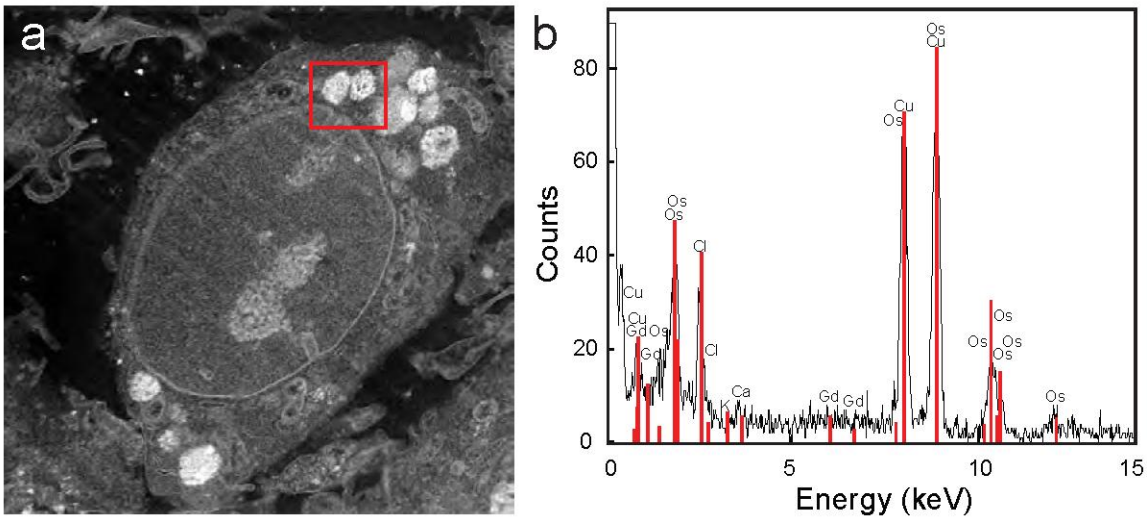

Figure 12: Electron Diffraction Spectra of the mitochondria of C(6) cells dosed with compound Gd(III)-Cl PAMAM-DO3A$_{23}$ (a) STEM Image of sample. (b) EDS spectra of the squared region in a. Image: Ber Anderson

The secondary fixative, OsO_4, which is used to stabilize and add contrast to lipid content, is a strong oxidizer, is capable of coordinating to nitrogen atoms. The coordinated OsO_4 can then react with additional OsO_4 to form large electron dense polymeric structures.[2,112,113] Since the G(4)-PAMAM dendrimer contains 238 secondary nitrogen atoms in its backbone, it presents an ideal scaffold for the formation of such osmium composite. Thus, due to the absence of high-density material at mitochondria of the control, it was hypothesized that that during the postfixation process OsO_4 reacts with dendrimers bound to TSPO receptors located on the mitochondria membrane causing the enhancement in contrast.

We tested this hypothesis by treating samples of Gd(III)-ClPhIQ$_{23}$-PAMAM-DO3A$_{23}$ with either a 1, 16, or 32 mole equivalent of OsO_4. A forth sample containing only a 32 mole equivalent of osmium tetroxide in water was made as a control. Upon addition of the osmium tetroxide to the three Gd(III)-ClPhIQ$_{23}$-PAMAM-

$DO3A_{23}$solutions, a dark brown precipitate formed. A 1 µL aliquot from each of the four samples was placed on 600 mesh, formvar coated copper grids, allowed to dry and imaged at 80 KeV using a Phillips CM12 TEM. It was found that the size and amount of the brown precipitate was dependent on the amount of OsO_4 added. The 1 mole equivalent sample had very small structures ranging in length from 100 to 500 nm. The 16 and 32 mole equivalent samples were much larger with the 32 mole equivalent sample having macrostructures many microns long. For the control, addition of the 32 mole equivalent of osmium tetroxide to water did not yield any brown precipitate during the duration of the experiment. These results confirm our hypothesis that our compound, Gd(III)-$ClPhIQ_{23}$-PAMAM-$DO3A_{23}$, undergoes oxidation with OsO_4 to form electron dense composites.

In order to verify that our TSPO targeted dendrimers are localized at the mitochondria, a lissamine fluorophore was attached to Gd(III)-$ClPhIQ_{23}$-PAMAM-$DO3A_{23}$ to give Gd(III)-$ClPhIQ_{23}$-PAMAM-$DO3A_2$-Liss (Scheme 4). Incubation of 2.1 µM of Gd(III)-$ClPhIQ_{23}$-PAMAM-$DO3A_2$-Liss with C6 glioma cells in conjunction with commercially available Mitotracker green overnight resulted in red fluorescence signal (Figure 13b), due to the lissamine dye. Fluorescence images were obtained using a Nikon Eclipse TE2000-U fluorescence microscope (Lewisville,TX) equipped with Texas Red and FITC filter sets.

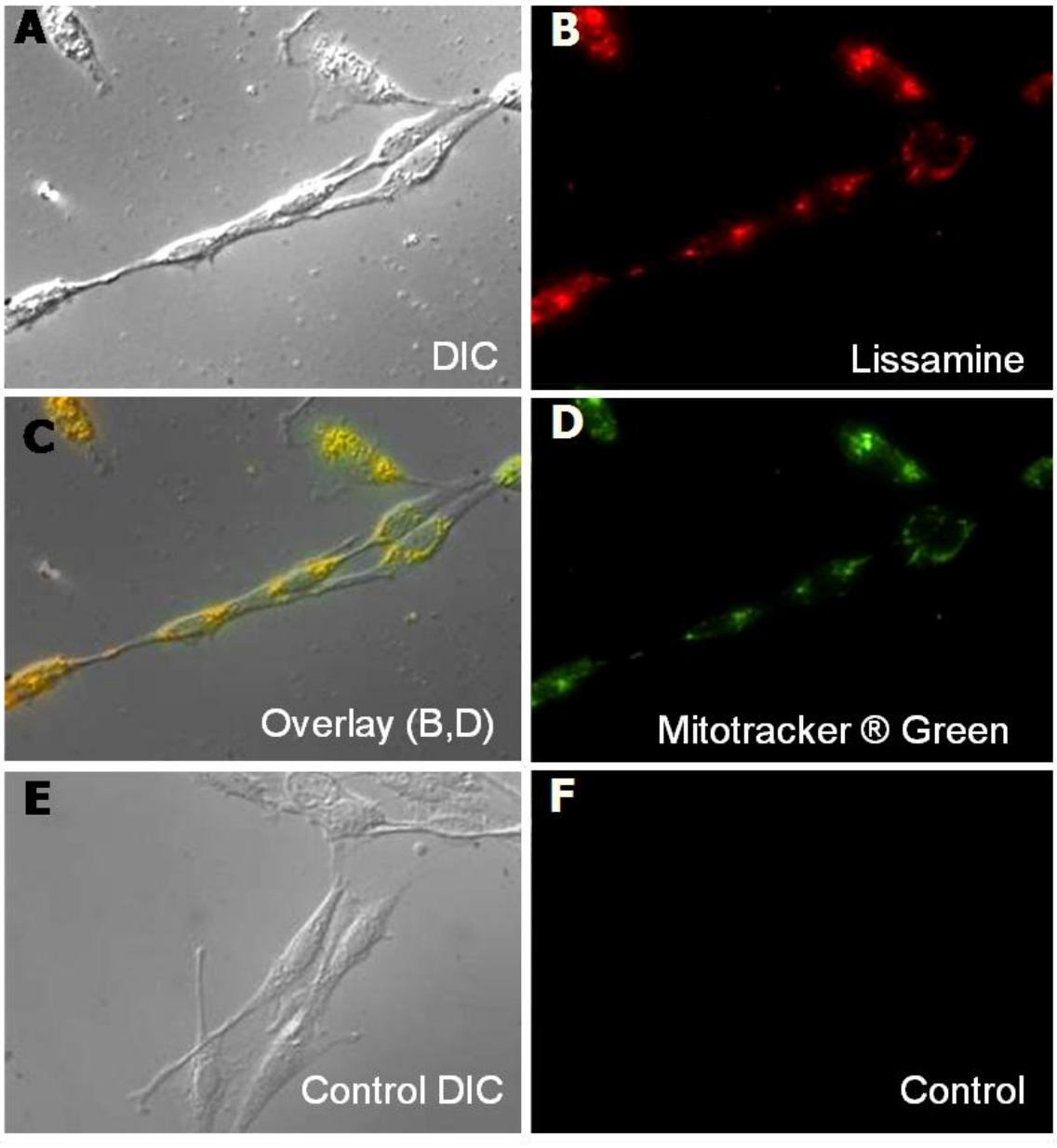

Figure 13: Fluorescence characterization of cellular internalization of Gd(III)-ClPhIQ$_{23}$-PAMAM-DO3A$_{23}$,. (a) Differential interference contrast image of labeled cells. (b) Lissamine fluorescence. (C) Co-registration of lissamine fluorescence with the mitochondria. (d) Green fluorescence due to Mitotracker Green in the mitochondria. (e) Differential interference contrast image of control cells (f) Control cells do not exhibit fluorescence. Image: Lynn E. Samuelson

To confirm that the dendrimer agent was targeting the mitochondria, the cells were co-incubated with Mitotracker Green (Figure 13d). An overlay of the lissamine and Mitotracker Green fluorescence is shown in Figure 13c. Co-registration at the

mitochondria was indicated by the orange color. The control, G(4)-PAMAM- Liss, which did not contain the targeting ligand ClPhIQ showed no mitochondrial fluorescence.

The fluorescence at the mitochondria clearly shows that the dendrimer agents are internalized in the cells, supporting our hypothesis that the high osmium density shown in the EDS spectra (Figure 12b) is a result of OsO_4 forming composites with the PAMAM dendrimers.

To determine if the Gd(III)-$ClPhIQ_{23}$-PAMAM-$DO3A_{23}$-Liss molecule is capable of producing EM contrast by itself, TEM samples were prepared as before, but with the OsO_4 fixation step omitted. C6 rat glial cells were prepared by plating twenty thousand cells per 35mm culture dish and allowing them to attach and grow for two days at 37°C and 5% CO_2. The cells were incubated with 2.1 μM Gd(III)-$ClPhIQ_{23}$-PAMAM-$DO3A_{23}$-Liss in cell media overnight at 37°C and 5% carbon dioxide. Control cells were also prepared in the same manner using a Gd(III)-PAMAM-$DO3A_{15}$ molecule which did not contain the TSPO targeting ligand ClPhIQ. The cells were washed three times (15 minutes per wash) at room temperature with 0.1 M cacodylate buffer to remove media and unbound agent. They were fixed for one hour using 4% paraformaldehyde in cacodylate buffer, to preserve them for sample preparation. No secondary fixation step with osmium tetroxide was performed. The cells were dehydrated with ethanol, and embedded in resin. Modestly thick, 300 nm sections were cut and mounted on copper grids. TEM images were recorded at 80 keV using a Philips CM-12. TEM images of both the OsO_4 stained and unstained cells are shown in Figure 14. Figure 14 shows increased contrast in the cells dosed with targeted compound (Figure 14a and Figure 14b)

over the control cells (Figure 14c and Figure 14d). The loss of ultrastructure details in Figure 14b and Figure 14d is due to the absence of OsO4 secondary fixation.

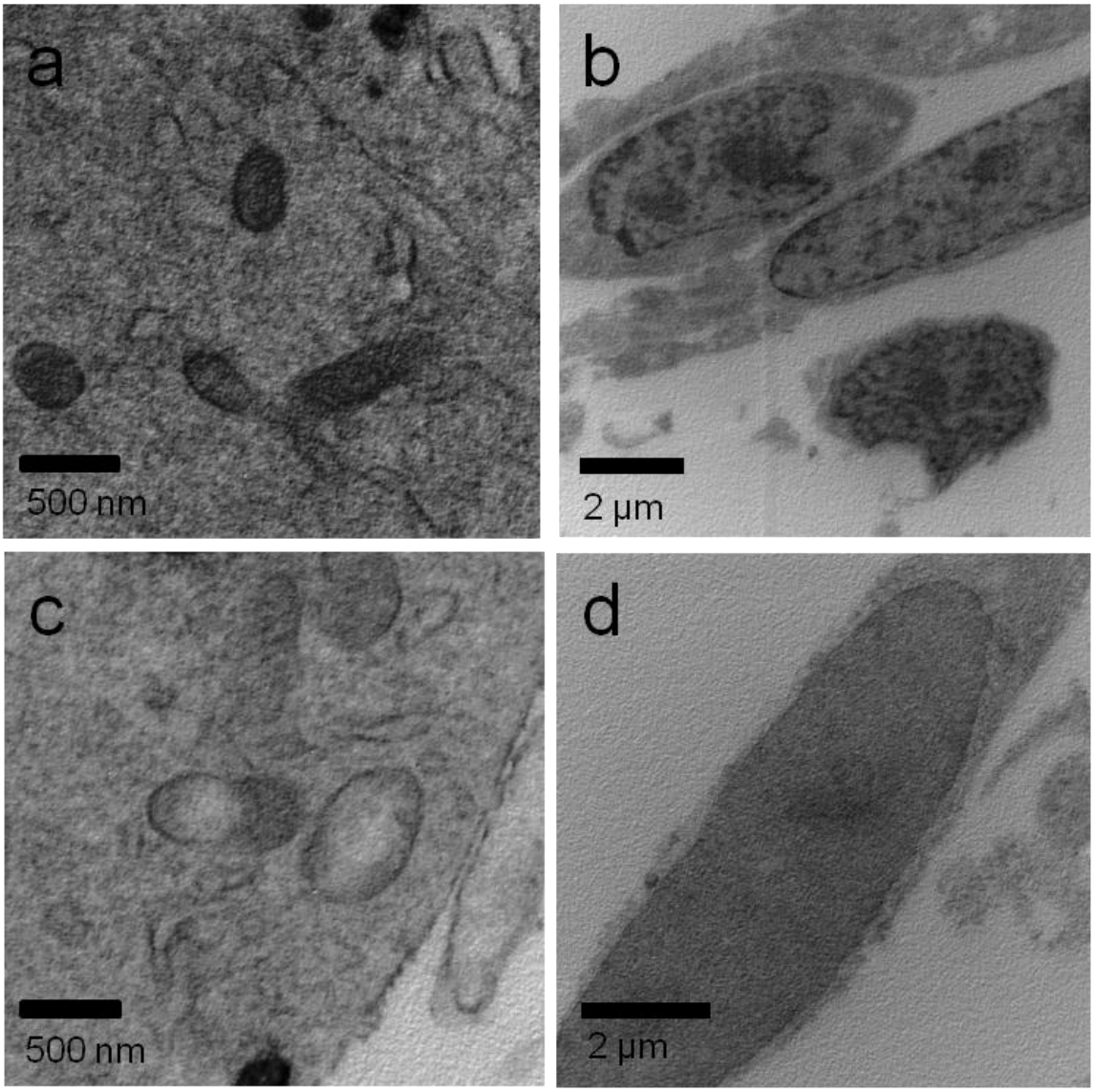

Figure 14: Comparison of OsO4 stained and unstained C6 glioma cells dosed with Gd(III)-ClPhIQ$_{23}$-PAMAM-DO3A$_{23}$-Liss. (a) TEM image of mitochondria of labeled C6 cells stained with OsO_4. (b) TEM image of labeled cells that are not stained with OsO_4. (c) TEM image of mitochondria of control cells stained with OsO_4. (d). TEM image of control cells that are not stained with OsO_4. Images Bernard M. Anderson and Madeline J. Dukes

2-2.3 Conclusions:

A TSPO targeted, bimodal dendrimer containing an organic fluorophore for optical signal and gadolinium ions for EM contrast was prepared and characterized. This molecule was shown to be internalized by cells expressing the receptor of interest. We have demonstrated that the molecule exhibits enhanced EM contrast both with and without OsO_4 staining.

In future, these imaging agents may be applied to electron microscopy of whole cells. Dendrimers are readily internalized by live cells and their surface functional groups provide ample attachment points for chelators, therapeutics, or additional imaging modalities. The gadolinium ions chelated to PAMAM dendrimers, discussed in the previous sections, offer an alternative to bulky metallic nanoparticles for labeling internal receptors.

CHAPTER III

CORRELATIVE FLUORESCENCE MICROSCOPY AND SCANNING TRANSMISSION ELECTRON MICROSCOPY OF QUANTUM-DOT-LABELED PROTEINS IN WHOLE CELLS IN LIQUID

3.1 Introduction

Cellular function is governed by the interaction of molecules with dimensions in the nanometer range, such as proteins, lipids, and deoxyribonucleic acid (DNA). Protein interactions in cells can be studied with fluorescence microscopy.[26] However, the spatial resolution is limited by diffraction to about 200 nm, thus it is not possible to elucidate what happens at the level of individual molecules, for example, in protein complexes. Also, the recently introduced subdiffraction (nanoscopy) techniques[114] do not reach a resolution in the required nanometer range (<10 nm). Cellular ultrastructure is traditionally investigated at the nanoscale with transmission electron microscopy (TEM). TEM imaging requires the preparation of the cells into conventional thin sections or into cryosections. [115] The cells are thus not in their liquid state and not intact (note that TEM imaging can be accomplished on cryogenically frozen samples at the very edge of intact cells). Correlative microscopy is a strategy, developed in the past decade, to combine the functionality of LM with the high resolution of electron microscopy (EM). By introducing fluorescent molecular probes, it is possible to image regions containing a

protein of interest with fluorescence microscopy and then to investigate the underlying ultrastructure with TEM, after preparing a conventional thin section, or a cryosection, of the cell.[50] A certain intracellular process can first be followed with light microscopy (LM), the cell can be fixed, or frozen at a time point of interest, and the sample can then be further studied with TEM.[116] Correlating LM and EM also allows one to search for a region of interest with LM prior to TEM imaging, thus reducing radiation damage induced by searching with TEM.[53] In addition to fluorescence labels, a second tag consisting of an electron-dense material, such as a gold, may be employed. The spatial distribution of a certain type of protein of interest can then be investigated at the nanometer scale with TEM.[72,117] It is also possible to use bimodal probes visible with both fluorescence and electron microscopy, such as dye-conjugated gold nanoparticles, or semiconductor nanocrystal quantum dots (QDs).[118] Different types of proteins can be labeled with QDs of different sizes exhibiting different fluorescence signatures.[65] Finally, electron-dense materials for contrast in TEM may be precipitated via photo-oxidation at the positions of fluorescent labels.[119] The key limitation in correlative fluorescence microscopy and TEM is the need for thin sections, or for cryogenically frozen samples, which complicates experimental procedures and is prone to introducing artifacts.

3.1.1 Liquid STEM

We have recently introduced a novel EM technique for imaging whole eukaryotic cells in liquid[63] or in a wet environment.[120] Eukaryotic cells in liquid are placed in a microfluidic chamber with a thickness of up to 10 μm contained between two ultrathin and electron-transparent windows (see Figure 15a). The specimen is then imaged with a

scanning transmission electron microscope (STEM). Due to the atomic number (Z) contrast of the annular dark-field (ADF) detector of the STEM, nanoparticles of a high-Z material, such as gold, can be detected within the background signal produced by a micrometers-thick layer of a low-Z liquid, such as water. Specific protein labels consisting of nanoparticles can then be used to study the locations of individual proteins in whole cells in liquid. In our initial work,[63,120] surface receptors were labeled with gold nanoparticles and a spatial resolution of 4 nm was achieved.

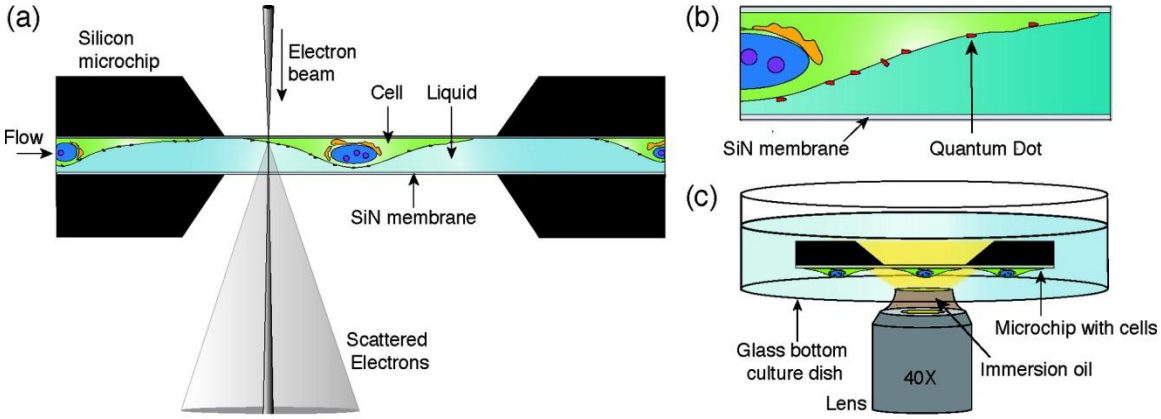

Figure 15: Schematic of the experimental setup for correlative light microscopy and liquid scanning trans electron microscopy (STEM). (a) Microfluidic chamber for liquid STEM consisting of two microchi supporting an electron transparent window. Cells are directly grown on the top microchip. The bottom mi contains a spacer (not shown). This chamber is placed in the vacuum of the STEM and imaged with a s electron beam. Transmitted electrons are detected. (b) Contrast is obtained in liquid STEM on nanop specifically attached to surface proteins of the cell. (c) For imaging with light microscopy, prior to liquic imaging, the microchip with the attached cells is placed upside-down in a glass bottom culture dish and using an oil immersion lens. Images are not drawn to scale.

Here we show that liquid STEM can be used to image QDs bound to surface proteins of eukaryotic cells, and that the STEM images can be correlated with fluorescence images. We also evaluate the signal-to-noise ratio of the liquid STEM images of QDs and determine the achievable resolution. The imaging methodology introduced here allows the imaging of whole fixed cells in liquid with both fluorescence

and EM. There is no additional sample preparation necessary for EM imaging. Cells are grown and labeled directly on the microchips of the microfluidic device. Prior to and after fixation, the samples can be imaged with fluorescence microscopy. Subsequently, the same sample is assembled into a microfluidic system and imaged with STEM, with only a few minutes delay with respect to the first light microscopic imaging.

3.2 Materials and Methods

3.2.1 Preparing the Microchips with COS7 Cells

COS7 (African green monkey fibroblast) cells were grown directly on the silicon microchips for the microfluidic chamber of the liquid STEM system.[63] Each microchip (2.60 × 2.00 × 0.30 mm) supported a silicon nitride (SiN) window of a 70 × 200 μm area and 50 nm thickness (Protochips Inc.). The protective layer of resist coating of the microchips was stripped by rinsing with acetone and subsequent rinsing with ethanol. The microchips were then plasma cleaned to render the surfaces hydrophilic and coated with poly-L-lysine to enhance cell adherence and to maintain the hydrophilic surface. COS7 cells were grown in Dulbecco's modified Eagle medium (DMEM) (Gibco) supplemented with 10% fetal bovine serum (FBS) (Sigma), penicillin/streptomycin antibiotics (100 units/mL and 100 μg/mL, Gibco), and additional l-glutamine (2 mM, Gibco) at 37 °C in a 5% CO_2 atmosphere. Confluent COS7 cells were harvested by rinsing in Dulbecco's phosphate buffered saline (PBS) and dissociating the adherent layer with CellStripper (Mediatech), followed by a quench in supplemented media. The cells were seeded onto the microchips and incubated in medium at 37 °C and 5% CO_2 for 1

day. Prior to labeling, the cells were incubated in serum-free medium for 4 h at 37 °C and 5% CO_2.

3.2.2 Preparing the Spacer Microchips

Each microfluidic chamber for liquid STEM consisted of a microchip with cells and a second microchip with spacers to provide a gap between the microchips for the specimen and for liquid flow. The microchips to be used with the spacer were first stripped of their protective coating with acetone and ethanol. While the surfaces were still hydrophobic, 0.2 μL droplets of an 8 μm diameter polystyrene microsphere suspension in water were pipetted onto the four corner regions of each microchip. The droplets of the suspension were dried, leaving the microspheres stuck to the four corners of the microchips' surfaces. The chips were then plasma cleaned to render the surfaces hydrophilic and coated with poly-L-lysine.

3.2.3 EGF-QD Labeling

QDs with 655 nm emission (QD_{655})were coupled to EGF molecules via biotin−streptavidin binding.[121] The EGF-QD complexes were formed by incubating EGF-biotin (Invitrogen) in a 6:1 molar ratio with streptavidin-QD_{655} (Invitrogen) for 2 h at room temperature in a solution of 1.3 μM QD in 50 mM borate buffer, pH 8.3 (the QD stock solution was first centrifuged to remove aggregates). Free EGF-biotin was removed with a microcentrifuge purification column (Ultracel-100YM, Millipore). For specific labeling of the EGF receptors, the cells were incubated with 5 nM EGF-QD_{655} in Tyrode's buffer (Sigma), supplemented with 0.1% BSA (Sigma) and 50 mM d-glucose (Sigma-Aldrich) for 5 min at room temperature by immersing the microchips in

incubation liquid.[63] The cells were then washed three times in PBS (Gibco) and fixed for 20 min with 4% glutaraldehyde in PBS. After fixation, the cells were washed three times with PBS and once in 10% PBS. The aldehydes in the fixative were quenched by incubating the microchips in 100 mM glycine in 10% PBS, followed by three rinses of the microchips in 10% PBS. Two different control experiments confirmed specific EGF labeling with QDs. The first control started with the above-described labeling of the cells with EGF-QDs. The control samples were then desalted, dried, and imaged with TEM. It was found that QDs were co-located with regions of the microchips containing cellular material. The second control involved the incubation with QD_{655}-streptavidin without EGF-biotin. This control was also desalted, dried, and imaged with TEM. Only a very low amount of nonspecifically bound QDs was observed.

3.2.4 Light Microscopy

The microchips with the labeled cells were placed upside-down in a 35 mm culture dish with thin glass bottom (Mat-tek), containing 2 mL of 10% PBS in water. Differential interference contrast (DIC) and fluorescent images (5 s exposure time) were recorded with a 40× oil immersion objective using a wide field microscope (TE300, Nikon) equipped with a far-red band-pass excitation filter (hq615/40 ×) and a far-red band-pass emission filter set (hq710/100 m). Fluorescence of the glutaraldehyde fixative was reduced prior to imaging by photobleaching, using the light source of the fluorescence microscope. The images were adjusted for optimum brightness and contrast, overlaid, and colored using ImageJ software (NIH).

3.2.5 Liquid STEM Imaging

For liquid STEM imaging, a microfluidic chamber containing a sample was assembled in a liquid specimen holder for STEM imaging (Protochips Inc.). This holder connected the specimen chamber to a syringe pump (Harvard Scientific) via microfluidic tubing (Upchurch Scientific). Before assembly, the tubing was cleaned with purified water and then the slot for the microchips was dried. The spacer microchip was first loaded with the spacer facing up. A droplet of 0.5 μL 10% PBS was pipetted onto the surface, wetting it completely. The microchip with cells was then placed in the slot on the spacer microchip with the cells facing downward. The loading was done rapidly to prevent the chips from drying. The lid of the holder was then closed, the buffer solution was rinsed off the outer surface of the microchip to prevent the formation of a salt crust, and a 1−2 μL/min flow of 10% PBS in water was initiated. The STEM (CM200, FEI Company, Oregon) was set to 200 kV, and a beam semiangle α of 11 mrad, a pixel dwell time of 20 μs, a probe current of 0.6 nA, a detector semiangle β of 70 mrad, and an image size of 1024 × 1024 pixels were chosen. The probe size containing 50% of the current was estimated to be d_{50} = 0.6 nm.[122] Contrast and brightness were adjusted for maximum visibility, and a convolution filter with a kernel of (1, 1, 1; 1, 5, 1; 1, 1, 1) was applied (using ImageJ) to reduce the noise in the STEM images; however, the data analysis via line scans was performed on the original, unfiltered data. The image of Figure 16c was recorded at the edge of the SiN window where the window bulged in the vacuum toward the center of the window, resulting in a change of the background signal level as a function of the vertical coordinate. This increase in background signal was compensated for by using image processing (Digital Micrograph, Gatan).

3.3 Results and Discussion

3.3.1 Correlative Fluorescence Microscopy and Liquid STEM of QD-Labeled Cells

COS7 fibroblast cells were grown on silicon microchips with electron transparent windows for liquid STEM imaging.[63] The cells were incubated for 5 min at room temperature with EGF conjugated to QD (EGF-QD) and then fixed with glutaraldehyde. The incubation with EGF-QD and the fixation were done directly on the microchips. The cells on one microchip were imaged with LM with the microchip placed upside-down in a cell culture dish with phosphate buffered saline water (Figure 15c). Figure 16a shows a direct interference contrast (DIC) image and overlaid fluorescence image of a window section partly covered with adhered cells. The cells have flattened-out on the SiN surface of the microchip. The DIC signal is visible through the SiN window only, while the fluorescence signal is visible over the whole surface. The fluorescence signal is co-located with cellular material visible in the DIC signal. Figure 16b shows the fluorescence image separately. The QD labels light up as bright spots against a dark background of regions without cells. The cellular regions contain a faint fluorescence signal from the glutaraldehyde fixative. Bright spots indicate the locations of single QDs and/or bigger clusters of QDs, distributed over the entire surface of the cell, as expected for the used incubation time.[123] The fluorescence image (Figure 16b) was also used to locate the position of the cell with respect to the window, in order to correlate the light microscope and STEM images. Fluorescence and DIC images were recorded for six other samples.

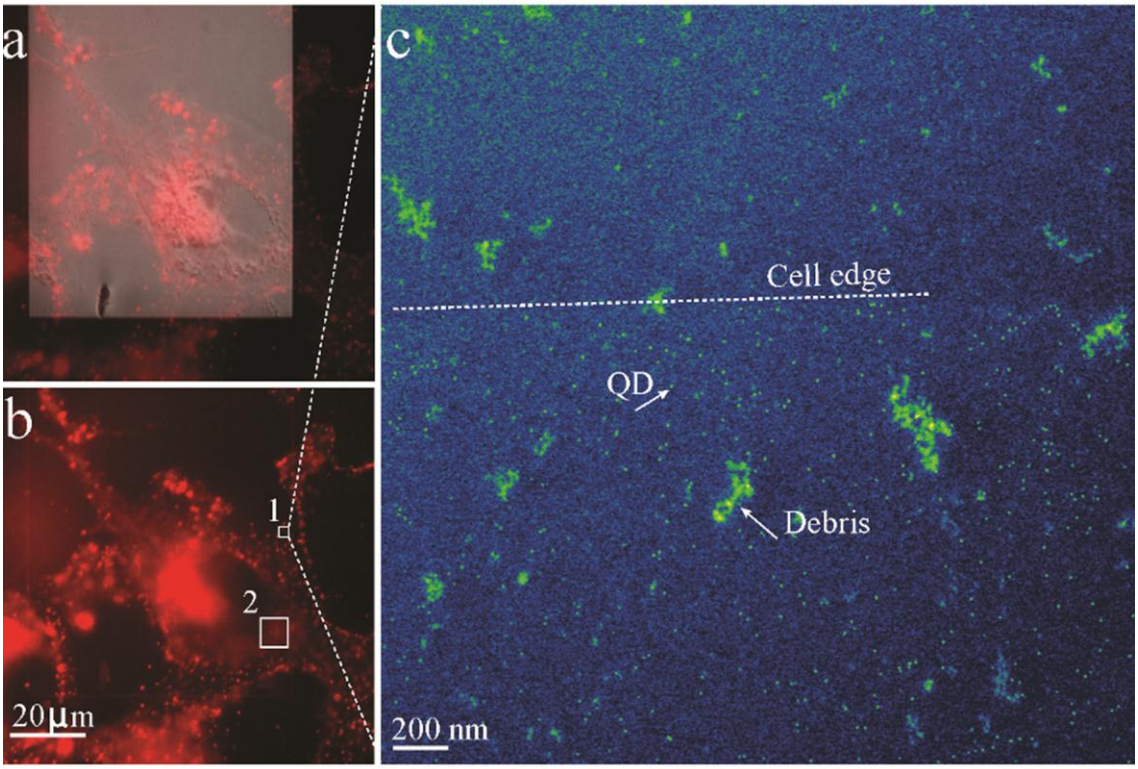

Figure 16: Correlative light microscopy and liquid STEM of intact fixed eukaryotic cells in saline water. (a interference contrast (DIC) image (gray) with overlaid fluorescent signal (red) of a microchip with CO showing the regions with quantum dot (QD)-labeled epidermal growth factor (EGF) receptors. The rec shape outlines the silicon nitride window. (b) Fluorescent signals (red) showing cellular regions with EGF re Some fluorescence from the fixative is also visible. (c) Liquid STEM image of the region indicated with a sc in (b). Individual QDs along the edge of the cell can be discerned as yellow spots on a blue backgrounc debris can be seen, as well. The magnification was M = 48 000. The signal intensity was color-coded to incr visibility of the labels.

Selected microchips with labeled cells in the window region were assembled into microfluidic chambers for liquid STEM and imaged with a 200 kV STEM at a magnification M = 48000, while a continuous flow of buffer was maintained over the cells. Figure 16c shows a STEM image recorded at the edge of the same cell in the fluorescence image in Figure 16b. The lower two-third of the image contains bright spots of similar sizes that we associate with the presence of QDs. These bright spots are absent in the upper part of the image. We interpret the indicated transition line as the edge of

the cell. Some debris from the microchip processing is visible, as well. Similar debris material was observed incidentally on microchip windows before cells were seeded and is residual material from the microchip processing that was not entirely washed off.

The QD-labeled EGF receptors were distributed almost evenly over the surface of the cell, consistent with the well-known behavior of the EGF receptor. Prior to EGF binding, the EGF receptor is known to be homogeneously distributed on the plasma membrane, as was shown by others via thin section TEM imaging of ferritin-labeled EGF[124] and of immuno-gold-labeled EGF receptors.[125] Incubation with EGF leads to ligand binding, activation of the receptor, and eventually internalization of the receptor via the formation of endocytotic vesicles after typical incubation times on the order of 30 min at room temperature.[123] The distribution of the labels thus changes with time from a homogeneous distribution to clusters of labels. The receptor distribution cannot be studied at the single-receptor level using fluorescence microscopy, so a microscopy technique with a resolution in the nanometer range is needed, for which traditionally TEM on thin sections is used. Figure 16c demonstrates that liquid STEM imaging provides information about the distribution of the individual EGF receptors correlated with the fluorescence image.

3.3.2 Liquid Thickness

To verify the presence of liquid in the microfluidic chamber, we have determined the fraction, N/N_0, of electrons in the probe, N_0, scattered onto the ADF detector by the liquid in the microfluidic chamber. A fraction of $N/N_0 = 0.44$ was measured during imaging. The thickness of the liquid T follows from this fraction as[63] with $l(\beta)$ being the mean free path length for elastic scattering in opening semiangle β or larger.

$$T = -l(\beta)\ln\left(1 - \frac{N}{N_0}\right) \qquad (\mathbf{5})$$

Equation **5** assumes that most of the signal in the ADF detector is formed by single elastic scattering events and thus neglects multiple scattering and inelastic scattering. It was demonstrated in a recent study that the values of *T* obtained with **5** were accurate within 30% compared to thickness measurements performed via tilting the sample.[126] Water has l_{water} = 10.5 μm for β = 70 mrad.[63] Note that the mean free path length for the total elastic cross section (scattering by angles of 0−π) for water at 200 kV is 0.43 μm, but most scattering events lead only to minor angular changes of the electron trajectories and do not cause electrons to scatter into the ADF detector. The larger mean free path length for the partial elastic cross section (scattering by angles of β−π) applies for angular changes sufficient to scatter electrons into the opening angle of the ADF detector. The value of l_{water} approximately equals the value of the buffer solution used here. The thickness of the liquid at the position of Figure 16b was calculated to be 6 ± 1 μm. This number is smaller than the diameter of the applied microspheres serving as spacer between the two microchips. Presumably, a compression of the microspheres occurred.

Localizing the same region in both a LM and an EM image often requires dedicated procedures in correlative microscopy.[65,127] For liquid STEM, the localization was accomplished with a simple procedure as described in the following. The positions of features in the fluorescence image were measured with respect to the frame of the SiN window, visible in Figure 16a as rectangular shape and visible as a thin line in Figure 16b. Because the magnification used for the STEM imaging was too high to display the

entire window area, the position of one corner of the SiN window was located first. The stage position at this point was recorded, and the scan rotation was aligned such that the scan direction of the electron beam ran parallel to the short side of the SiN window. During STEM imaging, the stage position of each image was recorded and correlated with the prior determined frame position of the SiN window. The position of Figure 16c corresponds to the square #1 in Figure 16b. The position of the square in the fluorescent image is at the edge of the cell, consistent with the finding of a separation line between regions with and without QDs in Figure 16c, interpreted as a cell edge.

A second region of the same cell is shown in square #2 of Figure 16b. Several STEM images were recorded in this area. Figure 17a shows an image recorded at M = 16000. The thickness of the liquid at this position was measured to be 5 ± 1 μm, consistent with the thickness determined for the region of Figure 16b within the accuracy of the measurement. The cellular material is visible as white irregular shapes, and the signal intensity increases toward the upper left corner to a level where the detector clipped. Cellular material has a shorter l value than water ($l_{cell} < l_{water}$) due to the higher average density and the higher average atomic number of protein, lipid, and DNA. Thus, a cellular region with a high density of protein, lipid, or DNA is expected to produce more scattering than water. The region in the upper left corner of Figure 17a can thus be interpreted as a region of the cell where it is denser or thicker than in the remaining region. This finding is consistent with the fluorescence image of Figure 16b, where the square #2 is located in proximity to the nucleus. It can thus be concluded that correlative fluorescence microscopy and liquid STEM was accomplished on QD-labeled EGF

receptors in whole COS7 cells in liquid. STEM images of two other samples also showed QDs in the cellular regions of the corresponding fluorescence image.

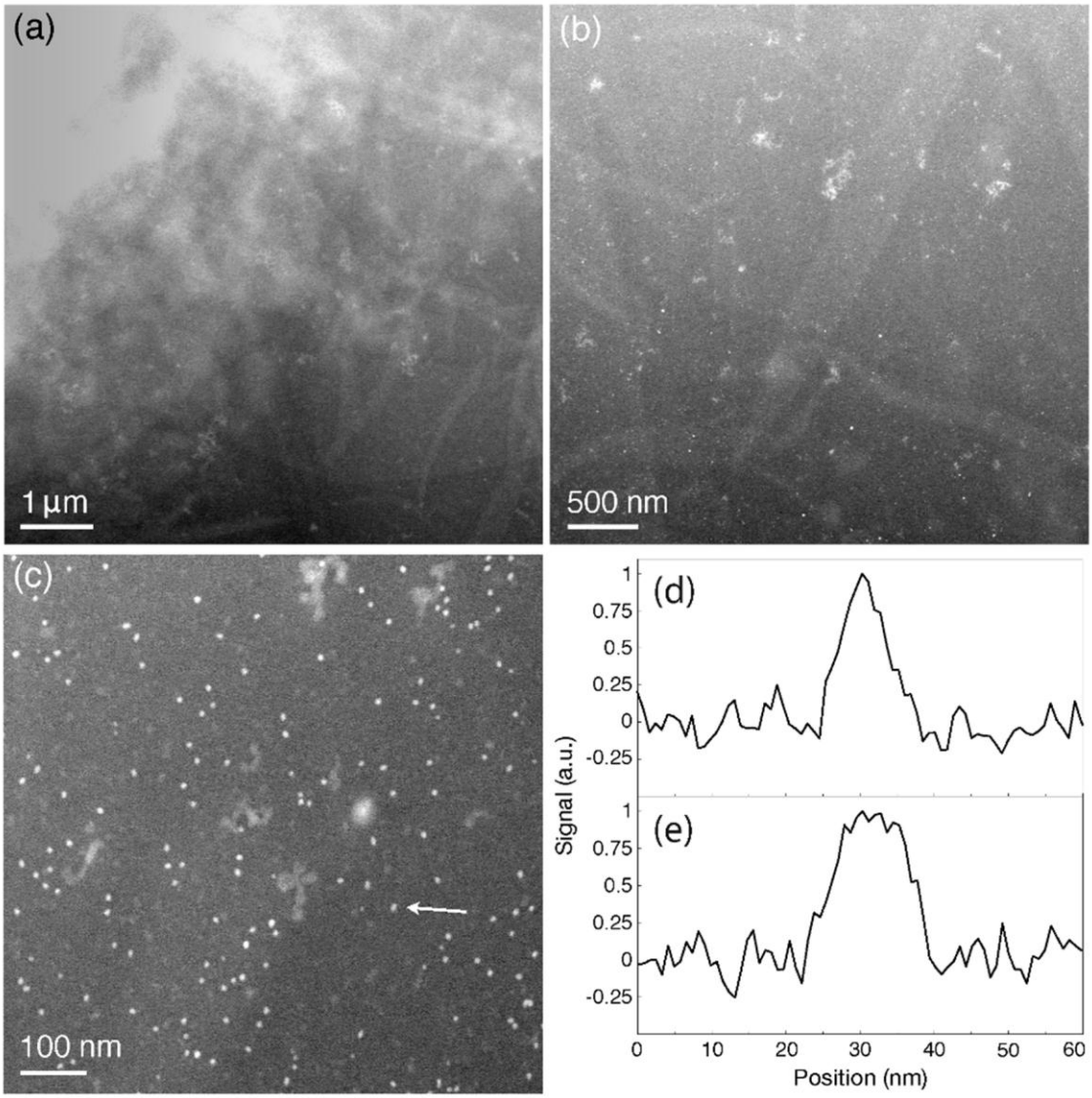

Figure 17: Liquid STEM images of a COS7 cell labeled with EGF-QD. (a) Cellular region at the position o square #2 in Figure 16 recorded at M = 16 000. (b) Image recorded at a region just at the bottom of the figur at M = 32 000. QDs are visible as bright spots. (c) Image recorded at M = 160 000 revealing the shape of the (d) Line scan over the QD indicated with the arrow in (c) over the short dimension of the QD. (e) Line scan the same QD as in (d), but over the long dimension. The background level was set to zero.

3.3.3 Resolving the Shape of the QDs

Liquid STEM images were recorded at higher magnifications, as well, to determine the shape of single QDs. Figure 17b was recorded at M = 32000, where some of the cellular material can still be discerned and the QDs are visible as small bright spots. Figure 17c, recorded at M = 160000, reveals the oval shape of the individual QDs. While the cellular material cannot be distinguished anymore, some of the debris is visible. A third type of object is the larger oval shape, center right, which is caused by electron beam contamination; that is, it appeared during imaging. The QD at the arrow was further analyzed. The line profile over the short dimension is shown in Figure 17d with a full width at half-maximum (FWHM) of 7 nm. The line profile over the long dimension has a FWHM of 12 nm, as shown in Figure 17e. The oval shape of the QDs was also detected by others, and STEM images at atomic resolution showed a bullet-like shape of QDs of the CdSe/CdZnS core/shell materials[40] that are used by the supplier (Invitrogen).

A total of 10 QDs was analyzed via line scans over their small dimensions, and it followed that the average FWHM was 8 ± 1 nm. The measured FWHM of the small dimension is consistent with the size of the CdSe core (7.3 nm) surrounded by a ZnS shell, which adds an additional 1−2 nm.[40,128] The protein coating of the QDs is not visible in the STEM image due to the lower atomic number of this material compared to the core, and the resulting lower contrast in STEM. It can thus be concluded that QDs were indeed observed with liquid STEM and that the resolution was sufficient to resolve the oval shape of the QDs in a 5 μm thick layer of water (buffer).

3.3.4 Evaluation of the Signal-to-Noise Ratio of the Liquid STEM Images

The signal-to-noise-ratio (SNR) of the peak of the signals at the QD with respect to the background level was 9 ± 1. The noise level was the standard deviation of the signal in a line scan over the background near the QD. The experimental SNR can be compared with a theoretical prediction. From the equations for elastic scattering[129] and assuming 100% detection efficiency, it follows for the imaging of QDs in several micrometers of water that the noise-limited spatial resolution, d, obtained on the QDs is given in equation **6**.[63,126]

$$\mathrm{d} = \mathrm{SNR}\cdot l_{\mathrm{QD}}\sqrt{\frac{\mathrm{T}}{N_0 l_{\mathrm{water}}}} \qquad (\mathbf{6})$$

This equation gives the relationship between the QD size and the SNR in the image. With the density of the CdSe core of 5.8 g/cm^3,[130] and a molecular weight of 14 g/mol, it follows that l_{QD} = 0.40 μm. Equation **6** predicts QDs with d = 9 nm to be visible with SNR = 9 for T = 5 μm and the microscope settings used here. This theoretical value corresponds to the experimental fwhm values of 7 and 12 nm for the short and long side, respectively. The FWHM is a measure of the size of the QD but is not necessarily equal to the actual diameter. The line scan represents a convolution of the object with the electron probe from the STEM imaging, but for our microscope settings, the electron probe size was about 0.6 nm, measured as the diameter containing 50% of the current, d_{50}, and the FWHM can be considered as a sufficiently accurate measure of a QD

dimension. It can thus be concluded that the theoretical model predicts the outcome of the measurements within the accuracy of the measurements and of equation **6**.

3.3.5 Resolution of Liquid STEM on QDs

We have also determined the spatial resolution achieved in this experiment. For a situation where the electron probe is much smaller than the imaged object, a measure often used to determine the spatial resolution is the 25−75% edge width, r_{25-75}.[131] Values of r_{25-75} were measured from the line scans over the QDs. Each r_{25-75} was determined from the average of the opposite edges of a line scan over the QD. The values of r_{25-75} for the QD of Figure 17: Liquid STEM images of a COS7 cell labeled with EGF-QD.d amounted to r_{25-75} = 3 nm. This value was the same for line scans over the long and short dimensions. The average over the small dimension of 10 QDs was 3.0 ± 0.5 nm. Thus, the spatial resolution achieved with liquid STEM of QDs on cells in buffer for T = 5 μm was 3 nm. This estimate applies for QDs in the upper region of the specimen with respect to the beam entrance. Interactions of the electron beam with the water will lead to beam broadening. At a depth of 0.5 μm, the electron probe will have increased to 4 nm,[63,120] still providing sufficient resolution, but at a depth of 1 μm, the probe size will be 9 nm and the QDs will be on the onset of visibility. QD-labeled receptors can thus be detected in many sections of the cells flattened on the SiN membrane.

Biological EM is mostly limited by electron beam damage, and the resolution is then not limited by the electron probe size, but rather by the available electron dose. The minimum size, d, of a nanoparticle that can be resolved with a certain electron dose is calculated with **6**. The Rose criterion[132] sets the limit SNR = 5, and the electron dose

determines N_0. The pixel size in Figure 17 was 0.85 nm, larger than the d_{50}, and the electron dose was thus 1.0×10^5 e^-/nm^2. This value is an order of magnitude larger than the limit of 8.0×10^3 e^-/nm^2 used in cryo-TEM of whole cells[133] and about a factor of 4 less than the limit used for the imaging of conventional thin sections.[134] A dose of 7×10^4 e^-/nm^2 applies for STEM imaging of fixed cells in liquid. An electron dose of 1.0×10^5 e^-/nm^2, SNR = 5, and T = 5 μm, yield d = 5 nm. QDs with a smallest dimension of 5 nm would thus be visible with sufficient SNR for detection.

3.3.6 Difference between STEM and TEM

The STEM has a key advantage over TEM when imaging molecular labels of heavy materials, such as gold nanoparticles or QDs, and the obtained images are different than those obtained with TEM. The molecular labels are visible with high contrast, while the underlying ultrastructure is visible with much less contrast than in TEM. This "absence" of information has the advantage that the background levels are relatively low, thus promoting the visibility of the labels when imaging whole cells. The difference between STEM and TEM has its analogue in LM, where fluorescence microscopy is used to image specifically labeled proteins and, for example, phase contrast is used to image the cellular structure. Correlative fluorescence microscopy and liquid STEM thus provides different information than correlative microscopy involving TEM.

3.4 Conclusions

These results demonstrate that liquid STEM is capable of imaging individual QDs used as specific protein labels on whole eukaryotic cells in liquid, and that the liquid

STEM images can be readily correlated with their fluorescent counterparts. The sample preparation method used for liquid STEM is similar to standard methods used for LM with the difference that nanoparticle labels of heavy materials are needed to provide contrast in STEM. Liquid STEM has two key advantages over state-of-the-art correlative LM and TEM, requiring thin sections, or thin frozen samples: (1) Artifacts introduced by dehydration, post-staining, freezing, or sectioning are avoided. (2) In liquid STEM, cells are labeled live and fixed, after which no further sample processing is required. As a consequence, fluorescence microscopy can be used to monitor tagged proteins in living cells to determine the desired time point of the fixation. It is thus possible to examine a certain specific state of the cell by subsequent liquid STEM imaging. Currently, liquid STEM is limited to surface proteins and proteins that internalize as was shown for the EGF receptor,[63] but strategies for introducing nanoparticles into live cells, such as membrane penetrating peptides,[135] may be used to label intracellular proteins in the future. The spatial resolution of 3 nm demonstrated here is sufficient to discriminate nanoparticles differing in size, shape, and electron density for multilabel experiments to study the constituents of protein complexes within cells.

CHAPTER IV

THREE-DIMENSIONAL LOCATIONS OF GOLD-LABELED PROTEINS IN A WHOLE MOUNT EUKARYOTIC CELL OBTAINED WITH 2.5 NM PRECISION USING ABERRATION CORRECTED SCANNING TRANSMISSION ELECTRON MICROSCOPY.

Adapted with permission from: Three-Dimensional Locations Of Gold-Labeled Proteins in a Whole Mount Eukaryotic Cell Obtained with 3 nm Precision Using Aberration-Corrected Scanning Transmission Electron Microscopy, *Journal of Structural Biology* **2011**, *In Press*

4.1 Introduction

The biological processes responsible for cellular function are controlled by complex macromolecular systems, which are assembled from individual proteins and other biological components such as lipids and DNA. Accurate three dimensional (3D) maps of the spatial organization(s) of such bio-molecular assemblies within a whole cell provide a blueprint for investigating biological mechanisms.[6,136] Tomographic techniques using transmission electron microscopy (TEM) are typically employed to obtain nanometer-scale reconstructions of cellular structures in 3D;[5,115] however TEM tomography is limited to maximum sample thicknesses of ~300 nm,[137] or a maximum of ~1 μm when using energy filtering techniques.[6] TEM imaging of a -in terms of electron microscopy (EM)- large structure, such as a whole cell, is not possible with tilt-series TEM tomography, because the beam must penetrate through micrometers of cellular material at the high tilt angles. Thus, TEM imaging of whole eukaryotic cells is generally confined to the periphery, where the cellular material is thin enough to be

contained within a single plastic section, or thin enough for reliable formation of vitrified ice for cryo-TEM preparation.[138] One procedure to image the cytoskeleton of whole mount cells involves the extraction of the cellular membrane and cytosolic proteins.[138] However, such procedure eliminates the possibility of imaging membrane or cytosolic structures and thus cannot be considered for imaging an intact system.

Although long assumed to be too damaging for imaging biological structures,[60] scanning transmission electron microscopy (STEM) has begun to gain acceptance as a technique for imaging thicker biological samples by both tomographic and focal-series techniques.[16,60,137] Recently, our group introduced the use of aberration-corrected STEM to obtain 3D reconstructions of biological structures with nanometer resolution.[16,59] Spherical aberration corrections allows electron beam opening semi-angles (α) of up to 40 mrads, compared to conventional STEM with $\alpha \cong 10$ mrad, while maintaining a high lateral resolution. On account of the increased opening angle a depth of field of several nanometers is obtained.[139] 3D information of a biological specimen is obtained via the recording of a series of 2D images at different focus positions (Figure 18), a so-called focal series, and subsequent deconvolution[59]

Here we present an optimized method to prepare whole mount eukaryotic cells for TEM or STEM imaging. Existing protocols[3,9,42,140] were optimized so that critical point dried, whole cells remained stable under the irradiation conditions of the STEM. We developed a quantitative method to analyze the sample stability in response to the electron dose using TEM imaging. The whole mount samples were imaged with aberration-corrected STEM, and several 3D focal series were obtained.

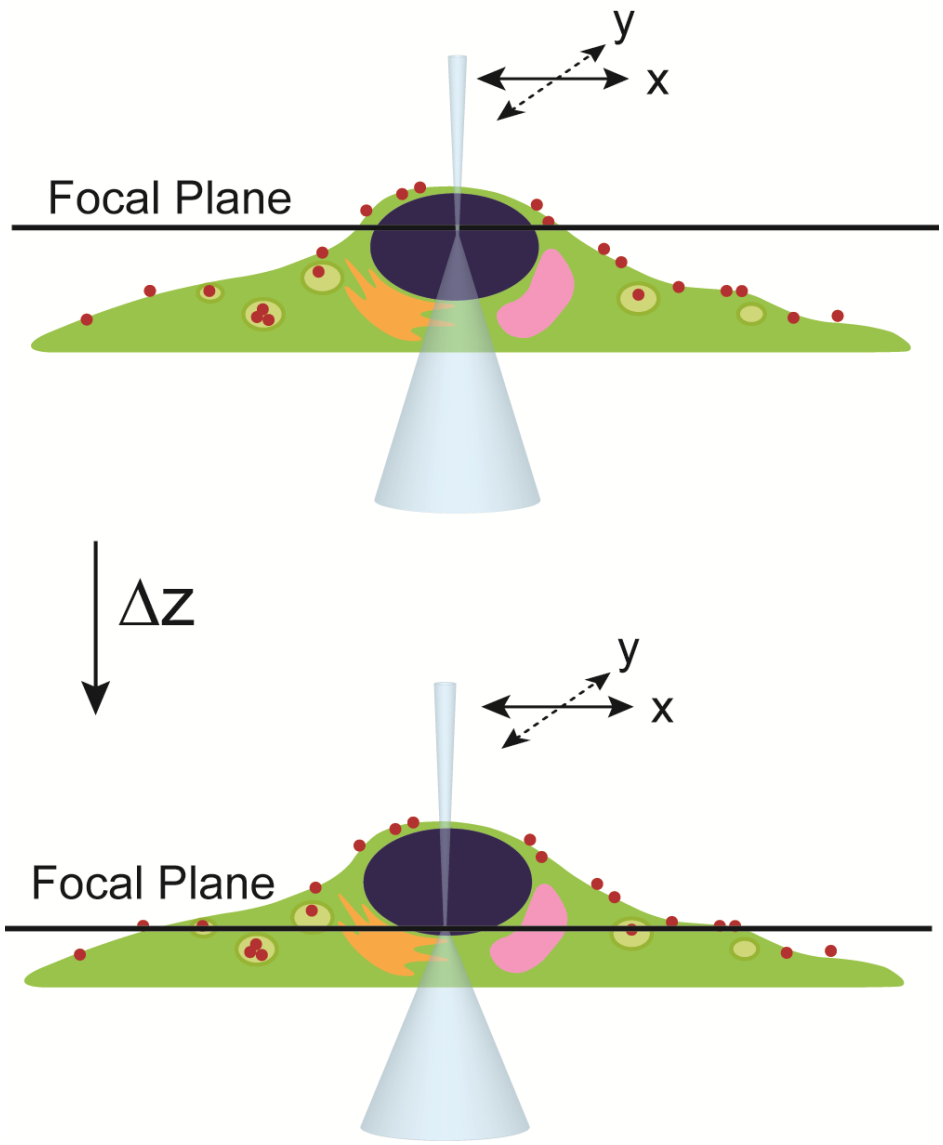

Figure 18: Image acquisition using aberration-corrected three-dimensional (3D) scanning transmission electron microscopy (STEM). The electron beam is scanned across the sample in the x,y plane at different focus positions, z. The cells are grown on a silicon nitride support window on a silicon microchip. Strong contrast is obtained on gold nanoparticles used as specific protein labels.

The contrast mechanism of STEM using the annular dark field detector is especially suited to image heavy nanoparticles in a thick layer of a light material.[59] For this reason we have labeled the epidermal growth factor (EGF) receptor with gold nanoparticles. The datasets were analyzed for the 3D positions of the labels on the cell.

4.2 Materials and Methods

4.2.1 Sample Preparation

Cells were grown directly on the EM sample supports, silicon microchips each with an electron transparent silicon nitride (SiN) window of an area of 250 x 250 μm^2, and 100 nm thickness (Protochips Inc, NC, and Nordaca Inc., Canada). The microchips were rinsed in ethanol for 2 minutes and then plasma cleaned (Harrick Plasma, NY) for 5 minutes. Next, the microchips were coated with poly-L-lysine (0.01%, Sigma, MO) to promote cell adherence to the SiN, by incubating them in solution for 5 minutes at room temperature. The microchips were then rinsed three times with HPLC-grade water (Fisher Scientific, PA) and placed, with the SiN surface facing upwards, into wells of a 96 well plate filled with Dulbecco's modified eagle medium (DMEM) (Invitrogen, CA) supplemented with 10% fetal bovine serum (FBS) (Sigma, MO).

Confluent COS7 cells (green monkey kidney fibroblast) were harvested from a 25 mL culture flask after detachment with trypsin and re-suspended in 5 mL of serum supplemented DMEM. A droplet of the suspended cell solution was added to each well, and cell adherence to the microchip was monitored using an inverted microscope (TS100 Nikon Instruments). The microchips were then transferred to new wells containing fresh media. Cells were grown in an incubator for four hours at 37 ºC in air with 5% CO_2. Thereafter they were rinsed with serum-free DMEM, and transferred to wells filled with serum-free DMEM, where they were incubated overnight at 37º C in air with 5% CO_2.

4.2.2 Receptor Labeling

EGF receptors were tagged using EGF conjugated to 10 nm gold nanoparticles (EGF-Au). Gold-streptavidin nanoparticles (KPL, MD) were coupled to biotin labeled EGF (Invitrogen, CA) using a previously described method.[63] The cells were incubated with 5 nM EGF-Au solution for 5 minutes at room temperature, followed by rinsing and fixation.

4.2.3 Primary Fixation

COS7 cells were fixed directly on the EM support using 4% glutaraldehyde in phosphate buffered saline (PBS, Electron Microscopy Sciences, PA).[63] Samples were immersed at room temperature in fixative for periods of 15, 30, 45, or 60 minutes. After fixation, they were rinsed three times with PBS (5 minutes each) followed by three rinses with 0.1 M cacodylate buffer (Ted Pella, CA), 5 minutes each, to remove residual fixative.

4.2.4 Staining and Secondary Fixation

Fixed cells were stained with OsO_4 by immersing the samples in solutions of either 40 mM, or 40 nM OsO_4 (Ted Pella, CA) in 0.1 M cacodylate buffer at room temperature for one hour.[3] Controls without OsO_4 were incubated in cacodylate buffer only. Samples prepared from different concentrations (0, 40 nM, and 40 mM) were processed separately from one another to prevent cross-contamination from OsO_4 vapor. After staining with OsO_4, the samples were rinsed three times with 0.1 M cacodylate buffer followed by three rinses with HPLC-grade water to remove salts.

4.2.5 Ethanol Dehydration

Cells were dehydrated with EM-grade ethanol (Ted Pella, CA). Microchips supporting fixed and stained cells were immersed sequentially in the following concentrations of ethanol: 25% for 5 minutes; 50% for 5 minutes; 70% for 5 minutes; 85% for 5 minutes; 95% for 5 minutes (twice); 100% ethanol for 10 minutes (three times).[3]

4.2.6 Critical Point Drying

Samples were critical point dried (EMS 850, Electron Microscopy Sciences, PA).[2] The loading of the microchips into the sample holder and into the chamber of the critical point dryer (CPD) was done under ethanol to prevent air-drying of the samples. The chamber was sealed and cooled to 5 ºC. The ethanol in the chamber was replaced with liquid CO_2 via a series of fluid exchanges. Each fluid exchange consisted of a 1-minute flush of the chamber with liquid CO_2 followed by a five minutes immersion in CO_2 with no flow. The CO_2 fluid level was adjusted so that the sample holder remained submerged at all times. After the removal of the ethanol the chamber was heated to the critical point of CO_2 (31 ºC, 73 atm), and the chamber was depressurized over a period of 45 minutes. The dry samples were stored in a desiccator prior to imaging to prevent the absorption of water from the air.[2]

4.2.7 Carbon Coating

Critical point dried whole mount cell samples were coated with a thin layer of amorphous carbon using a home built electron beam carbon evaporator. The carbon

deposition rate was ~0.2 Å/s. The vacuum level at the onset of evaporation was 10^{-7} torr, which decreased to 10^{-4} torr upon carbon evaporation.

4.2.8 Electron Microscopy

TEM imaging was performed at 80 kV using a TEM (CM12, FEI, OR) equipped with a 2k×2k CCD camera (Advanced Microscopy Techniques (AMT), MA). The electron dose wasmeasured as follows: the diameter of the electron beam illuminating the phosphor screen was determined, and the current (I) collected on the phosphor screen was measured. The electron dose per unit time (D/t) was calculated via the CM12 software using the equation:

$$\mathrm{D/t} = \frac{M^2 2.5 I D_{screen}^2}{e D_{meas}^2 A_{screen}} \qquad (7)$$

where, M is the magnification, 2.5 is a correction factor to account for backscatter electrons, D_{screen} is the diameter of the screen, e is the electron charge, D_{meas} is the measured diameter of illuminated region on the screen, and A_{screen} is the total area of the screen. After determination of the electron dose the specimen was inserted, whereby the diameter of the illuminated area on thephosphor screen was kept constant. The cumulative electron dose in an experiment was then determined from the irradiation time, t.

3D focal series data sets were recorded with a 200 kV aberration-corrected STEM/TEM (2200 FS, JEOL). The corrector was aligned at 17.3 mrad opening semi-angle (α), and then a second round of correction was done at α = 26.5 mrad. Finally, α

was set to 41 mrad. The corresponding probe current was Ip = 83 pA. Each image contained 512×512 pixels, and the pixel dwell time was $\tau = 8$ μsec.

4.2.8.1 Alignment of TEM images

The individual TEM images of a series were arranged in order of increasing electron dose, merged into a single stack, and then aligned to correct for stage drift using the following procedure. Several individual objects that remained visible throughout the image series were used as alignment references. The positions of these objects were tracked for each frame in the series using the ImageJ[141] plugin, MTrackJ.[142] Figure 19 shows an example of the observed drift of a sample containing COS7 cells coated with 10 nm of amorphous carbon.

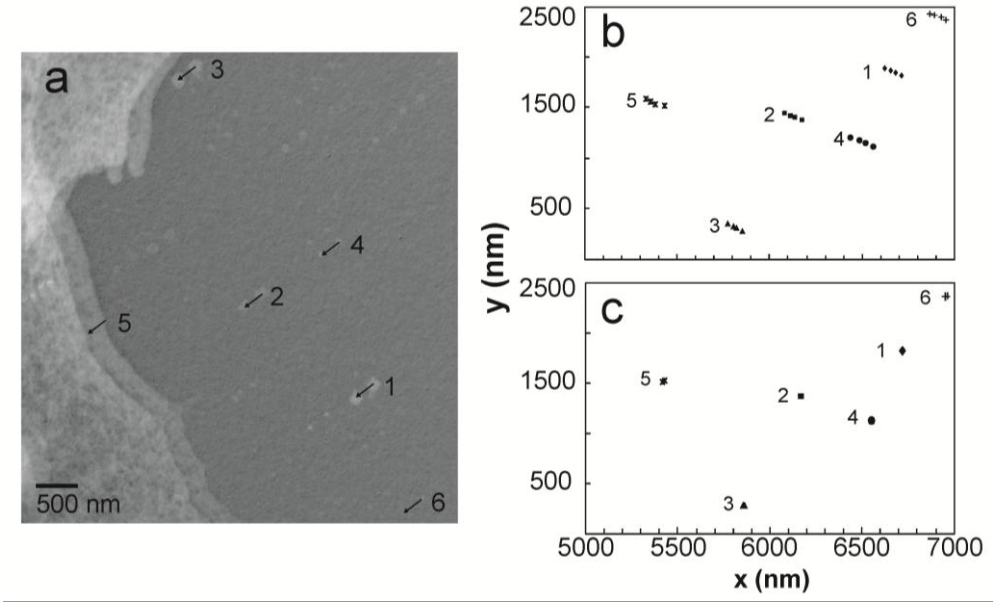

Figure 19: Stage drift over a transmission electron microscopy (TEM) image series. (a) Overlay of two TEM images after irradiation doses of 10^3 e^-/nm^2 and 10^6 e^-/nm^2. Drift vectors are shown as arrows. (b). Coordinates of the reference objects in the TEM image series. The stage drifted approximately 229 nm. (c) Reference object coordinates after image alignment by lateral shifts only.

TEM images taken after electron doses of 10^3 and 10^6 e^-/nm^2 were overlaid; the observed drift vectors are indicated by the arrows (Figure 19a). Stage drift presumably resulted in the translation of the objects between images. The coordinates (x,y) of several objects in Figure 19a were recorded for each frame in the image series (Figure 19b). The objects drifted by an average total of 229 nm. The direction and magnitude of the shift was approximately the same for all reference objects, which confirmed that the shift was a result of stage drift and not sample distortion. The images were then aligned using the average drift vector. The accuracy of the alignment was tested by re-plotting the coordinates of the same objects using the aligned image stack. Figure 19c shows that the reference objects did not exhibit notable shifts after alignment. The above procedure was used instead of cross-correlation,[52] since we wanted to measure the drift of multiple reference objects simultaneously to be able to check for radiation damage.

4.2.9 Stability Analysis Using Linescan Comparison

The following analysis was used to assess the sample stability in successive TEM images. The contrast of each image was inverted in ImageJ so that regions without cellular material had a corresponding signal intensity of 0. Changes to an ultrastructure as a result of electron beam irradiation were measured using linescans, measuring the signal S(x) versus position x, at certain locations in the images. The S(x) values of the linescan in the first image of a series served as the reference ($S_{ref}(x)$) against which the linescans profiles in subsequent images were normalized. The normalized difference in the signal intensity for each position in the linescan profile, $\Delta S_N(x)$, was calculated using equation **7**:

$$\Delta S_N(x) = 1 - \frac{|S_{ref}(x) - S(x)|}{S_{ref}(x)} \qquad (\mathbf{8})$$

The individual values of $\Delta S_N(x)$ were averaged in order to assign a single numerical value for the difference in the profile of the linescan (ΔS_N) as shown in equation **8**:

$$\Delta S_N = \frac{1}{x}\sum_x \Delta S_N(x) \qquad (\mathbf{9})$$

The average stability of the sample or sample region was expressed as the mean ΔS_N of multiple linescans in a region, with the standard deviation providing a measure of the variance within a given sample.

4.2.10 Image processing of STEM images

The 3D STEM data sets were processed using the following image processing steps.[59] The noise in the image was reduced using a convolution filter (Kernel: 1,1,1; 1,5,1; 1,1,1) using the software Digital Micrograph (Gatan). The data was then automatically aligned slice-by-slice using the Autoquant software (Media cybernetics Inc.). The alignment algorithm used was particle alignment with respect to the nearest neighbor, with an alignment setting of 'no warp.' The maximal lateral drift was 70 nm. To increase the axial resolution, the 3D datasets were deconvolved using the Autoquant software [59] via three cycles of deconvolution: (1) 50 iterations of adaptive deconvolution to estimate the object and the point spread function (PSF), (2) 50 iterations with fixed

PSF, and (3) 50 iterations of axial adaptive deconvolution. For the image processing of the datasets presented in the study, the first 100 and the last 100 images were removed from the focal series as these slices contained blurred information only, and removing these images improved processing speed.

4.3 Results and Discussion

Whole mount cell samples were optimized for stability under electron beam irradiation, and their stability under electron beam irradiation was assessed using TEM. The following sample preparation steps were optimized: OsO_4 staining, primary fixation time, and carbon coating. After sample optimization, the stability was determined over an electron dose series of 10^3 to 10^6 e^-/nm^2. Cellular samples, in which EGF receptors were labeled with 10 nm gold nanoparticles, were then imaged using aberration-corrected STEM. The acquired 3D data set was deconvolved and analyzed.

4.3.1 Stability Analysis

We developed a method to measure sample stability via linescan analysis. The method was tested on a sample containing ethanol dehydrated, critical point dried COS7 fibroblast cells grown on EM sample supports. Prior to dehydration the COS7 cells were fixed with glutaraldehyde for 15 minutes, stained with OsO_4 (40 nM), and the saline was removed by rinsing the samples in water. The analysis of sample stability was performed as follows. A reference image was recorded with an initial electron dose of 10^2 e^-/nm^2. After the reference image was recorded, a second image was recorded after a cumulative electron dose of 10^5 e^-/nm^2 at the same position of the sample. We expected the thicker

regions of the cells near the nucleus to be more sensitive to electron beam damage than the thin regions at the edge of the cells. For this reason, thick and thin cellular regions were analyzed independently. Two regions of different thickness within the same sample are shown in Figure 20. The first region, near the edge of the cell (Figure 20, a and b), remained stable during irradiation, as can be seem from the high degree of overlap of the linescans shown Figure 20c. A thick region, near the nucleus envelope, is shown in Figure 20d and Figure 20e.

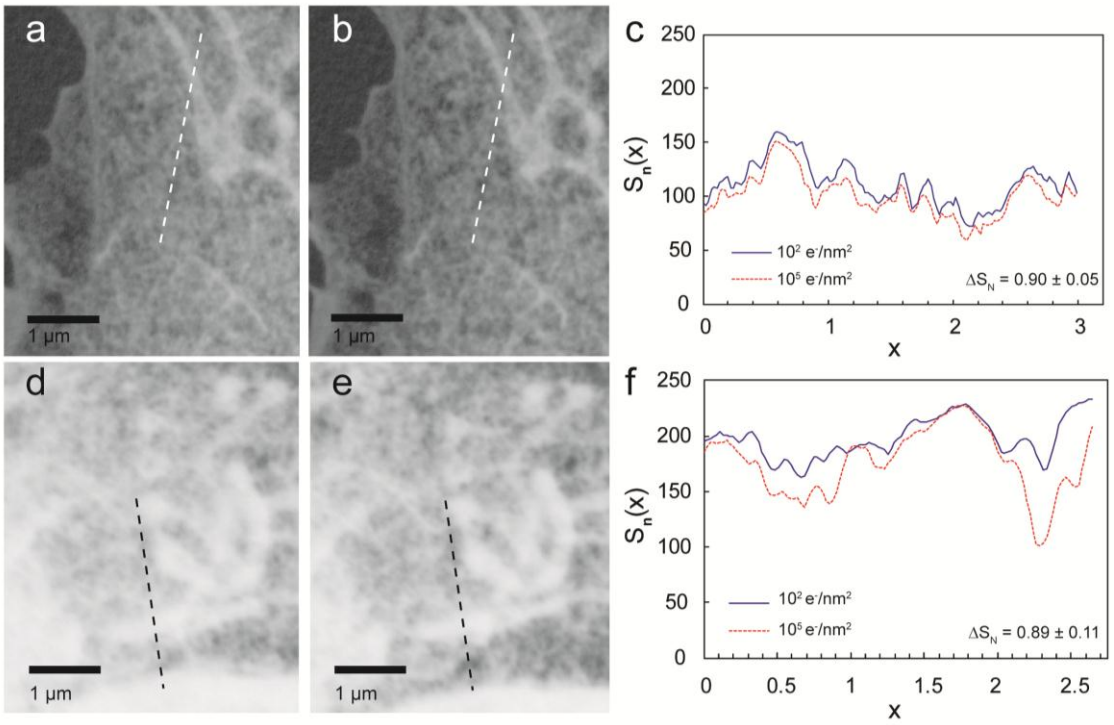

Figure 20: Linescan analysis of TEM images of critically point dried COS7 cells during irradiation series. (a) TEM image of a thin cellular region recorded with an electron dose of 10^2 e^-/nm^2. (b) TEM image of the same region after receiving a cumulative electron dose of 10^5 e^-/nm^2. (c) Signal versus position S(x) of the linescan indicated by the dashed white line shown in images (a) and (b). Both profiles exhibit a high degree of, with only a minimal decrease in signal intensity at the higher electron dose. (d) TEM image of a thick region in the same sample recorded with an electron dose of 10^2 e^-/nm^2. (e) TEM image of the same region shown in (d) after receiving a cumulative electron dose of 10^5 e^-/nm^2. (f) Profile of the linescan indicated by the dashed white line shown in images (d) and (e). The changes in the profile resemble structural changes corresponding to the two regions in the indicated by arrows in the TEM images.

The two linescans across this region show several differences (Figure 20f).

The largest changes in the profile occur at regions indicated by the arrows. The difference in the linescan profiles was quantified as the normalized change with respect to the first image in the series, and averaged for the pixels in a line scan (ΔS_N; see methods section). The ΔS_N values the linescans of Figures 3C and 3f are 0.90 and 0.89, respectively.

The overall sample stability was determined by analyzing several line scans and calculating the mean ΔS_N. For the thin cellular region the mean ΔS_N was 0.83 ± 0.02 (for a total of n = 7 averaged linescans), while the region near the nuclear envelope had a mean ΔS_N 0.80 ± 0.08 (n = 14). In addition to having a lower mean ΔS_N value, the standard deviation of the thick region was fourfold larger than for the thin cellular region, indicating that thick sample regions exhibited a larger variance in stability relative to thin regions. Thus, the stability measure, mean $\Delta S_{N,}$ is sensitive to a stability difference between two regions within a sample.

4.3.1.1 Osmium Tetroxide Staining

Staining with 1% OsO_4 (40 mM) is the standard in TEM sample preparation used to stabilize the lipid content and enhance contrast [3]. We reasoned that the standard concentration of OsO4 could possibly result in too much metal in the thicker regions of a whole cell sample, thus obstructing imaging in those regions. Therefore, staining with an ultra-dilute solution of OsO4 (40 nM) was used. Cells were fixed for 45 minutes in 4% glutaraldehyde in PBS, and then incubated in 40 nM OsO4 in cacodylate buffer for 1 hour. The samples were dehydrated with ethanol, critical point dried, and coated with 10 nm of carbon. For comparison we also tested the standard OsO_4 concentration of 40 mM

(1%), and no OsO_4 at all, see Figure 21. Regions of darker contrast (as indicated by the arrow) were present in the unstained control sample (Figure 21a), but several organelles, such as the mitochondria, were not identifiable. The mitochondria are clearly visible in both the OsO_4-fixed samples (Figure 21b, c). Yet, we did not observe a difference in contrast between the low and high concentrations of OsO_4, and, therefore, we chose the lower (40 nM) concentration for further the experiments described in this study.

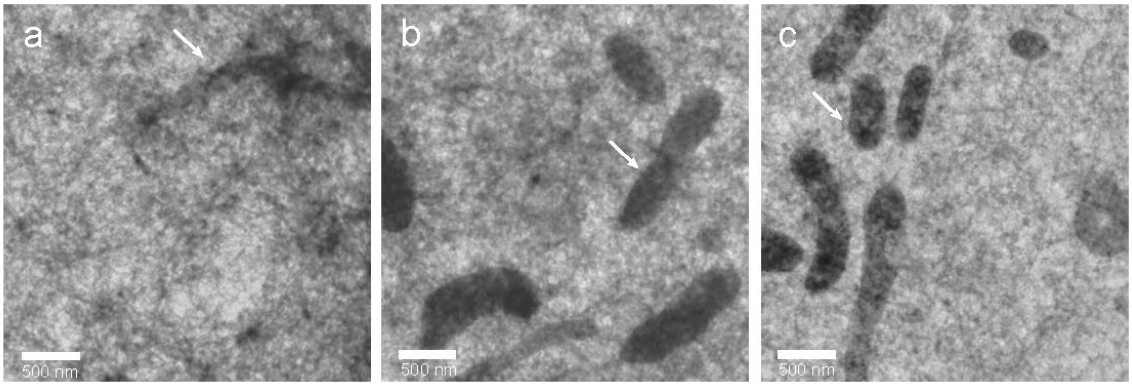

Figure 21: Comparison of OsO_4 staining conditions in TEM images. (a) No OsO_4. (b) 40 nM OsO_4. (c) 40 mM OsO_4. Cellular features in the unstained control (a), such as the mitochondrial envelope, were indistinct in comparison to the samples treated with OsO_4 (b and c). However, a clear advantage in contrast or ultrastructure preservation was not observed between the samples stained with 40 nM (b) or 40 mM of OsO_4 (c).

4.3.1.2 Glutaraldehyde Fixation Time

The length of the primary fixation was varied to determine if the fixation time influenced the sample stability. COS7 cells were fixed at room temperature in 4% glutaraldehyde for 15, 30, 45, or 60 minutes. The fixed cells were stained for one hour with 40 nM OsO_4, rinsed, then dehydrated with ethanol and critical point dried. For each condition 10 linescans were analyzed. The mean ΔS_N values are shown in Figure 22. There was no significant difference amongst the four fixation times examined, and,

therefore, subsequent experiments utilized a standard fixation time of 45 minutes in 4% glutaraldehyde.[2,3]

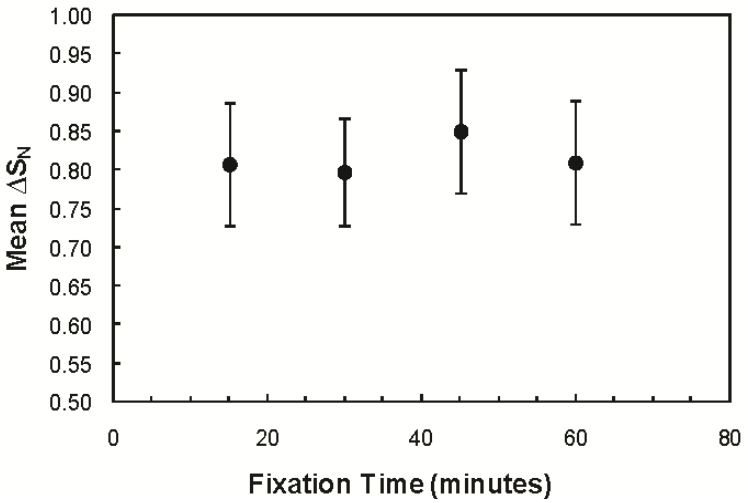

Figure 22: The sample stability measure, mean ΔS_N, as function of the glutaraldehyde fixation time. TEM images were recorded after the samples had received an electron dose of 10^2 e^-/nm^2 and 10^5 e^-/nm^2, and analyzed for stability.

4.3.1.3 Influence of Carbon coating on Stability

Additional samples were prepared to test if coating the samples with a layer of amorphous carbon improved the sample stability. A continuous layer of carbon provides electrical conductance, and mechanical stability. Samples were fixed for 45 minutes with 4% glutaraldehyde in PBS followed by OsO_4 staining for 1 hour (40 nM). Following ethanol dehydration and critical point drying, the samples were coated with 10, 20, or 50 nm of amorphous carbon, and then imaged using TEM (Figure 23). In an area near the cell grains of deposited material are visible on the SiN window surface, for the samples coated with either a 20, or a 50 nm layer of carbon. The average sizes of these grains were 6 ± 1 nm, and 20 ± 2 nm, for the 20 and 50 nm layers, respectively. For the sample coated with 10 nm of carbon the deposited material did not exhibit distinguishable grains.

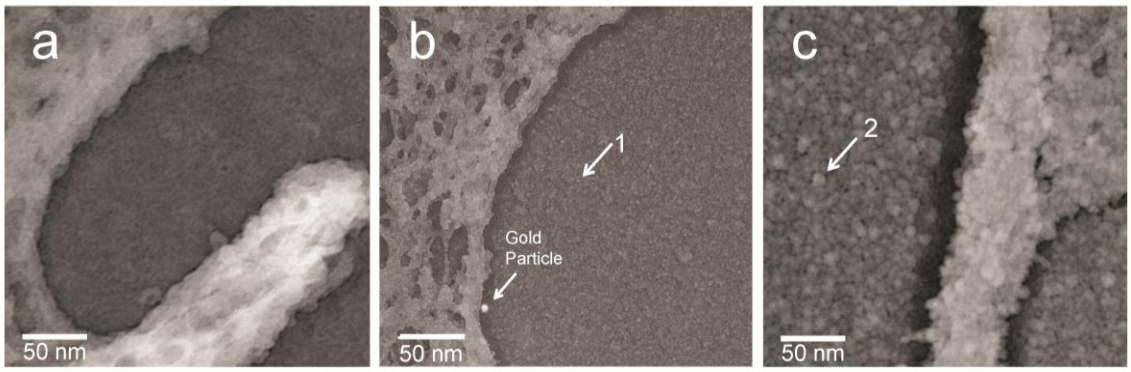

Figure 23: TEM images of carbon coated critical point dried cells. (a) 10 nm carbon coating. (b) 20 nm carbon coating. (c) 50 nm carbon coating. Grain-like particles indicated by the arrows measured were observed for both the 20, and the 50 nm layer, but were not visible for 10 nm of carbon.

The carbon-coated samples were analyzed for stability, and compared with an uncoated control sample. For each sample, a TEM reference image was recorded using an electron dose was 10^2 e^-/nm^2. The same region was then recorded after a receiving a cumulative electron dose of 10^6 e^-/nm^2. Linescans throughout both thin and thick cellular regions were analyzed to measure the difference in stability between the coated and uncoated samples. Figure 24 compares the stability of samples with, and without, a coating of amorphous carbon. TEM images of the uncoated control sample (Figure 24a) shows a loss of cellular material near the region indicated by the arrow in after irradiation (Figure 24b).

However, TEM images of samples coated with a 10 nm layer of amorphous carbon (before: Figure 24c, after: Figure 24d) show no visible structural change upon electron beam irradiation. A comparison of the mean ΔS_N values for both thick and thin regions samples coated with different carbon thicknesses is shown in Figure 24e. The control sample (no carbon) was the least stable, with a mean ΔS_N of 0.85 ± 0.02, while each of the carbon coated samples had a mean ΔS_N of 0.93 ± 0.02 or above. Thus, the

application of the carbon coating significantly improved the stability, but only a small difference was found between the tested coating thicknesses.

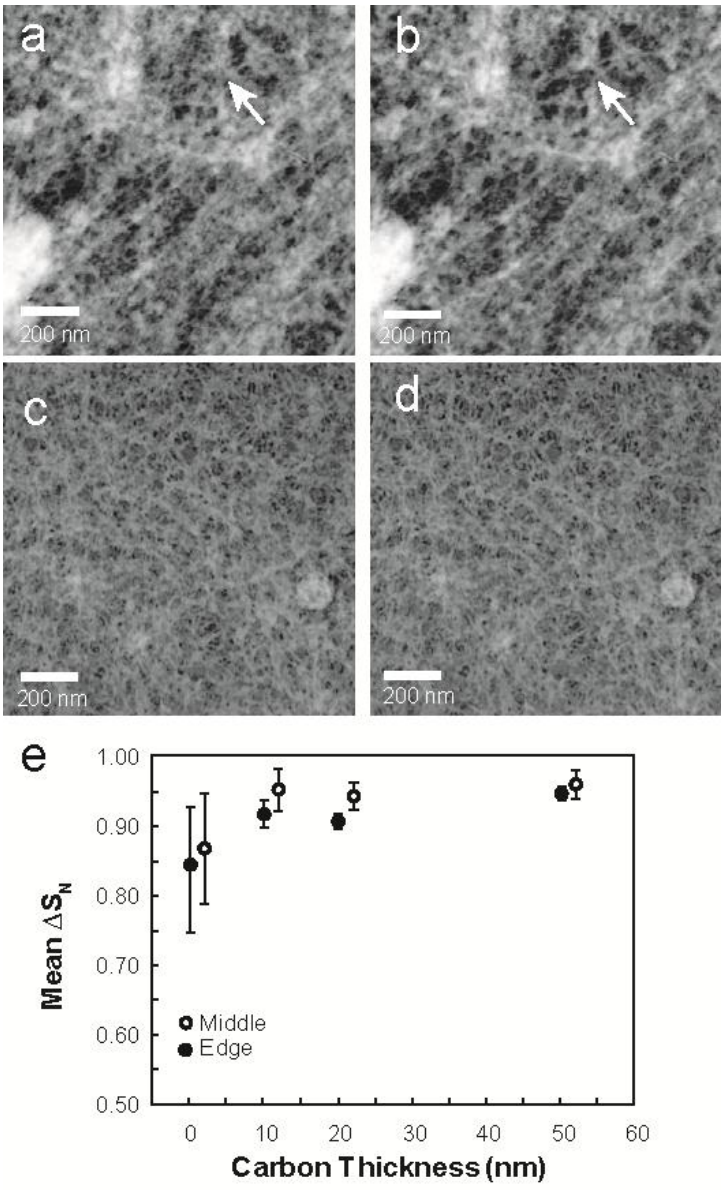

Figure 24: Evaluation of the sample stability obtained with carbon coating. (a) TEM image of a control (no carbon), recorded with an electron dose was 10^2 e^-/nm^2. (b) TEM image of the same region of the control sample after cumulative irradiation of 10^6 e^-/nm^2. The arrows indicate a region that underwent distortion. (c) TEM image a sample coated with 10 nm of carbon and recorded with and electron dose of 10^2 e^-/nm^2. (d) TEM image of the same region of the carbon coated sample after irradiation with a dose of 10^6 e^-/nm^2, demonstrating the high degree of structural preservation. (e) Stability measure, mean ΔS_N, of samples coated with different thicknesses of carbon. The stability was tested for two different cellular regions.

4.3.1.4 Stability Range: Electron Dose

In order to determine the dose resistance of the optimized samples coated with 10 nm carbon to high electron doses, we tested the following series of electron doses: 10^3, 10^4, 10^5, and 10^6 e^-/nm^2. The mean ΔS_N for both thick and thin cellular regions at each electron dose are shown in Figure 25.

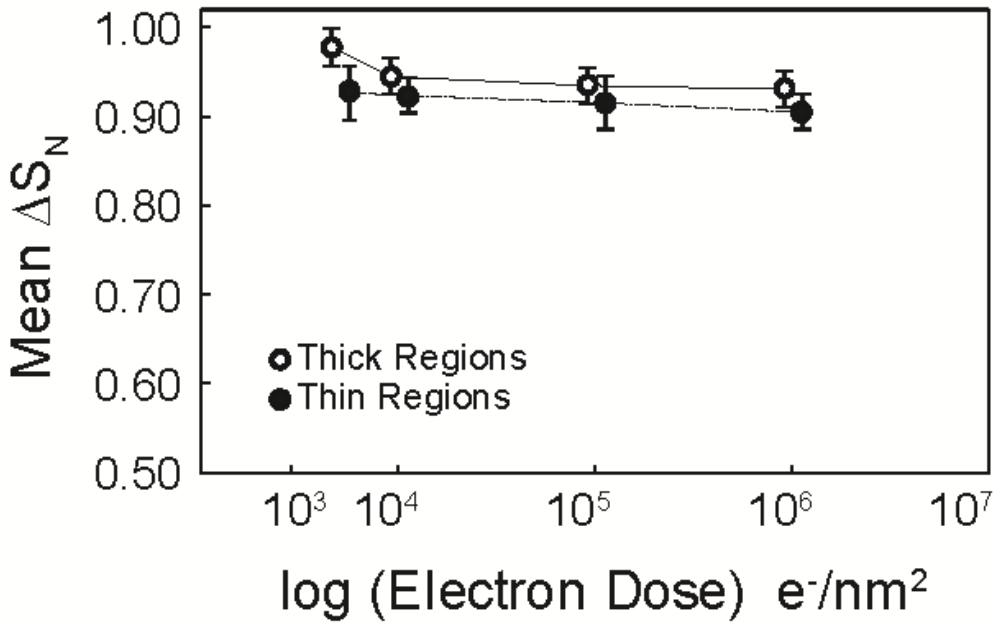

Figure 25: The sample stability, measured with ΔS_N, as function of the electron dose, separated by cellular region.

Thick regions remained stable for each dose in the series with values of mean ΔS_N remaining at 0.93 or higher, with a standard deviation of less than ± 3% for all data points. Thin and thick sample regions were of the same stability within the standard deviation. From these results we conclude that the samples should withstand the electron dose needed for the recording of a focal-series dataset with STEM with a dose of up to 10^6 e^-/nm^2.

4.3.2 3D STEM Imaging of Nanoparticles on Whole Cells

Samples of whole mount COS7 cells were prepared with gold-tagged EGF receptors localized at the cell surface. The cells were fixed, stained, critical point dried, and coated with 10 nm of amorphous carbon. 3D focal series were recorded over several cellular regions at a magnification of 100,000 and a probe semi angle of 41 mrad, with an aberration corrected STEM. The sample was first pre-irradiated with an electron dose of 1×10^5 e^-/nm^2 to reduce contamination and sample shrinkage during imaging. The first dataset was collected at the edge of the cell. It contained N = 500 images, acquired with focus steps of dz = 2.5 nm, and a pixel size of s = 2.8 nm (magnification of 100k). The image series was acquired such that sufficient focal positions above and below the specimen were obtained to allow deconvolution.[16] The total imaging time was 30 minutes. Since the divergence of the electron beam over the entire vertical range of the focal series was much smaller than the image size, the average electron dose during the focal series acquisition can be approximated by:

$$D = \frac{I_P \tau N}{e s^2} \qquad \textbf{(10)}$$

with electron charge e. It followed that D = 2.6×105 e-/nm2 for the settings used in this experiment. The cumulative dose the sample was irradiated with at this location was thus 3.6×10^5 e^-/nm^2.

Before and after the recording of a focal -series dataset we also took an image with the cell mostly in focus, to test for possible radiation damage. We analyzed the stability of the sample by comparing these two STEM images. Figure 26 shows selected

areas of 256 x 270 pixel of STEM images recorded before (Figure 26a) and after (Figure 26b) the focal series acquisition. From these images it can be seen that the ultrastructure was mostly preserved after the 3D imaging. The only visible change was a shift along the fold-like feature highlighted by the dotted line at arrow #1. Also the positions of gold nanoparticles were conserved, as shown, for example, at the arrow #2. Linescans were taken along the dashed lines in Figure 26a and b, and their profiles compared in Figure 26c. The linescan analysis demonstrates a good structural stability as indicated by the overlap of the two profiles. The nanoparticle at arrow #2 is also visible in the linescans. The region with less stability clearly shows at arrow #1. Since the less stable region at arrow #1 was surrounded by overlapping regions in the linescan, we suggest that the sample distortion was a movement of a cellular structure, possibly a membrane protrusion. Further analysis of the images via linescans resulted in a mean ΔS_N value of 0.90 ± 0.03 ($n = 21$) in most section of the images Figure 26a and b, except for the region along the dashed line, where the mean ΔS_N was 0.82 ± 0.09 ($n=11$). The specimen thus remained mostly stable during the recording of a focal series with STEM.

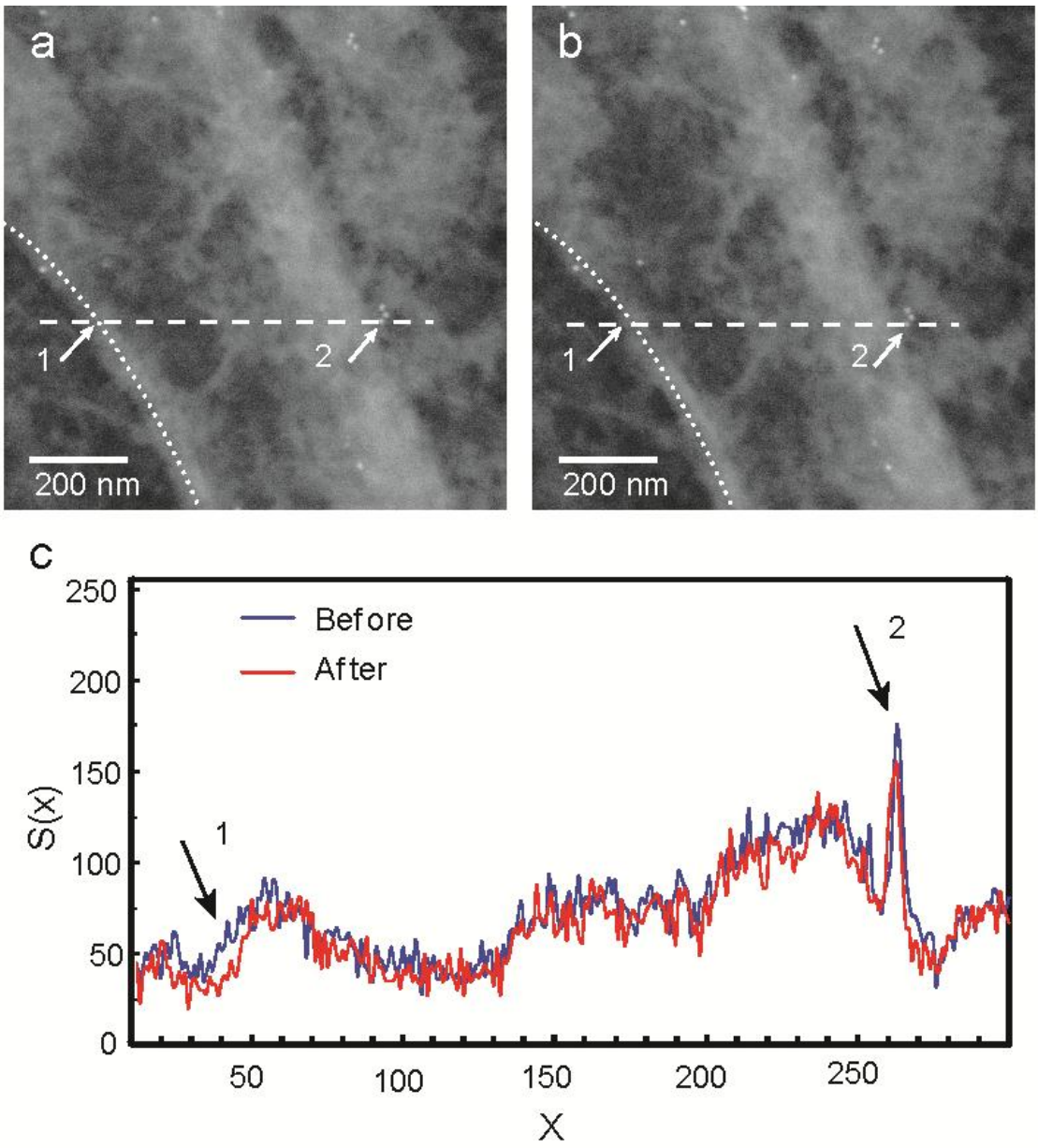

Figure 26: Sample stability during the recording of a STEM focal series of COS7 cells. (a) STEM image recorded prior to the acquisition of the focal series. The celluar structure is visible in grey. The round spots indicate gold nanoparticles. (b) Same region as shown in (a), images after the recording of the focal series. The cumulative electron dose was $3.6 \cdot 10^5$ e^-/nm^2. (c) Intensity profiles of the linescan shown as dashed line in (a) and (b). The arrows indicate the regions in the STEM images indicated by #1 and #2. The dotted line in (a) indicates a structural feature that underwent a shift as observed in the profile in (c) at arrow #1.

Selected frames from the focal series are shown in Figure 27. Initially, the nanoparticles appear blurred and out-of-focus. However, as the image series progresses,

individual particles begin to come into focus, with the most particles in focus at an axial position between 272.5 nm and 422.5 nm.

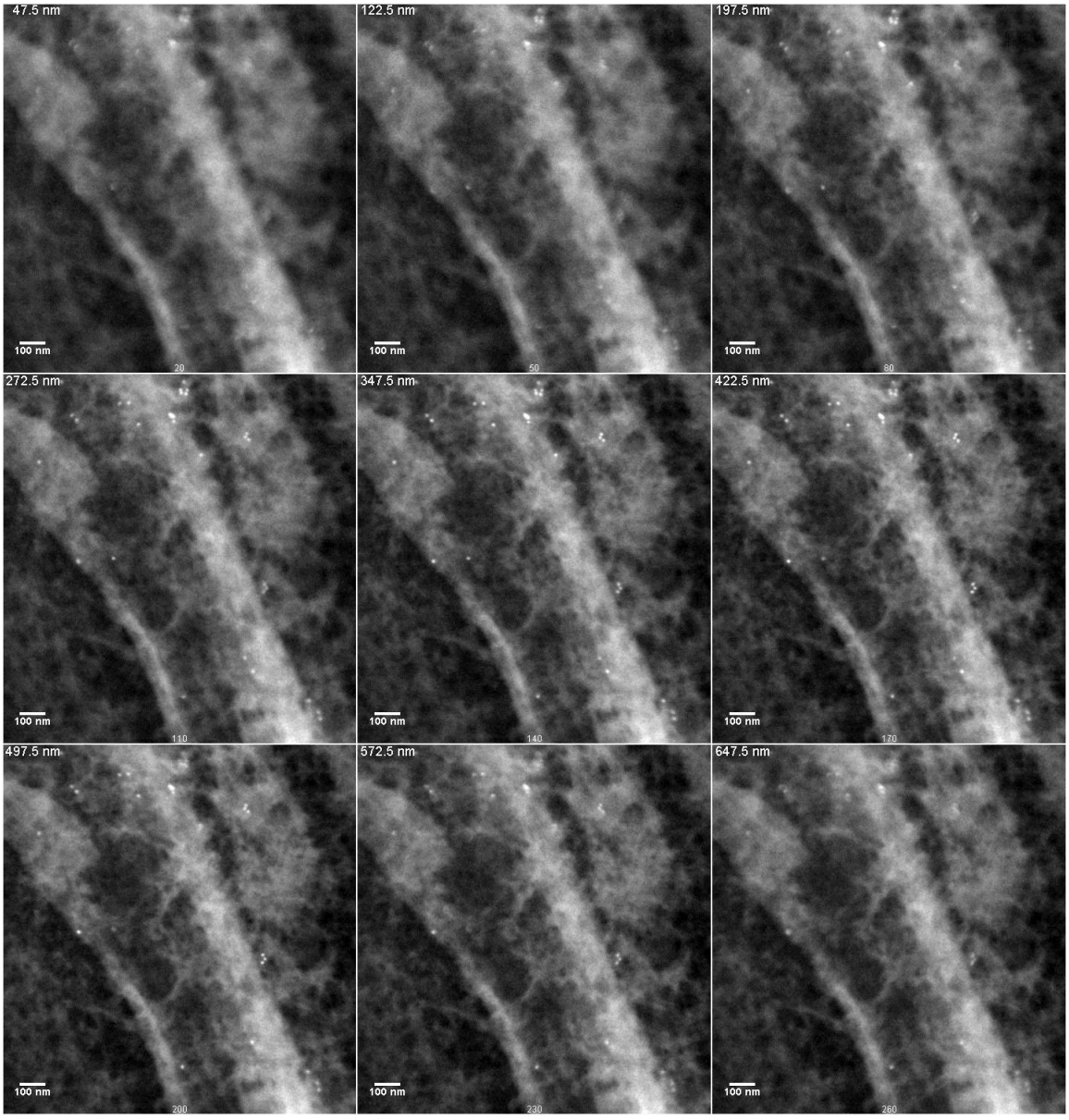

Figure 27: Selected frames of STEM focal series. The gold nanoparticles, visible as bright white dots, begi coming into focus in frames 272.5 to 422.5, after which they begin to move out-of-focus. The cell structure visible as grayish white material.

Figure 28a shows an image obtained from a projection of the focal series at the same coordinates as Figure 26. The focal series was projected in axial direction on the lateral plane as the sum of the individual slices to obtain the image (using ImageJ). This dataset was recorded in a cellular region close to the edge of a cell, where several filaments are visible. A total of 26 gold nanoparticles can be distinguished as bright spots. These are homogenously dispersed, as expected for the short period of incubation.[123] Because 3D STEM is a wide field imaging methodology each image contains also out-of-focus information of the adjacent slices, and the axial resolution is limited. To optimize the axial information in the 3D data set we have applied adaptive deconvolution [59]. To enhance the processing speed the first 100 and the last 100 images were removed from the focal series as these slices contained only out-of-focus information, beyond that which was necessary for deconvolution. Figure 28b depicts a projection on the lateral plane of the deconvolved data at the same position as Figure 28a. The labels are visible with more contrast. Some of the information of the ultrastructure was lost while the deconvolution functions optimal for objects with a strong contrast.

The increase in axial resolution due to deconvolution was evaluated with axial linescans over nanoparticles, as exemplified in Figure 28c for nanoparticles #1 and #3 (indicated in Figure 28b). The average full width half maximum (FWHM) of the axial intensity peaks (signal intensity versus axial position) of 10 nanoparticles was 340 ± 75 nm. The deconvolution procedure reduced the noise and increased the axial resolution, as shown in Figure 28d. After deconvolution, the average FWHM over the intensity peaks in the axial linescans of 10 nanoparticles was 99 ± 28 nm. The precision at which

a position of a single nanoparticle can be determined is much higher than the resolution, as long as the nanoparticles are well separated.

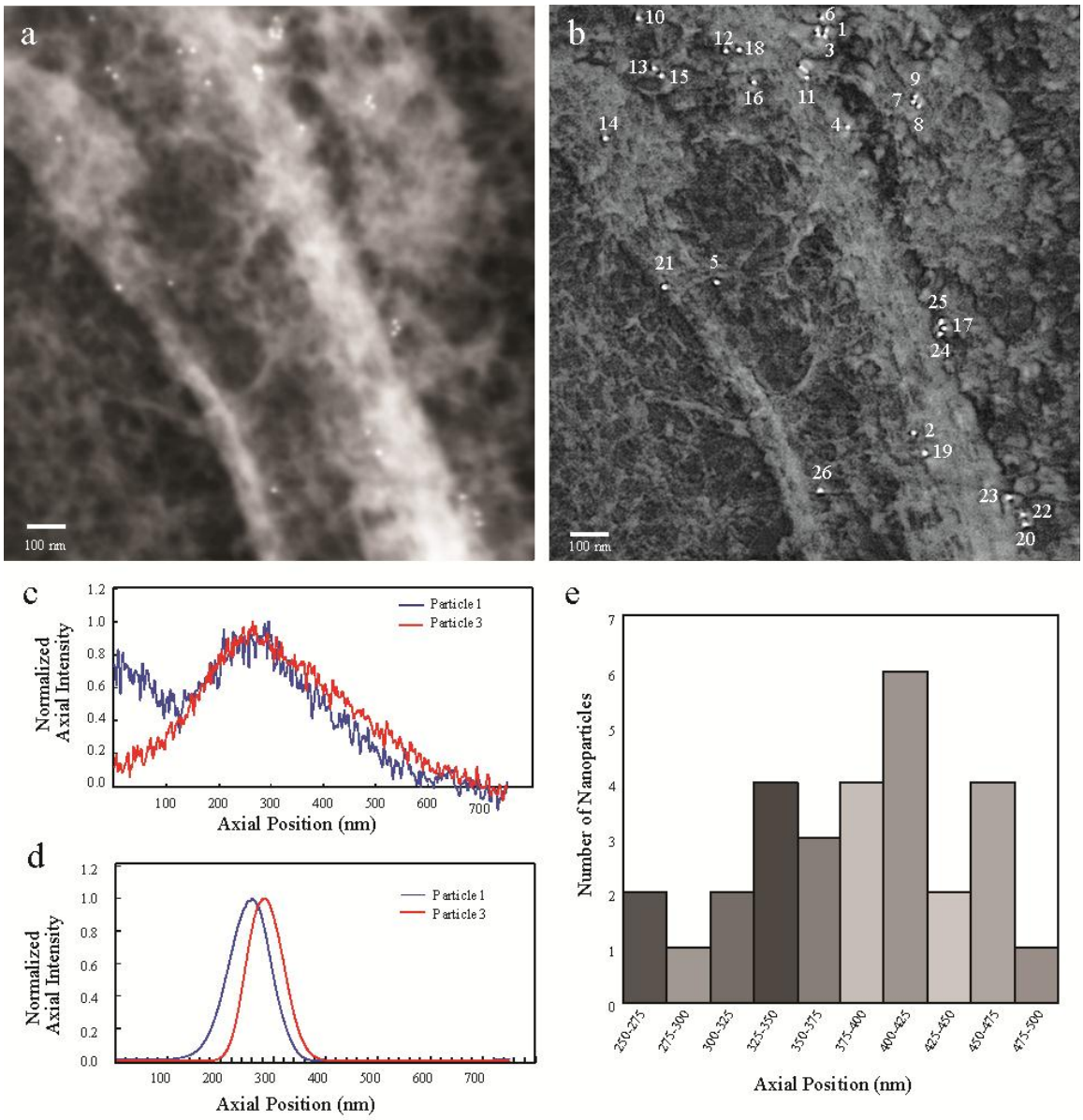

Figure 28: STEM focal series of COS7 cells. The epidermal growth factor (EGF) receptor at the cellular surface with labeled with gold nanoparticles conjugated to EGF. (a) Projection of the images of the focal series on the lateral plane, showing both the ultrastructure and the nanoparticles. (b) The dataset was deconvolved to increase the axial resolution obtained on the nanoparticles. The image resembles the projection of the focal series on the lateral plane. (c) Axial profiles (intensity versus vertical position) over adjacent nanoparticles (#1 and #3) before deconvolution. (d) The plot profiles of the same linescan after deconvolution. (e) Histogram of the vertical locations of the gold nanoparticles with axial increments of 25 nm. The axial region that contained the largest number of gold nanoparticles was between 400 nm and 425 nm. Image contrast and brightness was adjusted to increase visibility of the gold nanoparticles.

The increase in the axial resolution after deconvolution can be observed in Figure 29. The out-of-focus signal is reduced, and the largest number of in-focus nanoparticles is contained within the frame corresponding to 422.5 nm.

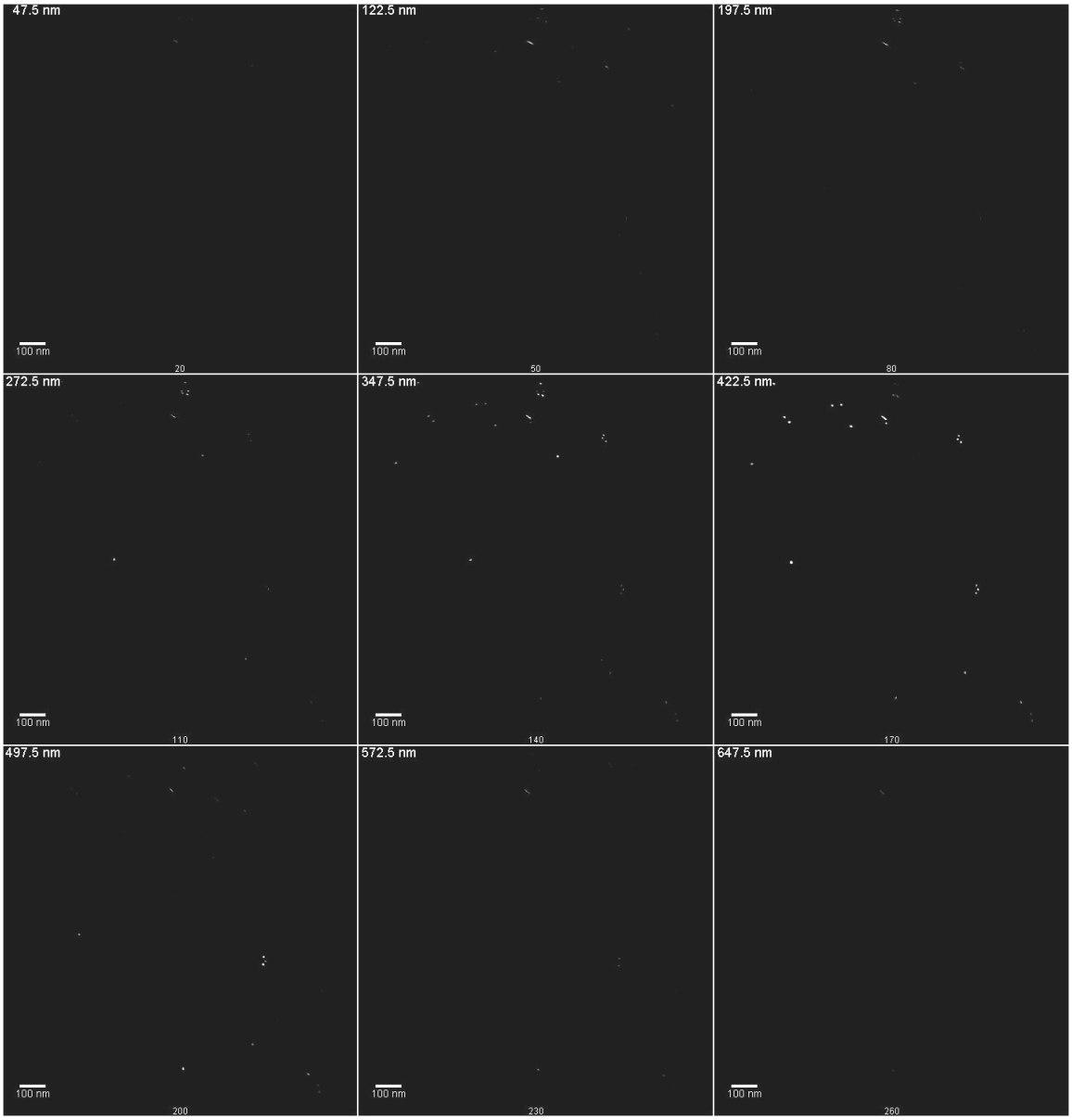

Figure 29: The same image frames, as shown in Figure 27, after deconvolution. The image contrast and bri have been adjusted to highlight the positions of the gold nanoparticles. The majority of the particles are in f frame 170. The deconvolved images contain less noise than the non-deconvolved images.

The axial positions of the 26 gold nanoparticles were determined from the maximum in the axial intensity profile, see Table 3.

Table 3: Axial Locations of Gold Nanoparticles

Particle	Axial Position (nm)	Particle	Axial Position (nm)	Particle	Axial Position (nm)
1	260 ± 2.5	11	385 ± 2.5	21	442.5 ± 2.5
2	265 ± 2.5	12	392.5 ± 2.5	22	450 ± 2.5
3	282.5 ± 2.5	13	395 ± 2.5	23	467.5 ± 2.5
4	312.5 ± 2.5	14	400 ± 2.5	24	467.5 ± 2.5
5	317.5 ± 2.5	15	405 ± 2.5	25	470 ± 2.5
6	330 ± 2.5	16	407.5 ± 2.5	26	482.5 ± 2.5
7	337.5 ± 2.5	17	415 ± 2.5		
8	350 ± 2.5	18	415 ± 2.5		
9	352.5 ± 2.5	19	422.5 ± 2.5		
10	357.5 ± 2.5	20	425 ± 2.5		

The precision was estimated to be ± 2.5 nm, which corresponded to the focal step size. The two labels, #1 and #3, shown in Figure 10d, were located at vertical positions of 260 nm and 282 nm, respectively. The positions of the gold nanoparticles range from 260 ± 2.5 nm (label #1) to 482.5 ± 2.5 nm (label #26). A histogram of the distribution of the axial locations (Figure 10e) shows that the largest number of nanoparticles is located at a depth of 400 - 425 nm. The cells face towards the point of beam entry, and a smaller axial value resembles a vertical position closer to the surface of the SiN membrane. Thus the smaller the axial position the farther the nanoparticle is relative to the SiN support. Thus we can conclude that the topography of the cell surface is inhomogeneous.

A 3D dataset was also recorded at a thicker cellular region, near the nuclear envelope is shown in Figure 30. This dataset was recorded with the following

microscope settings, N = 400 images, dz = 5 nm, and s = 4.6 nm (magnification of 100k). The total dose after pre-irradiation was 1.8×10^5 e^-/nm^2. All images were used in the doconvolution. The mean delta S_N was 0.91± 0.03 (n =25), indicating that also this cellular region was stable during the recording of the focal series. Prior to deconvolution (a), the gold nanoparticles are not visible within the increased signal from the cellular material compared to imaging at the edge of the cell (Figure 28). After deconvolution the nanoparticles were visible (Figure 30b).

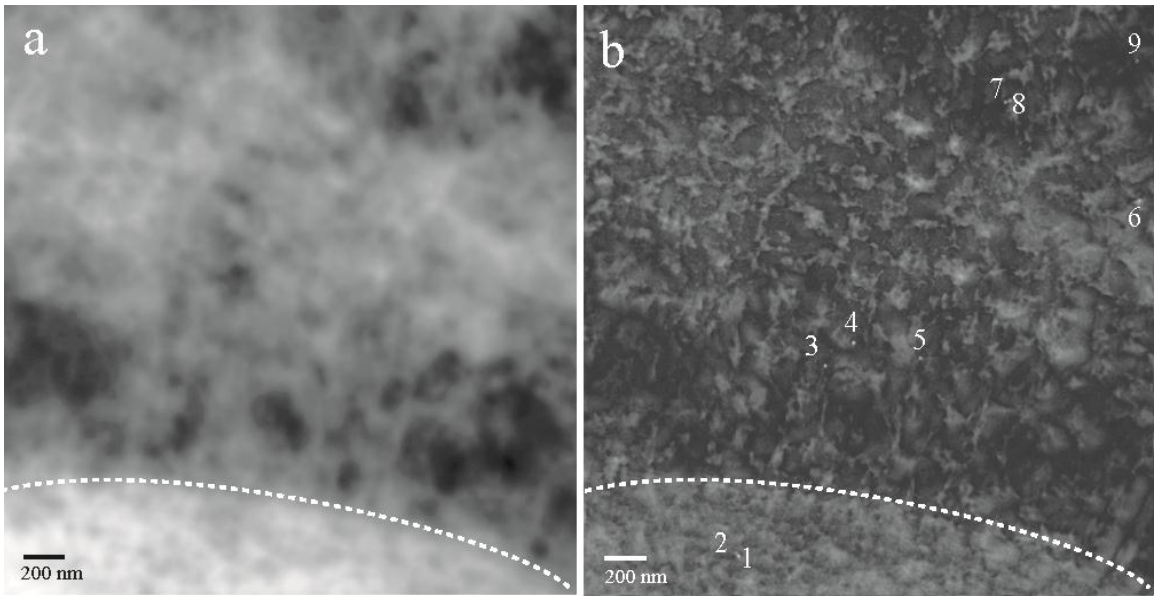

Figure 30: STEM focal series of a COS7 cell recorded in a thick cellular region at the edge of the nuclear e (indicated by dashed line). (a) Projection of the focal series on the lateral plane. (b) Projection of the decon dataset. A total of 9 gold nanoparticles is visible.

A total of 9 gold labels was observed, and their axial positions are shown in Table 4. Nanoparticles # 2 and #6 were separated by an axial distance of 730 nm. Thus the cellular surface curved from the region near the nucleus towards the nuclear region causing its surface to rise by 730 nm. The thickness of the cell thus must have been thicker than 730 nm. Obtaining 3D information with nanometer precision from cellular

specimens of this thickness is very difficult with conventional TEM tomography, even with energy filtering.[6]

Table 4: Axial Locations of Gold Nanoparticles at the Nuclear Envelope

Particle	Axial Position (nm)
1	1230 ± 5
2	1335 ± 5
3	760 ± 5
4	800 ± 5
5	645 ± 5
6	605 ± 5
7	650 ± 5
8	665 ± 5
9	790 ± 5

We have successfully applied 3D STEM the imaging of whole-mount cellular samples, and detected the vertical locations of the labels with high precision (3 nm). In our sample we found the labels to be mainly at the cellular surface, but several labels were probably located just below the surface, or within membrane regions of high curvature. It is important to notice that the STEM detected electrons transmitted through the entire sample. It does not matter for the STEM if the labels are located at the surface, or within the cell, as long as the labels are not so deep in the sample that beam blurring prevents their imaging, which does not happen until at least depth of 2 μm depending on the density of the specimen.[39]

An example of a STEM focal series of a control sample which was not coated with amorphous carbon is shown in Figure 31. Although the control was imaged with an

electron dose of 1×10^5 e^-/nm^2, more than threefold lower than the dose used to image the carbon coated samples, the cellular material was unstable during imaging. The white arrows in Figure 31 highlight the regions where damage was sustained during the focal series.

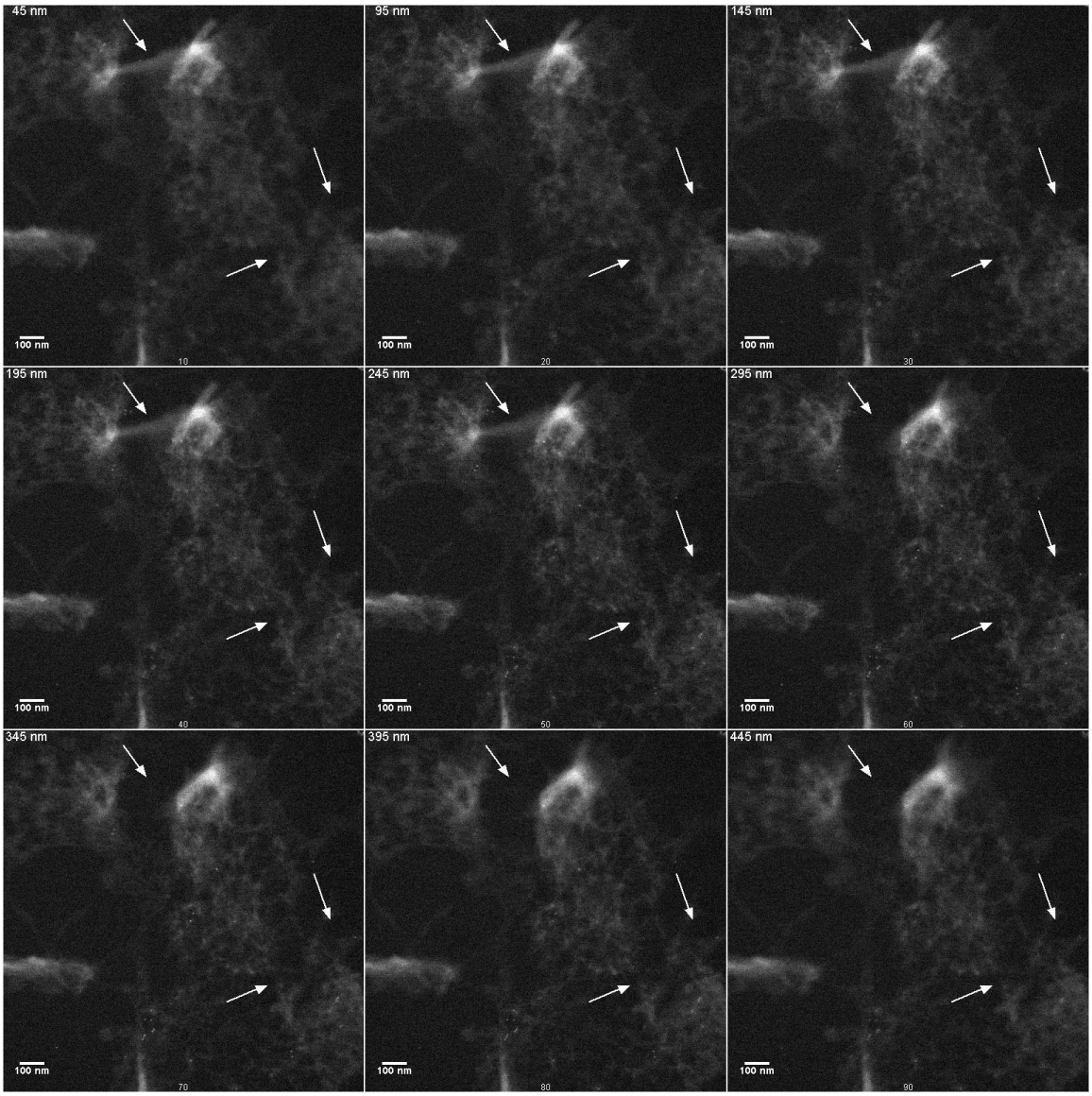

Figure 31: Selected frames of a control sample which was not coated with carbon. The arrows indicate regi which the cellular material undergoes damage as the focal series progresses. The total electron dose was of focal series was 1×10^5 e^-/nm^2.

4.3.3 Axial Distribution of Labels

An important question is what the cause of the variation in the axial positions of the gold nanoparticle labels; was this caused by (1) passive diffusion through the membrane (2) internalization of the EGF receptor or (3) vertical inhomogeneity of the cellular surface? Diffusion of the nanoparticles through the membrane of cells is unlikely to occur in glutaraldehyde fixed cells without first permeabilizing them with a detergent, such as saponin or tritonX.[49] Also, endocytosis of the EGF labeled gold nanoparticles is unlikely to occur during the five-minute incubation at room temperature.[63,123,143] Thus the difference in axial position of the nanoparticles in Figure 28 is presumably due to the topography of the cellular membrane. Because EGF is internalized via endocytosis of clathrin coated pits,[144] one possibility is that some of the nanoparticles are localized within clathrin enriched buds, or invaginations within the cellular surface that occur during the first step of vesicle formation. Although internalization of the EGF ligand-receptor complex occurs within minutes of binding at 37ºC, the process of endocytosis is much slower at room temperature.[145,146] Furthermore, clusters of gold nanoparticles, which form prior to vesicle formation, are absent, which suggests that the difference in axial height is not due to pit formation.[124,144,146,147]

A second possibility is that the difference in axial height is due to ruffling of the cellular membrane.[148] Ruffling is the formations of transient, fold-like protrusions of the membrane, particularly near the edge of the cell. Stimulation of COS7 cells, as well as other cell lines, with EGF is well known to induce ruffling of the cellular membrane 1-2 minutes after binding of EGF.[149-151] The cellular ultrastructure observed in Figure 9 is similar to the long fold-like structure of membrane ruffles observed by others using

SEM.[148,150,152] Two pairs of adjacent nanoparticles are located on such fold, for example, the structures: #5 and # 21, and #2 and #19. Interestingly, the individual nanoparticles that comprise each pair are separated by an axial distance greater than 100, despite their lateral proximity. The difference in axial position of these nanoparticle pairs is likely due to the slope of the membrane ruffle on which they are bound. Thus, we conclude that the difference in axial heights among the gold nanoparticles is a result of the surface topography of the membrane, specifically membrane ruffles, rather than internalization of the receptor ligand complex.

The presence of membrane ruffling may also account for the localized instability of the sample described in Figure 28. Because the ruffle structure protrudes out, away from the cellular surface, it is capable of being deflected by the electron beam. Thus the shift in the linescan observed in Figure 28c may have resulted from a change in position, such as folding, of the membrane ruffle structure, while the main cellular body was stable.

In Figure 30, two nanoparticles located on the nucleus, # 1 and #2, have an axial position relative to the remaining nanoparticles of 730 nm at most. This vertical difference can be explained by the vertical protrusion of the nuclear envelope. The vertical positions of nanoparticles near the nuclear envelope differ by a maximum of 185 nm, which indicates a high degree of membrane surface roughness near and bending of the membrane towards the nucleus.

4.5 Conclusions

A procedure was developed for stabilizing whole mount eukaryotic cell samples grown on SiN windows for imaging with STEM. The key step was the coating of the critical point dried cells with amorphous carbon. The stability of the samples was measured quantitatively by analyzing linescans obtained from TEM images. The samples remained stable during the acquisition of a 3D focal series using aberration-corrected STEM with an electron dose of 3.6×10^5 e^-/nm^2. The 3D datasets highlighted different cellular regions containing gold nanoparticles tagging the EGF receptor. The gold nanoparticles were resolved on the surface of the whole cell at a range of vertical positions, and an axial precision of ± 2.5 nm was achieved after deconvolution. From analysis of the variation of the axial positions of the labels we concluded that the cellular surface was ruffled.

CHAPTER V

CONCLUSIONS AND FUTURE DIRECTIONS

Imaging techniques which are capable of imaging individual proteins in their physiological environments are key to the development of our understanding cellular structure and function. Conventional electron microscopy (EM), however it is limited to by sample thickness (< 500 nm). Thus thin sections (< 100 nm) are typically prepared from cells embedded in resin or ice, which can result in extensive changes to the native structure.[2,44] In addition to sample preparation, labeling intracellular features using conventional immunogold labels, requires either-sectioning of the cell prior to labeling, or permeabolization of the membrane. Thus, designing targeted molecular probes which can be internalized without disrupting the cell's structure is desirable. One such strategy would be to utilize flexible polymeric nanoparticles that are interspersed with high-Z metal ions. Due to their biomimetic qualities, these structures, such as dendrimers, have been shown to have enhanced membrane penetrability in comparison to metal nanoparticles,.[91,104,153-156] Thus, they can be delivered into a living cells.

Combining multiple imaging modalities in a single probe significantly increases the overall performance of the molecular probe.[75] Thus, combining both fluorescent and electron dense moieties into a single biologically targeted nanoparticle would allow both real-time imaging, via light microscopy (LM), and high resolution via EM. Chapter I introduced the use of lanthanide metal ions as both luminophore and EM contrast agents. Due to the low extinction coefficient of europium, it was necessary to sensitize the ion by

attaching an organic chromophore to the chelate scaffold. Several coumarin sensitized europium chelates were synthesized and their fluorescence was characterized. One such complex (III) 2,2',2"-(10-(coumarin-3-carbonyl)-1,4,7,10-tetraazacyclododecane-1,4,7-triyl) triacetate exhibited a molar extinction at 8400 $M^{-1}cm^{-1}$, increased by 240% relative to our previously published quinoline methyl antenna.[101] Additionally, it was found that two antennas, 7 – methoxy - (4-bromomethyl) - coumarin and 4-bromomethyl acridine, showed potential as a two-photon active antennae for near infrared (NIR) excitation. Thus, when complexed with a NIR emitting lanthanide ion such as ytterbium or neodymium, we expect these compounds will both excite and emit in the NIR, allowing better penetration and signal for in vivo applications labeling. As a proof of concept, the synthesis and characterization of a membrane permeable, metal-loaded dendrimer nanoparticle was presented. This particle, a TSPO targeted, bimodal dendrimer containing an organic fluorophore for optical signal and gadolinium ions for EM contrast was shown to be internalized by cells expressing the receptor of interest. Enhanced EM contrast was shown in cells labeled with this compound, both with, and without OsO_4 staining, relative to the contrast of controls. Such lanthanide containing dendrimers-could be utilized to label live cells for whole cell imaging with EM. Furthermore, the affinity of OsO_4 for PAMAM dendrimers suggests that biologically targeted PAMAM dendrimers themselves could be utilized as site specific contrast enhancement agents for OsO_4 stained samples.

Scanning transmission electron microscopy (STEM) enables electron dense (high-Z) structures, such as nanoparticles, to be imaged within several micrometers of low-Z material, such as a whole cell, or a layer of liquid. Chapter III demonstrates correlative

light and electron microscopy imaging of quantum dots on a whole cells using wide field fluorescence microscopy followed by STEM. Additionally, the cell was maintained in a native (liquid) environment during imaging by enclosing it within a vacuum isolated, microfluidic chamber. STEM images of individual QDs on whole eukaryotic cells were correlated with the fluorescent images of the same sample. Correlative liquid STEM requires no additional sample processing beyond that which is needed for fluorescent imaging. Thus, it has two key advantages over state-of-the-art correlative LM and TEM, requiring thin sections, or thin frozen samples: (1) Artifacts introduced by dehydration, post-staining, freezing, or sectioning are avoided. (2) Because additional sample processing between imaging modalities is not required, fluorescence microscopy can be used to monitor tagged proteins in living cells to determine the desired time point of the fixation. Although liquid STEM has so far been limited to either surface proteins or proteins that internalize via endocytosis,[63] strategies for introducing nanoparticles into live cells, such as membrane penetrating peptides,[135] or metal loaded dendrimers (such as those discussed in Chapter II), may be used to label intracellular proteins in the future. The spatial resolution of 3 nm demonstrated with liquid STEM is sufficient to discriminate nanoparticles differing in size, shape, and electron density for multi-label experiments to study the constituents of protein complexes within cells.

The next objective was to extract three dimensional (3D) data from whole cells using EM, which is desirable for elucidating the arrangement of protein assemblies. The 3D distributions of tagged proteins on whole cells were obtained utilizing STEM as shown in Chapter IV. Whole COS7 fibroblast cells were imaged and remained stable during the acquisition of a 3D focal series using an aberration-corrected STEM which

resulted in an axial precision of ± 3 nm deconvolution. From analysis of the variation of the axial positions of the labels features of the cellular surface, such as membrane ruffling were identified, highlighting the potential of this technique to identify structural features in addition to localizing positions of individual proteins.

Table 5 summarizes the imaging requirements that are met by both liquid STEM and 3D focal series STEM.

Table 5: Summary of Attained Imaging Requirements

Requirements Met	**Liquid STEM**	**3D Focal Series**
Native State Conditions	✓	✓*
3D	✓*	✓
Resolve Protein Position	✓	✓
Whole Assemblies	✓	✓
Time Resolved		
Intracellular	✓	✓
Reproducible	✓	✓
Speed	✓	✓

* Indicates feasible, but not demonstrated

Although seven of the eight requirements are obtained with either technique, dynamic processes cannot be observed in real time using STEM because the electron beam initiates rapid cell death.[157] However, this limitation is mediated when combining whole cell STEM with light microscopy for correlative imaging. Dynamic cellular processes can be observed initially with light microscopy, following which high resolution "snapshots" can be recorded at the same position using liquid or 3D focal series STEM.

The development of high-Z, membrane permeable labels, such as the lanthanide chelate imaging agents discussed in Chapter II, is expected to further increase the utility these EM techniques. Additionally, the observed affinity of OsO_4 for PAMAM dendrimers offers a second labeling strategy that omits the need to chelate high-Z ions. Such an approach could utilize biologically targeted PAMAM dendrimers to provide site-specific contrast enhancement in specific regions after OsO_4 staining. Because changes in the cellular quantities of many proteins act as identifying markers for a number of disease states, such as cancer [158,159]and Alzheimer's disease[108], accurate quantification of the concentration and spatial distributions of these markers is important in both diagnostic and therapeutic monitoring. For instance, the TSPO targeted PAMAM dendrimer, discussed in Section II of Chapter II, could be employed to enhance the visibility of the mitochondria for both liquid and 3D focal series STEM. The contrast of the mitochondria would be preferentially enhanced after osmium staining, thus enabling changes in TSPO expression to be more easily identified.

The results presented in this dissertation demonstrate that utilizing STEM enables whole cells to be imaged under both dry and wet conditions; thus minimizing structural and environmental disruption of the native state of cellular proteins.

APPENDIX A

WHOLE-CELL ANALYSIS OF THE EFFECT OF CHOLESTEROL ON LOW DENSITY LIPOPROTEIN - GOLD NANOPARTICLE UPTAKE IN MACROPHAGES BY STEM TOMOGRAPHY AND 3D STEM: PRELIMINARY RESULTS

This appendix is adapted from the abstract submitted to the *2011 Microscopy and Microanalysis Meeting* entitled "Whole-Cell Analysis of the Effect of Cholesterol on LDL-Gold Nanoparticles Uptake in Macrophages by STEM Tomography" by J.P. Baudoin, M.J. Dukes, W.G. Jerome, and N. de Jonge.

A.1 Introduction

Macrophage cholesterol accumulation is considered a critical process in the development of atherosclerotic plaques, the cause of most heart attacks and strokes. Low density lipoprotein (LDL), the main carrier of blood cholesterol, enters blood vessels where monocyte-derived macrophages take it up, converting macrophages into so-called foam cells.[160] Most of the studies about cholesterol accumulation by macrophages use LDL-gold nanoparticle uptake to monitor the amount of LDL taken up by the cells. Semi-thin sections provide an elegant way to look by conventional transmission electron microscopy (TEM) at the localization of LDL-gold nanoparticles along the endocytic pathway and to quantify them.[161] But such quantifications are time consuming and an accurate quantification of LDL-gold uptake at the whole cell level is still missing. Tilt-series TEM is the traditional methodology to resolve unique parts of the three dimensional (3D) cellular ultra-structure.[115] A cubic volume is reconstructed from projections obtained by mechanically tilting the sample stage. The resolution of the reconstruction is in the range of 1–20 nm.[114] A new development in 3D electron

microscopy (EM) is the use of scanning transmission electron microscopy (STEM), which can detect high atomic number elements inside an embedding medium of a low atomic number.[58-60,137]

In this study we are utilizing an approach combining the advantages of tilt-series STEM and focal-series STEM to image gold-nanoparticles within the 3D context of whole cells. We applied this new methodology to quantify the effect of cholesterol on LDL-gold nanoparticles uptake by macrophages.

A.3 Preliminary Results

The LDL-gold was prepared and purified following standard literature procedures.[162,163]. The final product was negative stained with and imaged with TEM to verify adsorption of the lipoprotein to the surface of the gold nanoparticle (Figure 32).

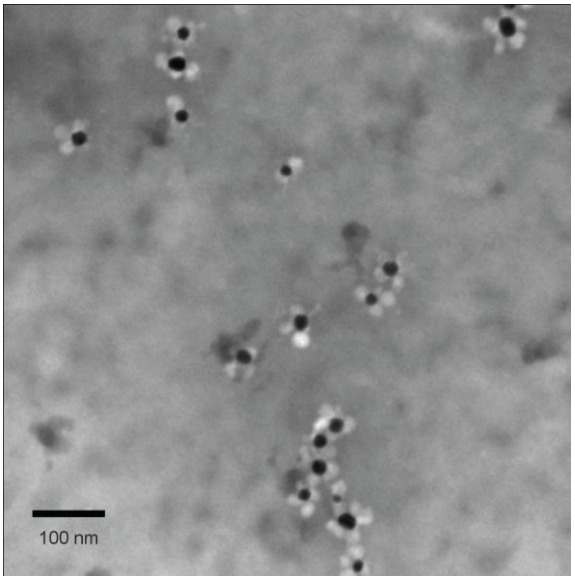

Figure 32: TEM image of negative stained LDL-gold

THP1 monocytes differentiated as macrophages were grown for 6 days directly on silicon microchips supporting thin silicon nitride (SiN) windows and then loaded with 10 nm LDL-gold for 1 day (5 µM).[164] After two rinses with PBS, cells were fixed with a mixture of Glutaraldehyde 2,5% in cacodaylate 0,1M/$CaCl_2$0,005% buffer for 1 hour, post-fixed with OsO4 1% for 1 hour, ethanol dehydrated, air dried and finally coated with 50nm of carbon. The obtained data describes the localization and quantification of gold-nanoparticles inside whole-cells with a nanometer resolution.

The samples were first inspected by TEM at 120 KeV (CM12, FEI) to characterize at the whole-cell level the nanoparticles internalization pattern (Figure 33)..

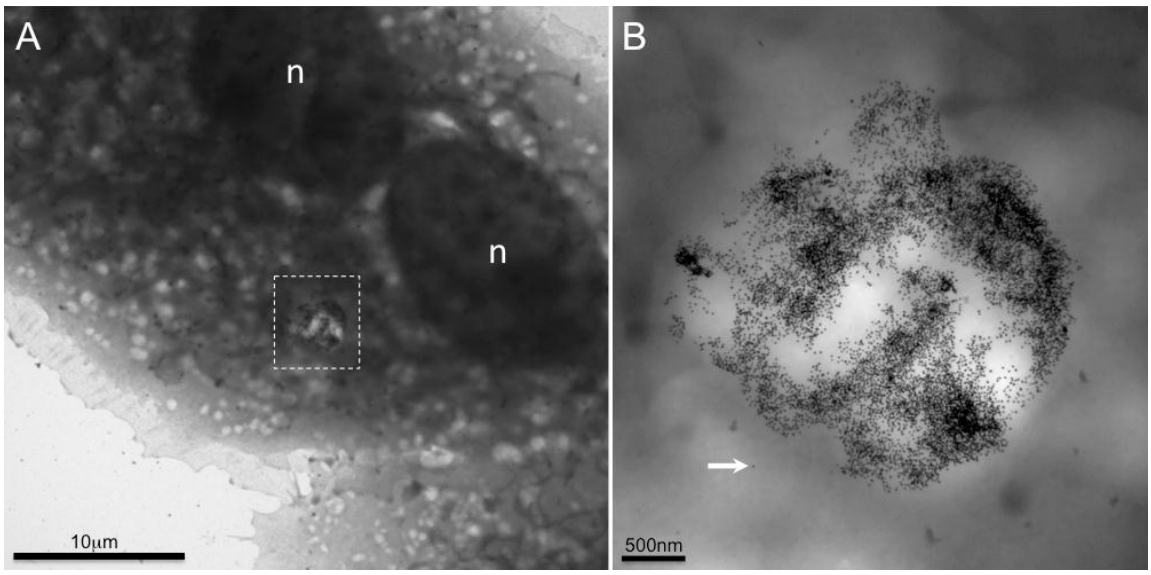

Figure 33: TEM images of low density lipoprotein (LDL)-gold nanoparticles contained in macrophage cell lysosomes. (a). TEM view of a whole macrophage containing low density lipoprotein (LDL)-gold nanoparticle (n = nucleus). (b) Close up of the the area indicated by the dashed box from (a) depicting nanoparticles (arrow), likely localized within in a vesicle.

To obtain 3D information while optimizing for reduced damage we recorded a tilt-series with minimal acquisitions/angle range using a 200 KeV STEM (CM200, FEI)

(Figure 34a). The tilt-series reconstruction was processed with the Etomo/3Dmod software, (Figure 34b).[165]

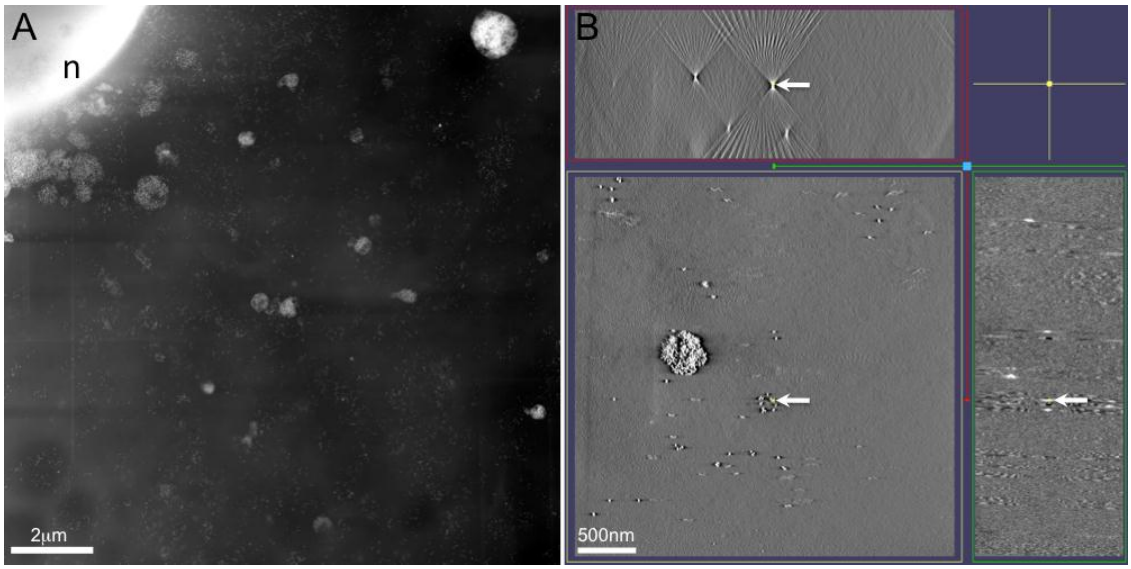

Figure 34: Scanning transmission electron microscopy (STEM) images of low density lipoprotein (LDL)-gold contained in macrophage vesicles. (a) STEM view of low density lipoprotein (LDL)-gold nanoparticles in the peri-nuclear region of a macrophage. (b). XYZ view of a 3D tomogram depicting single gold-nanoparticles (arrow). n = nucleus.

A.4 Preliminary Conclusions and Future Directions

As a second 3D approach focal series using aberration corrected STEM was also recorded using 200 KeV (JEOL 2200 FS). These results are currently undergoing deconvolution, after which they will be compared with the results obtained with tilt-series STEM. We expect that combining the results obtained by both 3D approaches will provide an improved methodology for whole cell analysis by electron microscopy.

APPENDIX B

SILICON NITRIDE WINDOWS SAMPLE SUPPORTS FOR ELECTRON MICROSCOPY OF CELLS

This appendix is adapted from "Silicon Nitride Windows for Electron Microscopy of Cells" by Elisabeth A. Ring, Diana B. Peckys, Madeline J. Dukes, Jean-Pierre Baudoin, and Niels de Jonge, it is currently in press by *The Journal of Microscopy*.

B.1 Introduction

Transmission electron microscopy (TEM) has traditionally been used to study the ultrastructure of cells via the preparation of conventional thin sections, where a cellular sample is fixed, stained, embedded in plastic resin, and sliced.[2] Cells can also be prepared into amorphous ice via high-pressure freezing and cryo-sectioning,[54,115] although the involved protocols are rather complex. For many questions in cell biology it is useful to study samples containing whole cells with both light microscopy (LM) and TEM, which can be accomplished by growing cells directly on 3 mm support grids with carbon or formvar thin films.[53] However, these thin films are typically difficult to handle with cell culture procedures. In recent years, semiconductor-manufacturing processes have resulted in a new type of support film for TEM: thin silicon nitride (SiN) membranes.[166,167] These films are highly homogeneous in thickness, extremely robust, and are biocompatible, meaning that cells can be cultured directly on them. In addition, SiN windows can be used as separation windows for vacuum chambers, such that cells in liquid can be studied with electron microscopy (EM).[63,168] The use of microchips as support for cellular samples[169] is especially beneficial for correlative LM and EM,

wherein lower-resolution images are obtained via LM, and EM is used to "zoom in" on a section of interest with nanometer resolution.[170]

Here, we describe the design and fabrication of the microchips, and details of how to prepare biological samples to be imaged on them, including specific labeling with nanoparticles, and drying procedures for use with TEM. We provide examples of images of whole eukaryotic cells, obtained using LM, TEM, scanning TEM (STEM), and liquid STEM. In all examples, the cells were prepared directly on the microchips. We also discuss correlative approaches. This paper serves as a detailed guide for those interested in using silicon microchips with SiN windows as support for cellular samples.

B.2 Microchips

B.2.1 Design and testing

The microchips (manufactured by Protochips Inc, NC) were made of silicon with dimensions of 2.00 mm in height, 2.60 mm in length, and 0.30 mm in thickness, with a SiN window in the middle,[171] see Figure 35.

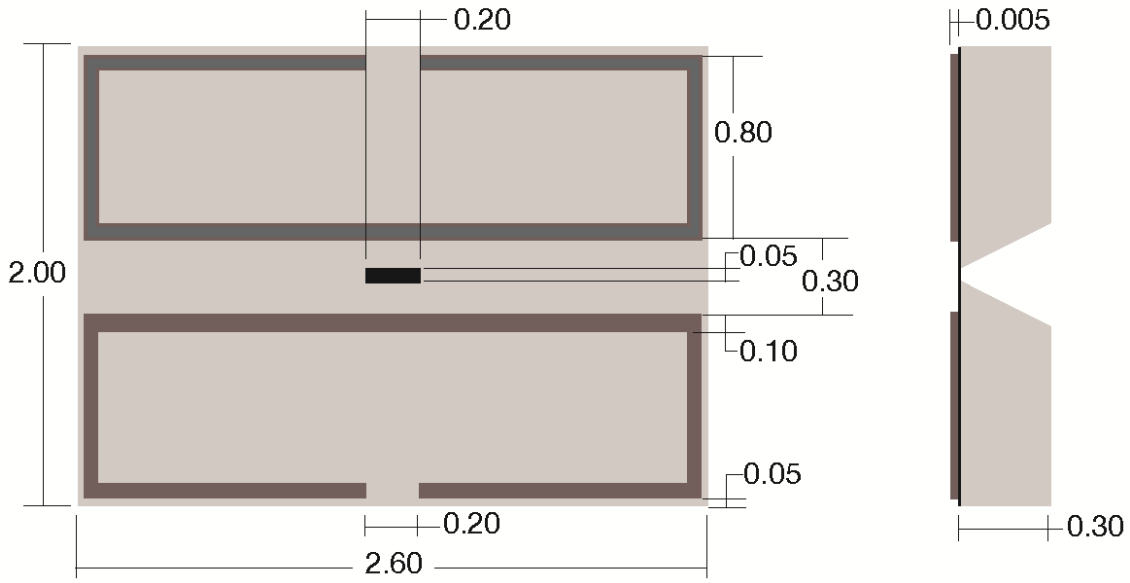

Figure 35: The design of the spacer microchip. Both the top view and the side-view cross-section are shown. All dimensions are in mm. The microchip had a width of 2.00 mm, a length of 2.60 mm, and a thickness of 0.30 mm. The tolerances were ±10 μm. The black area in the middle indicates the 50 nm thick silicon nitride (SiN) window. A patterned spacer is shown in dark grey, providing a flow channel over the SiN window.

SiN is a commonly used material in micro electro mechanical systems (MEMS) fabrication. To determine the optimum SiN window thickness, we deposited gold nanoparticles on the top and bottom of a 50 nm thick test window and imaged the window at high magnification in an aberration corrected 200 kV STEM (JEOL 2200 FS) in a previous study.[62] Gold fringes with a spacing of 0.2 nm were visible for particles both at the bottom and at the top, thus we concluded that the 50 nm thick window had a negligible effect on the electron beam. A 100 nm-thick test window was also imaged, but the image of the gold layer at the bottom of the window appeared blurred. This is attributed to elastic scattering of the electron beam in the SiN material. With TEM, the resolution would be slightly decreased due to inelastic scattering. Using standard equations,[64] it was calculated that the resolution in TEM would be limited to maximal 0.5 nm for 50 nm-thick SiN, which is more than sufficient for many biological applications.

However, when higher resolution is required, for example, for single particle tomography, then thinner SiN windows, or carbon windows should be considered.

Several sizes of the SiN window were tested. Windows spanning several hundreds of micrometers allow a large field, but are prone to rupture during cell culture processing steps. The rigidity of the windows is of particular importance for liquid EM, where two windows are placed in the vacuum of the electron microscope, and enclose a liquid at atmospheric pressure. The windows have to withstand this pressure difference, and each window should not bulge by more than ~1 μm for liquid STEM imaging, as the bulging could render the sample too thick to image. Furthermore, if the thickness throughout the sample varied due to bulging, then the image contrast would vary correspondingly, preventing high-resolution imaging. To optimize window strength and field of view, we tested rectangular windows, since the degree of bulging is mainly determined by the short dimension.[171] Two windows with dimensions of 50×200 μm^2 and 50 nm thickness were used to enclose a liquid at atmospheric pressure in the vacuum of the electron microscope. The windows were found to bulge by about a micrometer each, which was deemed acceptable. However, windows with dimensions of 70×200 μm^2 were found to bulge by about 2 μm each, which was considered too large to allow for high resolution imaging.[171]

The dimensions were chosen such that at least one entire eukaryotic cell could be viewed within the window. It is not uncommon for typical surface adhering eukaryotic cells to spread out to a length of 50 μm.[172] Thus we aimed for a window with a width that was no smaller than 50 μm. The length of 200 μm facilitated the imaging of multiple cells, which is desirable for biological experiments. Because the width of the window is

the limiting dimension in terms of resistance to bulging and breaking, the length can be altered to fit the user's needs. Additionally, for experiments that involve smaller objects, the width can be made smaller.

For use in liquid EM, two microchips have to be positioned on top of each other. In this application it is crucial to ensure that the windows of both microchips are aligned as closely as possible, in order to maintain a sufficiently large field of view for the transmitted electron beam. A precise overlap of the windows was obtained by 1) manufacturing microchips with precisely diced side edges, 2) defining the SiN windows in the center of each microchip, and 3) aligning the microchips in a slot in the specimen holder at their sides. All dimensions of the microchips were manufactured within ±10 µm precision. An additional benefit was that the precision-made vertical sides of the microchips allowed for a much easier handling, compared to commercially available microchips. Certain commercially available microchips have tapered sides, which seem to be difficult to secure with tweezers without damaging the sample at the top surface. If a small field of view is acceptable, then a different solution to the alignment problem is to use one of the standard chips, and one chip where the window is oriented perpendicular to that of the standard model. We have successfully used windows with widths as small as 20 µm. Because these windows bulge less than 1 µm each, they can be used for TEM imaging of liquid specimens, which requires thinner samples and has stricter maximum bulging restrictions for the windows than liquid STEM.

B.2.1.1 Design of spacer layer

To prevent compression of the sample when the microchips are assembled into the microfluidic device, a spacer is needed between the microchips. Two different types

of spacers were used. Microspheres were placed between the microchips, with the advantage being that the gap between the microchips was customizable by choosing microspheres of the desired size.[63] The microspheres were positioned at the four corners of one microchip (not at the window, otherwise rupture is likely to occur), which created a fluid path from the input tubing, through the microchips and surrounding area of the holder, and out through the output tubing. This method accommodated fluid flow, but did not allow for control of the fluid path.

In order to precisely control the rate at which fluid injected into the system reaches the sample, we created a system with a defined fluid path [173]. This consisted of a microchip with a patterned spacer layer (Figure 35) paired with a flat base microchip, providing a straight liquid flow channel with a width of 300 µm over the long side of the microchip. The spacer wall width was 100 µm and its thickness was 6 µm.

Cells were typically grown on base microchips, which have no spacer and provide a flat surface over the whole microchip, allowing the cells to spread and cover the most of this surface. During assembly of the microfluidic chamber the spacer microchip was pressed, with the spacer layer facing down, onto the base microchip containing cells inside the slot in the specimen holder. We patterned a void into the spacer to provide an area for excess cellular material. The wall around the void included an opening at the side where excess cellular material could flow out. Furthermore, the spacer did not extend to the end of the microchips, because in that case, the dicing process (see below) led to detachment of the spacer. The specific design of the spacer layer can be varied by changing the photolithography mask, and the thickness can also be changed, if desired.

B.2.1.2 Fabrication

The microchip fabrication procedure was based on standard methods,[174] the main difference being the highly specified side tolerances, both for the smoothness of the sides, and also for the location of the window with respect to the sides. A schematic of the fabrication of the microchips is shown in Figure 36a for the base microchip, while Figure 36b describes the spacer microchip. A 300 µm thick, double side polished, n-type Si(100) wafer was cleaned using the two step, standard cleaning procedure used in the semiconductor industry, which removes all organic and metal particles, and strips the microchips of their native oxide layer (Step i).[174] A low-stress SiN layer was then deposited on both sides of the wafer via low-pressure chemical vapor deposition at 810ºC (Step ii). The thickness of the SiN layer was confirmed using ellipsometry. A layer of resist was applied, and the window was then defined by photolithography using a mask made of soda lime glass (Step iii). The SiN layer was isotropically dry-etched (Step iv), which resulted in a second mask, allowing for an anisotropic KOH etch of the silicon (Step v). This defined the "front" and "back" sides of the microchips – the front side containing the SiN window.

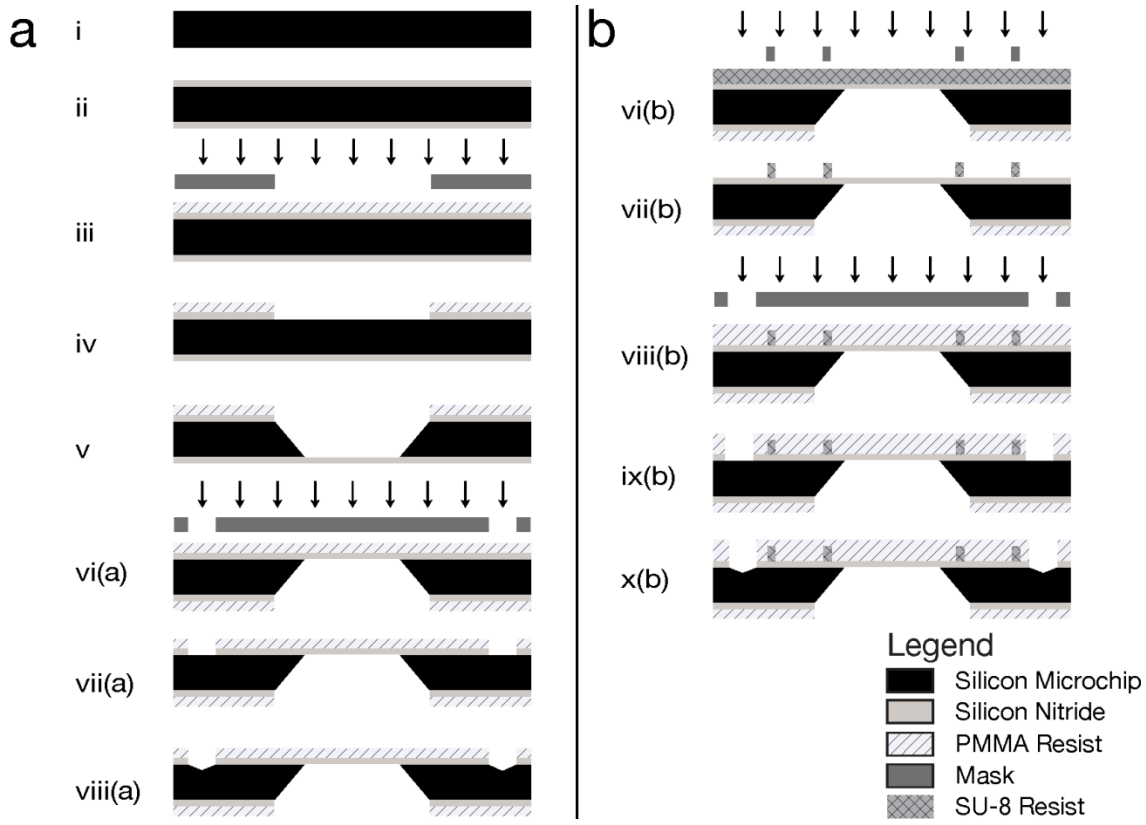

Figure 36: Schematic of the workflow of the fabrication of (a) the base microchips and (b) the spacer microchips. The arrows indicate lithographic exposure. Drawings not to scale.

The edges of the microchips were defined with a tolerance of ±10 µm with respect to the window position. Grooves were etched in the silicon for guidance of the saw-blade. The location of the grooves was patterned into the SiN on the front side of the wafer using CHF_3 reactive ion beam etching (Step vii(a)). The silicon was then anisotropically etched to create the groove (Step viii(a)). Before the final step, a resist coating was applied to protect the microchips from damage and from collecting debris. Then, the microchips were placed with the backside down onto double-sided adhesive tape, and were separated by dicing along the grooves with a precision saw.

For the microchips with the spacer layer, the front side of the microchip was coated in a layer of SU-8 photoresist, and the spacer pattern was defined by

photolithography (Step vi(b)). The grooves were then established using the same methods as for the base microchips (Steps vii(b)-x(b)), and the microchips were coated with a protective resist layer, and then diced using the same method as the base microchips.

B.2.1.3 Cleaning

To allow for high resolution imaging, the SiN window surfaces must be free of any contamination, such as dust particles or material fragments. Both types of contamination are easily collected during manufacturing (especially during dicing), and also during exposure outside of a clean room environment. To keep the microchips clean until they were ready to be used, a resist coating was applied on the SiN during the fabrication process. Once the microchips were ready to be used, the coating was removed by washing for 2 minutes in acetone followed by a 2 minute wash in ethanol, taking care that the acetone did not dry during the transfer of the microchips between the two liquids. About 150 mL of each fluid was sufficient to clean up to 12 microchips at a time, and HPLC grade liquids were always used. Figure 37a shows a window covered in the resist coating and debris from manufacturing, as compared to a clean window, shown in Figure 37b.

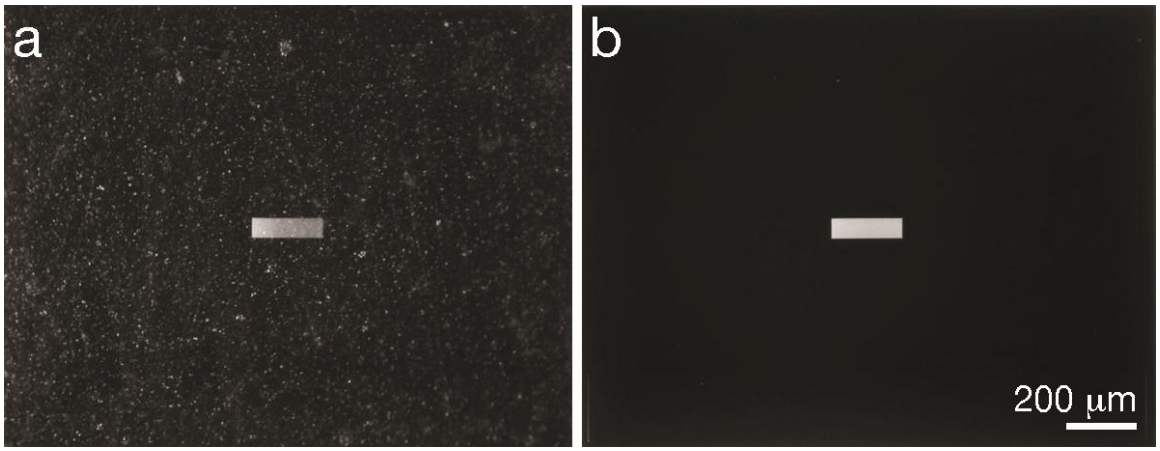

Figure 37: Photographs showing the difference between coated and clean microchips. (a) A microchip with a protective resist coat, covered in debris is shown. (b) The same microchip after washing with acetone, ethanol, and water.

The windows were hydrophobic after stripping the resist, but were made hydrophilic for use with biological samples by plasma cleaning for several minutes, usually 3-7. The hydrophilicity lasted for about a day. After plasma cleaning, the microchips were washed with H2O (also HPLC grade) to remove any remainders of debris and salt. Next, the microchips were coated with poly-L-lysine to extend the duration of their hydrophilicity and to promote cell adhesion. This coating was accomplished by immersing the microchips in a solution of 0.01% poly-L-lysine for five minutes at room temperature. Excess poly-L-lysine was removed by soaking the microchips three times briefly in fresh volumes of HPLC grade water. The microchips were inspected under an optical microscope after each cleaning step.

If polystyrene microspheres were used for a spacer layer, they needed to be applied on hydrophobic microchips, thus before plasma cleaning. 0.2 μl droplets containing the beads in aqueous solution were placed at the corners of a microchip. If the droplets were applied after plasma cleaning, the entire microchip surface was wetted, and

the microspheres were not confined to the corners. There should be ~5-20 beads in each droplet, depending on the size of microspheres used.

B.3 Biological sample preparation

After the microchips had been prepared for cell culture, they were transferred to a ninety-six well cell culture plate, as shown in Figure 38a, for biological experiments, including cell seeding, labeling, fixation, staining and dehydration.

B.3.1 Cell seeding

Each step of the cell seeding process was accomplished by transferring the microchips to a new well of the 96 well plate. The microchips were transferred between wells using Teflon coated tweezers with flat tips, to minimize adherence of the microchips to the tweezers, and to prevent damage to the edges of the microchips. They were held such that the microchips remained upright (flat-side up) at all times, and the tweezers did not come into contact with the surface of the microchip, except at the edges, as shown in Figure 38a. If a microchip was placed into a well with a solution and then immediately (within ~10 seconds) placed into a new well, that was termed "rinsing" whereas if a microchip was placed into a well and left for a longer amount of time, that was termed "immersing" or "incubating".

The microchips were first immersed in ~150 µL of cell media per well. Confluent cells were detached from a culture flask using a cell stripper solution such as trypsin, and then re-suspended in cell media. We typically re-suspended cells grown in a 25 cm^3 culture flask in 5 mL of media, which we counted to be ~$(1\text{-}3)\times10^5$ cells/mL for COS7 cells, as determined using a hemocytometer.

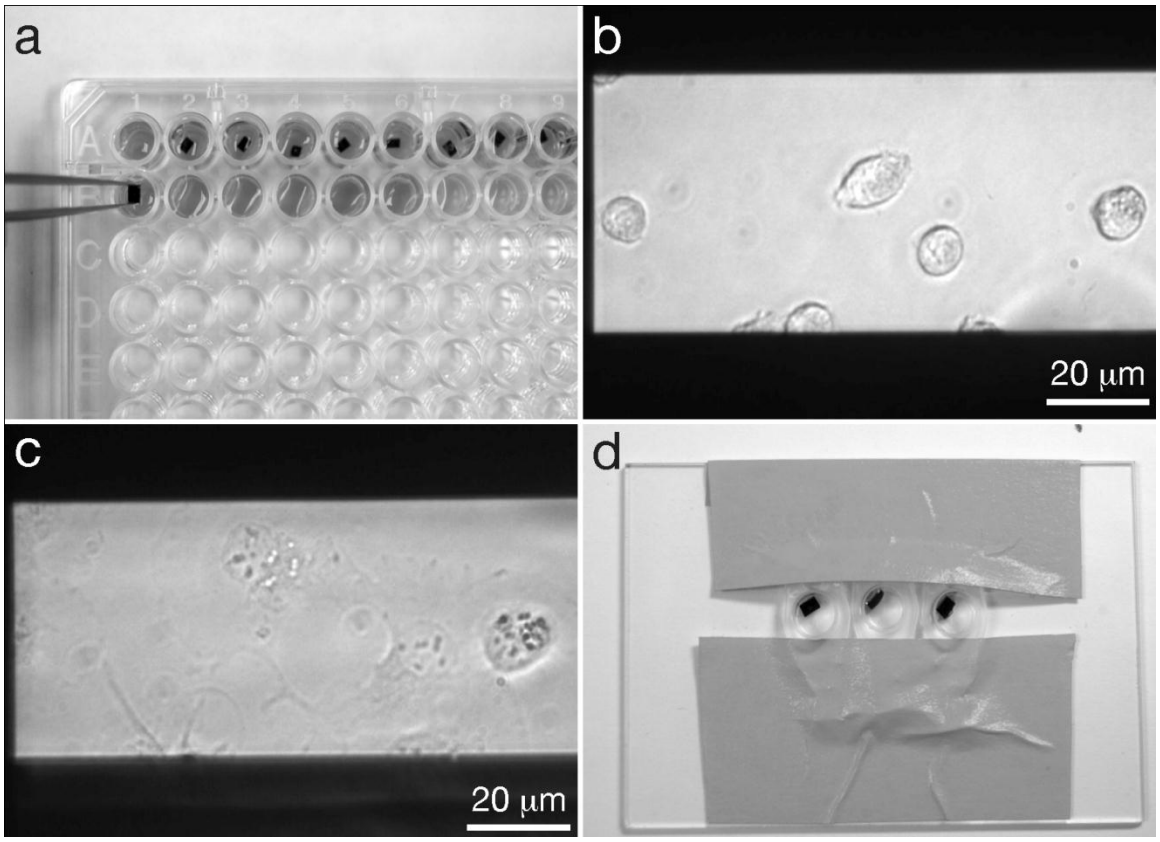

Figure 38: Seeding cells onto microchips and labeling the cells. (a) Microchips in a 96 well plate, where they will be seeded with cells, and the cells will be fixed. Note the orientation of the tweezers gripping microchips by their sides and not their top surfaces. Tweezers with a teflon coated flat tips are recommended. (b) COS7 cells on windows after ~5 minutes of incubation. (c) COS7 cells that have adhered to a window, after ~1 hour of incubation. (d) Microchips in labeling device are inclined against a drop of labeling solution to reduce the amount of non-specifically bound label on the sample.

A droplet of the cell suspension was added to each well containing a microchip and media. After ~1 minute the microchips were inspected with an inverted light microscope to verify that cells had begun to adhere to the windows. A microchip should have no more than ~1 adhered cell per 50 x 50 μm^2 area. The presence of more cells than this inhibits them from flattening against the window. If after ~5 minutes, the desired amount of cells had not begun to adhere to the window, we added another droplet of the cell suspension. If too many cells were present, we typically discarded the microchips, although the amount of cells could sometimes be sufficiently reduced by transferring the

chip into a new well with fresh media, which washed away cells that had not yet tightly adhered to the window surface.

Once the desired amount of cells had begun adhering to the window, as seen in Figure 38b, the microchips were immersed in a new well with media and incubated for at least 4 hours at 37°C in 5% CO_2. For certain experiments, the cells were incubated in serum-free media for 2-12 hours prior to labeling, as this enhances the cells' ability to uptake certain protein-coupled labels. An example of cells adhered to the surface is shown in Figure 38c.

B.3.2 Cell labeling

Just as fluorescent tags can be used to image specific proteins in LM, nanoparticles made of high atomic number materials, such as gold, can be used to image specific proteins in EM. For example, it has been shown that epidermal growth factor (EGF) coupled to either quantum dots (QD) or gold nanoparticles could be used to label the EGF receptor.[63,169]

To label the cells with protein-coupled labels, the following method was used, based on live cell labeling protocols developed by others.[175,176] The microchips with adhered cells were first rinsed with Tyrode's buffer containing 1-3% Bovine Serum Albumen (BSA) to reduce non-specific label binding. The chips were then placed in the labeling solution. Incubating the microchips in an inclined position, with the cells facing downwards, was found to reduce unspecific binding with certain labels, such as larger diameter gold nanoparticles, probably by reducing the effect of gravity on the labels. The rim of the 96 well plate wells are too high to allow for the maneuvering of the microchips into such a position, so we made simple labeling devices using lids of 0.2 mL

microcentrifuge tubes that were clipped from the tubes and fixed with tape onto a large glass microscope slide, as shown in Figure 38d.

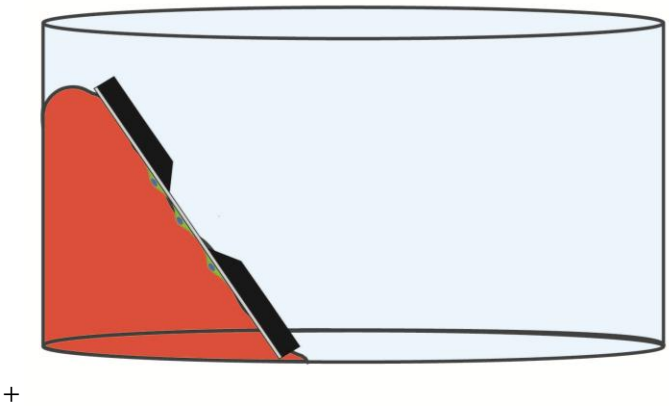

Figure 39: Detail of labeling using a droplet of labeling solution. The droplet is placed at the edge of the well, such that it is in contrast with both the side and bottom of the well. The SiN microchip is then leaned against the droplet with the cell side submerged.

For the labeling, a droplet of gold nanoparticle label solution was deposited at the edge of such a plastic well, and a microchip was inclined against the droplet, as shown in Figure 39. The microchip was inclined against, rather than immersed in, the labeling solution in order to reduce background due to the gravitational settling of gold nanoparticles. We have found that other labels, such as streptavidin-QDs or lipoprotein bound gold nanoparticles, undergo negligible settling. In such instances the microchip may simply be immersed in a well containing labeling solution. For long incubation times (longer than 5 minutes) these labeling devices were placed into a humid environment, such as a plastic box containing damp paper towels, to prevent evaporation of the labeling solution. The duration of incubation was defined by the protein-label pair used, and the purpose of the experiment. For example, to examine membrane bound EGF with gold nanoparticles

(EGF-Au) before internalization occurs,[123] the microchips were incubated for 5 - 10 minutes at room temperature.[63] After incubation with the label, the microchips were rinsed with Tyrode's buffer containing BSA to remove any unbound label, and further processed for fixation.

B.2.3 Cell fixation and staining

Fixation of biological samples can help to protect them from degradation during sample preparation and imaging. Fixation of cells attached to SiN windows for EM is analogous to the fixation of fluorescence microscopy samples. However, instead of the typical LM fixatives (i.e. paraformaldehyde, formalin), glutaraldehyde is used, as it is a stronger EM fixative.[13]

For fixation, the microchips were immersed in a 4% glutaraldehyde solution in Phosphate Buffer Saline (PBS) at room temperature for at least 20 minutes. After this step, the cells were rinsed three times in PBS to remove excess glutaraldehyde, followed by three five-minute immersions in 10% PBS in water to remove excess salt. If the cells were to be air dried, an additional soaking step in pure water was performed.

In some cases it was required to post-fix and stain the samples with osmium tetroxide, which aids fixation by increasing lipid stability, and also increases contrast during EM. [3] In that case, the microchips were first rinsed with cacodylate buffer (0.1M, pH 7.4) , and then immersed in a osmium tetroxide solution 1% in cacodylate buffer for 1 hour at 37 ºC with 5% CO_2. We later found that a much lower osmium tetroxide concentration of 0.001% provided sufficient contrast and sample stability; and also that the required time could be lower to 30 min, even at room temperature. Because the sample consists of a monolayer of thin cells only, presumably the fixation conditions are

relaxed as compared to tissue samples. The microchips were then rinsed for 5 minutes each, first 3 times in cacodylate buffer, and then 3 times in water times to remove salts. The samples were stored in the refrigerator overnight before use.

B.3.4 Sample drying

For standard EM imaging, the sample must first be dried before it can be imaged in the vacuum of the electron microscope. Any water left in a sample will evaporate upon exposure to vacuum, resulting in structural damage and instability of the sample.[2]

The sample can be air dried in principle (after removal of salts via soaking in pure water), but the high surface tension of water typically causes cellular damage that can be seen in high-resolution imaging. Preferably, the water is replaced by ethanol, which causes less damage upon drying as it has a smaller surface tension than water. A graded ethanol series was used for dehydration. The samples were immersed in each of the following grades of ethanol for 5 minutes: 20%, 30%, 50%, 70%, 95%; and then immersed 3 times in 100% ethanol for 10 minutes each. EM-grade ethanol, with a very low concentration of water, was used. Samples were then air dried for 30 min, and used for imaging. We have also used hexamethildisilazane (HMDS) [8] to replace the ethanol for a further reduction of the surface tension, and thus to reduce the damaging occurring during drying. Just after ethanol dehydration, microchips were immersed for 5 minutes in an ethanol/HMDS (1:2) mixture, then 2 times in pure HMDS, and allowed to air dry for 30 minutes.

An alternate way to dry samples with minimal damage to the cellular structure is critical point drying. Critical point drying is the process of drying a sample by raising the

temperature and pressure such that the sample transitions from the liquid phase to the gas phase above the critical point. This eliminates damage deriving from the surface tension effects that occur if the sample crosses the phase boundary,[2] and thus prevents collapse of the sample during dehydration. For critical point drying the microchips were placed in the chamber of the critical point drier (CPD) after the graded ethanol dehydration, while remaining immersed in 100% ethanol. Liquid CO_2 was flushed through the chamber of the CPD for one minute, followed by a five-minute soak, a cycle that was repeated until the fluid exchange was complete. The chamber was then heated under pressurized conditions to the critical point of CO_2 (31.1 ºC, 1072 psi), and once this point was reached, the pressure was reduced over a period of 45 minutes. After any drying method that was used, samples were always stored under desiccated conditions until imaging.

B.3.5 Comparison to current techniques

The sample preparation process using SiN windows shares some similarities to current TEM preparation procedures,[2,3] but also offers several advantages. Most conventional cell preparations involve fixation, post-staining, and drying of the samples. The cells are typically embedded in resin, such that they can be sliced into thin sections using an ultramicrotome. The embedded sections are transferred to metal or carbon grids, typically by floating the sample on water above a grid, and then draining that water. The inclusion of fluorescent tags can be used for correlative fluorescence microscopy and TEM of thin sections.[119,170]

Whole-mount cell samples can be prepared on grids coated with a thin film such as carbon.[177] Cells can be cultured, fixed, stained, and dried, for example, with critical-

point drying.[2] Alternatively, wet samples can be rapidly frozen for cryo TEM. This type of sample preparation is often used in correlative microscopy.[53,74]

The silicon microchips are compatible with both LM and EM and provide the most robust sample support. All steps in the preparation process are compatible with current biological protocols and equipment, *e.g.*, the microchips fit in the well of a standard 96 well plate, and live cells on the microchips can be imaged with LM. When the size and the thickness of the SiN windows are chosen correctly, they do not break, or wrinkle, although the window area is limited. The cells are cultured, labeled, fixed, stained, dried, and imaged directly on the microchip. In order to visualize labels, the samples can be easily air-dried, or critical-point drying can be used. We have shown that the microchips can be used to image fixed cells in a liquid environment,[63] which is not possible when using grids. We have not tested if cryo samples can be prepared, but this should be possible in principle.

B.4 Microscopy

The cells prepared on microchips accommodate several different imaging modalities. The cells can be imaged with LM (dry or wet), either placed in a standard dish, or in the liquid (S)TEM specimen holder. Dry microchips can be examined with both STEM and TEM. Eukaryotic cells in the microfluidic chamber can be imaged with liquid STEM. Figure 40 summarizes the possible imaging modalities, of which examples are provided in the following section.

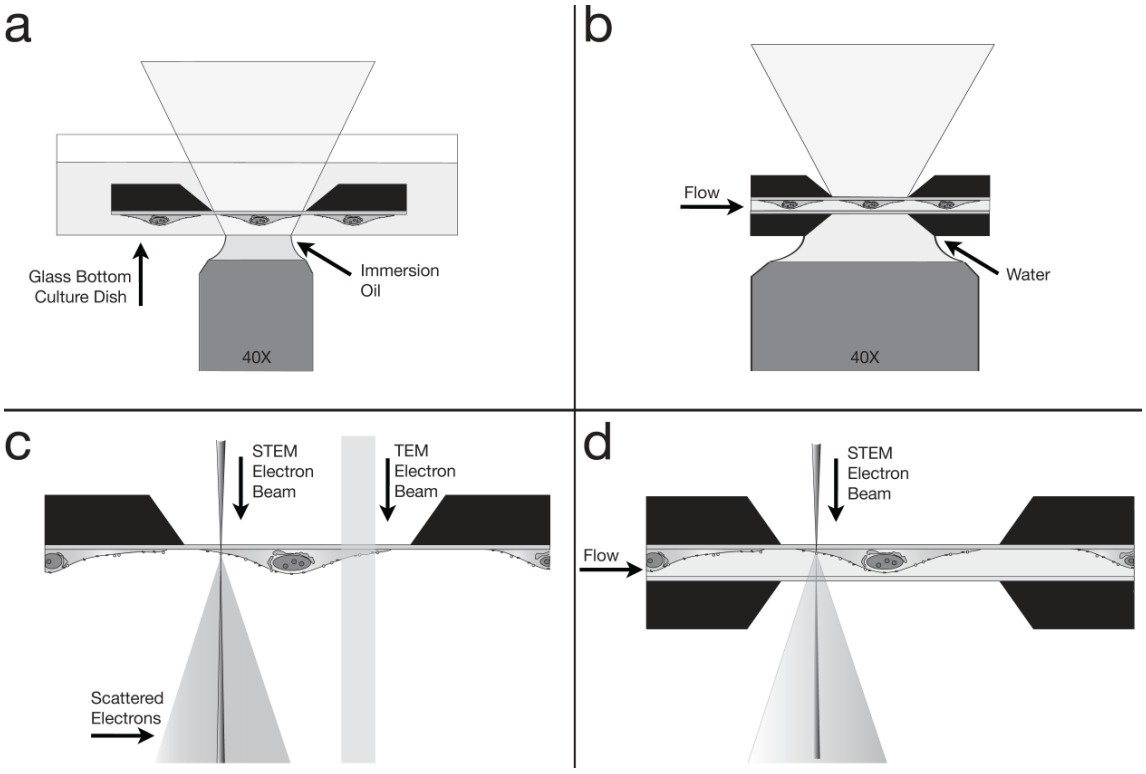

Figure 40: Schematics showing different ways microchips can be used for imaging. (a) The microchip can be imaged in liquid in a standard dish with LM. (b) Two microchips enclosing a sample in liquid can be imaged with LM. (c) A dry sample on a microchip can be imaged with transmission electron microscopy (TEM), or the scanning TEM (STEM). (d) Two microchips enclosing a cell in liquid can be imaged with STEM; thin samples can be imaged in liquid TEM as well. Drawings not to scale.

B.4.1 Light microscopy

For LM imaging, the microchip with the cellular sample can simply be inverted onto a glass bottom culture dish containing saline water, and imaged in an inverted LM, following typical LM protocols, as shown in Figure 40a. A fluorescence image of QD labeled EGF receptors on COS7 cells in 10% PBS in water buffer is shown in Figure 41a.[169]

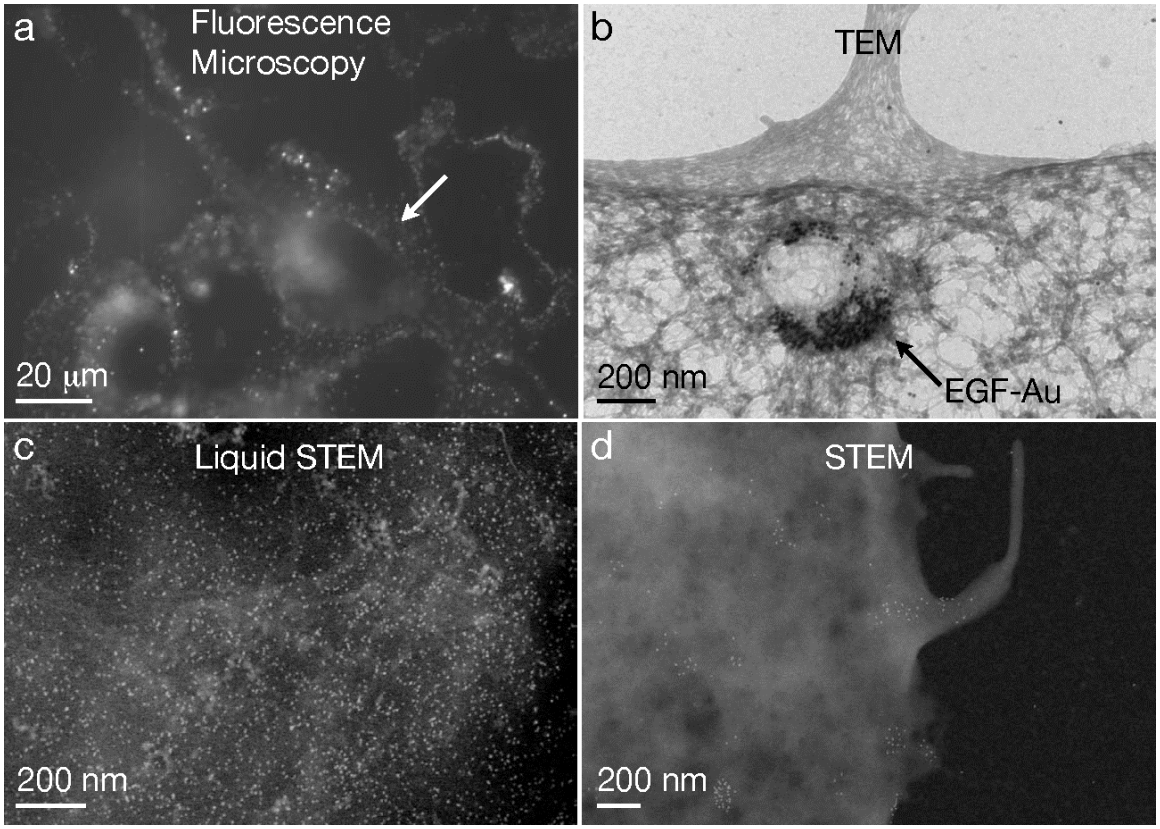

Figure 41: Examples of micrographs of cellular samples on microchips obtained with different microscopy modalities. (a) Fluorescence image showing epidermal growth factor (EGF)-quantum dot (QD) labeled COS7 fibroblast cells in saline water. (b) TEM image of EGF-Au nanoparticles in a vesicle in a fixed and dried COS7 cell. (c) Liquid STEM image recorded at the location of the arrow in (a). Individual QDs are visible on a background of biological material. (d) Dry STEM image of EGF-QD labels on the edge of a COS7 cell.

The sample was incubated with labeling solution for 5 minutes, and then fixed with glutaraldehyde, such that the E GF-QDs remained on the cell membrane.[63,123] The cellular surface is covered with bright spots. Possibly, activated EGF receptors at the cell membrane were in the process of forming clusters and coated pits at the onset of endocytosis. Additional fluorescence is visible in the nuclear region, presumably autofluorescence of the fixative. The image in Figure 40a was recorded using a widefield microscope (TE300, Nikon), with a 40X oil immersion objective, equipped with a far-red bandpass exitation filter (hq615/40 X) and a far-red emission filter set (hq710/100 m).

The exposure time was 5 seconds. To reduce the autofluorescence of the glutaraldehyde fixative the samples where illuminated with the light source of the microscope for several minutes. The brightness and contrast of all images were optimized for contrast and brightness using ImageJ software (NIH).

The sample can also be assembled in a microfluidic chamber in the tip of the liquid (S)TEM holder, and the holder can be positioned on a microscope stage to study the sample with LM, as illustrated in Figure 41b. The best microscopy results were obtained with a water immersion objective (data not shown). The space between the lens and the lower window was filled with water. Water immersion objectives allow working distances of several mm for a large numerical aperture (NA) values (typically NA = 1). A dry objective (with a lower NA than the water immersion objective) was also used, leaving an air gap between the lens and the window. It turned out to be impractical to use an oil immersion objective, because it was difficult to 1) ensure that the gap was entirely filled with oil, and 2) remove the oil from the microchips and specimen holder for subsequent liquid STEM.

B.4.2 Transmission electron microscopy

Dried samples can be viewed with standard TEM and STEM. The imaging setup for TEM, as well as for (dry) STEM imaging is shown schematically in Figure 41c. Figure 41b shows an example of TEM of an EGF-Au labeled COS7 cell. The sample was incubated with the labeling solution for 10 minutes, and then with Tyrode's Buffer for 10 minutes more. After fixation, it was post-fixed with osmium tetroxide, and dried using a graded ethanol series/HMDS drying method. The EGF coupled nanoparticles are visible, concentrated in a large vesicle located near a filipodium, consistent with the idea

that filipodia may be found in proximity of receptors like the EGF receptor.[178] This image was taken on a TEM (CM12, Philips) operating at 120 kV equipped with a 2k X 2k CCD camera. The microchip was placed in the TEM specimen holder with the cells facing downward; thus the SiN window did not interfere with the electron beam between the specimen and the projection system.

B.4.3 Scanning transmission electron microscopy

One of the main advantages of these microchips is the ability to assemble cellular samples in buffer solution into a microfluidic chamber placed in a specimen holder for liquid STEM.[63,169] The specimen holder accommodates liquid flow in the specimen region,[173] such that the microfluidic chamber is entirely filled with liquid even when placed in the vacuum of the electron microscope, and this system opens the possibility of live-cell experiments. We have previously demonstrated nanometer resolution on gold nanoparticles and QDs used to tag EGF on whole fixed eukaryotic cells (COS7) in their native liquid state. A schematic of the imaging setup is shown in Figure 40d.

Liquid STEM is particularly useful in correlation with LM. Cells can be maintained in liquid in the microfluidic chamber and imaged with LM to provide overview images of the cells. Cellular regions can then be imaged at high resolution with liquid STEM, zooming-in on regions of interest with nanoscale resolution. If bi-modal labels are used, LM can reveal the locations of regions of tagged proteins with respect to the cellular structure, while liquid STEM provides information of the distribution of the labels at the level of individual proteins. We have for example, imaged the same cell of which the fluorescence image is shown in Figure 41a, with liquid STEM. Figure 41c reveals the locations of individual QDs on a background of signal from the biological

material (the resolution obtained on the cellular material is much lower than that obtained on the labels, because the contrast mechanism of STEM depends on the atomic number(s) of the material(s) in the sample). The QDs are densely packed, which suggest that the EGF receptor had begun to concentrate together at the cellular surface, which is a step preceding the formation of endocytotic pits.[146] Thus, where we observed a bright spot in the LM image, we found a high density of QDs in the liquid STEM image. We did not find QDs in regions outside of the cell. Fig. 6c was recorded with a 200 kV STEM (CM200, FEI), a pixel-dwell time of 20 µs, 1024×1024 pixels, a probe current of 0.68 nA, an electron probe semi-angle of 11 mrad, an annular dark field detector semi-angle of 70 mrad, a pixel size of 1.6 nm, and a magnification of 80,000. The noise in the mage was reduced by using a convolution filter (in ImageJ) with a kernel of (1, 1, 1; 1, 3, 1; 1, 1, 1). In Figure 41a and c we assembled the microfluidic chamber after LM, but we have also successfully tested LM and subsequent liquid STEM of cells already in the microfluidic chamber. In that case, the amount of time needed for the transfer between the two microscopy modalities can be as short as a minute, mainly set by the vacuum pumping time, and this time determines the temporal correlation. Shorter times can be obtained using integrated LM and (S)TEM.[179] For samples thinner than about 1 µm liquid samples can also be viewed with TEM [180].

The microchips can also be used for imaging dried samples in the STEM, as shown schematically in Figure 40c. An example of an image of a dried STEM sample is shown in Figure 41d. The sample was prepared in the same way as that shown in Figure 41a and c, (*i.e.*, used EGF-QDs), and then dehydrated using a graded ethanol series, and air-dried. Individual EGF-QDs are visible along the edge of a dried COS7 cell. In this

case, the cellular ultrastructure is visible with a much better contrast and resolution than in the case of liquid STEM, since the contrast is now obtained against a background of the SiN window only, instead of against a column of liquid as in liquid STEM. Figure 40d was recorded at the same microscope settings as Figure 40c, but with a magnification of 48,000 and a pixel size of 2.7 nm. The microchip was placed in a modified single-tilt specimen holder that had a 0.2 mm deeper sample slot. The microchip was positioned with the cell side facing upwards, such that the STEM probe was unperturbed by the SiN window, and the sample was imaged at the highest possible resolution.

An important benefit of using SiN membranes for EM imaging is their versatility. Typically, biological sample preparation techniques are chosen based on the type of imaging modality desired, and the possibility for using different or additional modalities may be limited based on the type of support chosen. However, this is not a problem when microchips supports are used. As illustrated in Figure 42, starting with the same basic cell culture steps, essentially any desired imaging modality may be used.

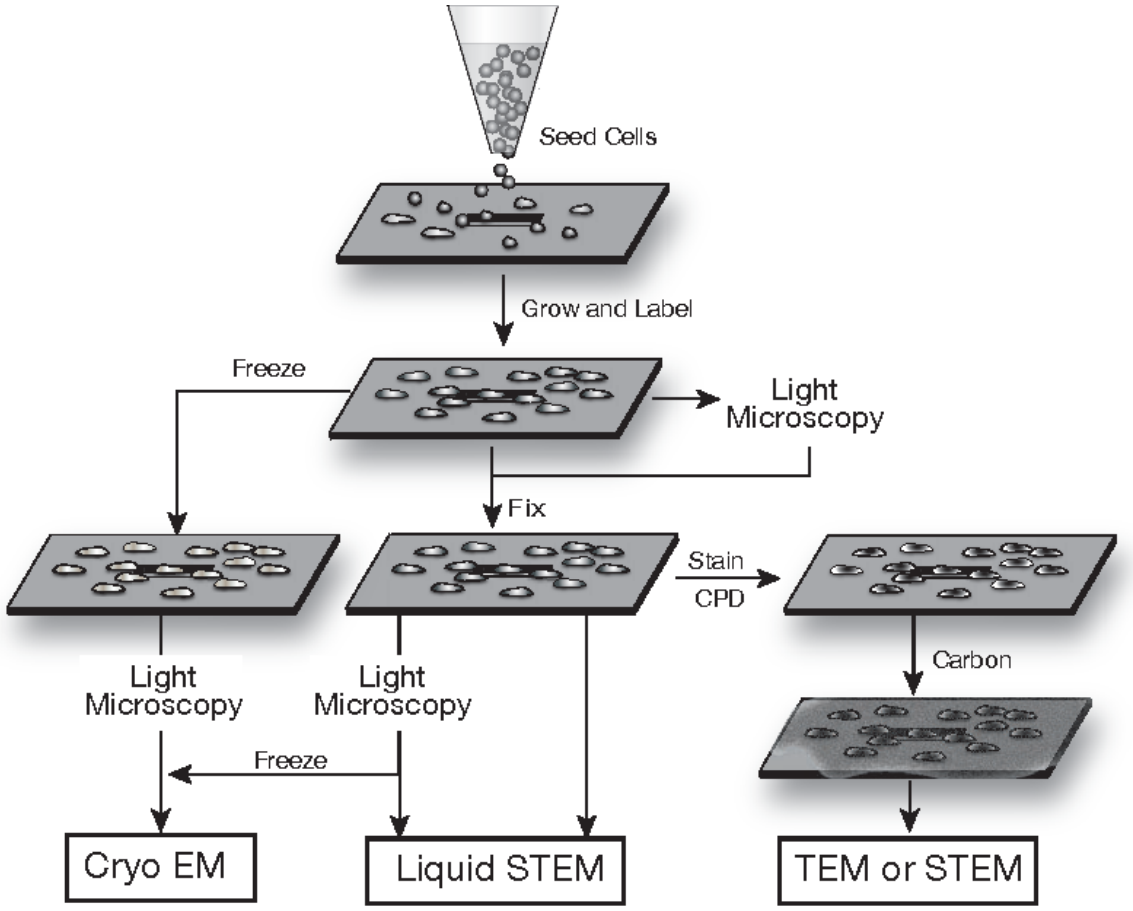

Figure 42: Diagram illustrating the versatility of the silicon microchip support for whole mount cell samples for imaging with different modalities. Cells are seeded onto a clean poly-L-lysine coated microchip, and grown and labeled (if needed) directly on the support. Live cells can be imaged with LM. The cells can then be fixed, or frozen (freezing was not yet tested and this branch in the schematics is, therefore, indicated with a dashed line). Fixed cells can undergo additional sample preparation steps for EM processing such as staining, dehydrating and evaporative coating, as needed. This sample preparation system permits multiple samples to be prepared under the same conditions, and efficiently processed for cryo EM, liquid STEM, TEM, and dry STEM. Thin biological samples can also be imaging with liquid TEM. The cells can be imaged at different stages with LM enabling correlative imaging studies to be performed. Drawings not to scale.

Cells are grown and labeled directly on the microchips, and may be viewed in the light microscope at any point after this. While sample freezing and cryo-EM have not yet been demonstrated, we expect that this should be possible. Alternatively, the samples could be fixed and then imaged using both LM and STEM for samples in liquid, with no further preparation steps required. If imaging the samples in liquid is not desired, the samples

could be prepared using any other standard (S)TEM sample preparation procedure, and be imaged in both light and electron microscopes. The silicon microchips are compatible with all current biological protocols and equipment. Thus, they can be easily incorporated into current practices, streamlining laboratory procedures.

B.5 Conclusions

Silicon microchips with thin electron transparent SiN windows provide robust supports for both LM and EM of whole eukaryotic cells in vacuum, or liquid. These microchip supports are suitable for a range of imaging modalities including LM, TEM, and dry, and liquid STEM, without imposing the need for different preparation protocols, except for the drying step, if desired. This minimizes sample processing. When using liquid STEM, the sample preparation is similar to standard LM sample preparation using fixation. Most importantly, the presented microchip sample support can be used for experimental series where samples are studied with different microscopy modalities in correlative approaches.

BIBLIOGRAPHY

1. Williams, D. B.; Carter, C. B. *Transmission Electron Microscopy: A Textbook for Materials Science*; Springer: New York, 1996; Vol. 1.

2. Bozzola, J. J.; Russell, L. D. In *Electron Microscopy Principles and Techniques for Biologists*; 2nd ed.; Jones and Barlett Publishers: Boston, 1999.

3. Gluaert, A. M.; Lewis, P. R. *Biological Specimen Preparation for Transmission Electron Microscopy*; Princeton University Press: Boston, 1998; Vol. 17.

4. Hayat, M. A. *Principles and Techniques of Electron Microscopy Biological Applications*; 4th ed.; Cambridge University press: Cambridge, 2000.

5. Pierson, J.; Sani, M.; Tomova, C.; Godsave, S.; Peters, P. *Histochemistry and Cell Biology* **2009**, *132*, 253-262.

6. Lučić, V.; Förster, F.; Baumeister, W. *Annu. Rev. Biochem.* **2005**, *74*, 833-865.

7. Borrelli, M. J.; Koehm, S.; Cain, C. A.; Tompkins, W. A. F. *Journal of Ultrastructure Research* **1985**, *91*, 57-65.

8. Braet, F.; deZanger, R.; Wisse, E. *Journal of Microscopy-Oxford* **1997**, *186*, 84-87.

9. Ris, H. *J. Cell Biol.* **1985**, *100*, 1474-1487.

10. Mollenhauer, H. H. *Microsc Res Tech* **1993**, *26*, 496-512.

11. McDonald, K. L. *Journal of Microscopy-Oxford* **2009**, *235*, 273-281.

12. He, W. Z.; Kivork, C.; Machinani, S.; Morphew, M. K.; Gail, A. M.; Tesar, D. B. B.; Tiangco, N. E.; McIntosh, J. R.; Bjorkman, P. J. *Journal of Structural Biology* **2007**, *160*, 103-113.

13. Hopwood, D. *Histochem. Cell Biol.* **1969**, *17*, 151-161.

14. Vadillo-Rodriguez, V.; Busscher, H. J.; Norde, W.; de Vries, J.; Dijkstra, R. J. B.; Stokroos, I.; van der Mei, H. C. *Applied and Environmental Microbiology* **2004**, *70*, 5541-5546.

15. Lindroth, M.; Bell, P. B.; Fredriksson, B. A.; Liu, X. D. *Microsc Res Techniq* **1992**, *22*, 130-150.

16. de Jonge, N.; Sougrat, R.; Peckys, D. B.; Lupini, A. R.; Pennycook, S. J. *Nanotechnology in Biology and Medicine: Methods, Devices, and Applications* **2007**.

17. Pawley, J. *Handbook of Biological Confocal Microscopy*; Springer, 2006.

18. Abbe, E. *Journal of the Royal Microscopy Society* **1883**, *2*, 790-812.

19. Fernandez-Suarez, M.; Ting, A. Y. *Nat. Rev. Mol. Cell Biol.* **2008**, *9*, 929-943.

20. Bates, M.; Huang, B.; Zhuang, X. W. *Curr. Opin. Chem. Biol.* **2008**, *12*, 505-514.

21. Bossi, M.; Folling, J.; Dyba, M.; Westphal, V.; Hell, S. W. *New Journal of Physics* **2006**, *8*.

22. Bretschneider, S.; Eggeling, C.; Hell, S. W. *Physical Review Letters* **2007**, *98*.

23. Huang, B.; Bates, M.; Zhuang, X. W. *Annu. Rev. Biochem.* **2009**, *78*, 993-1016.

24. Betzig, E.; Patterson, G. H.; Sougrat, R.; Lindwasser, O. W.; Olenych, S.; Bonifacino, J. S.; Davidson, M. W.; Lippincott-Schwartz, J.; Hess, H. F. *Science* **2006**, *313*, 1642-1645.

25. Steinhauer, C.; Forthmann, C.; Vogelsang, J.; Tinnefeld, P. *Journal of the American Chemical Society* **2008**, *130*, 16840-+.

26. Lippincott-Schwartz, J.; Manley, S. *Nature Methods* **2009**, *6*, 21-23.

27. Shtengel, G.; Galbraith, J. A.; Galbraith, C. G.; Lippincott-Schwartz, J.; Gillette, J. M.; Manley, S.; Sougrat, R.; Waterman, C. M.; Kanchanawong, P.; Davidson, M. W.; Fetter, R. D.; Hess, H. F. *Proceedings of the National Academy of Sciences of the United States of America* **2009**, *106*, 3125-3130.

28. Rust, M. J.; Bates, M.; Zhuang, X. W. *Nature Methods* **2006**, *3*, 793-795.

29. Bates, M.; Huang, B.; Dempsey, G. T.; Zhuang, X. W. *Science* **2007**, *317*, 1749-1753.

30. Zhuang, X. W. *Nature Photonics* **2009**, *3*, 365-367.

31. Somekh, M. G.; Hsu, K.; Pitter, M. C. *Journal of the Optical Society of America a-Optics Image Science and Vision* **2009**, *26*, 1630-1637.

32. Davis, I. *Biochemical Society Transactions* **2009**, *37*, 1042-1044.

33. Eggeling, C.; Ringemann, C.; Medda, R.; Schwarzmann, G.; Sandhoff, K.; Polyakova, S.; Belov, V. N.; Hein, B.; von Middendorff, C.; Schoenle, A.; Hell, S. W. *Nature (London)* **2009**, *457*, 1159.

34. Nagerl, U. V.; Willig, K. I.; Hein, B.; Hell, S. W.; Bonhoeffer, T. *Proceedings of the National Academy of Sciences of the United States of America* **2008**, *105*, 18982-18987.

35. Vogelsang, J.; Cordes, T.; Forthmann, C.; Steinhauer, C.; Tinnefeld, P. *Proceedings of the National Academy of Sciences of the United States of America* **2009**, *106*, 8107-8112.

36. Willig, K. I.; Rizzoli, S. O.; Westphal, V.; Jahn, R.; Hell, S. W. *Nature* **2006**, *440*, 935-939.

37. Schermelleh, L.; Heintzmann, R.; Leonhardt, H. *J. Cell Biol.* **2010**, *190*, 165-175.

38. Knoll, M.; Ruska, E. *Annalen der Physik* **1932**, *404*, 607-640.

39. Demers, H.; Poirier-Demers, N.; Drouin, D.; de Jonge, N. *Microscopy and Microanalysis* **2010**, *16*, 795-804.

40. McBride, J.; Treadway, J.; Feldman, L. C.; Pennycook, S. J.; Rosenthal, S. J. *Nano Lett.* **2006**, *6*, 1496-1501.

41. Massover, W. H. *Micron* **2011**, *42*, 141-151.

42. Anderson, T. F. *Trans. NY. Acad. Sci.* **1951**, *13*, 130-134.

43. Bridgman, P. C.; Reese, T. S. *J. Cell Biol.* **1984**, *99*, 1655-1668.

44. Bouchet-Marquis, C.; Hoenger, A. *Micron* **2011**, *42*, 152-162.

45. Lucic, V.; Leis, A.; Baumeister, W. *Histochemistry and Cell Biology* **2008**, *130*, 185-196.

46. Sousa, A. A.; Hohmann-Marriott, M.; Aronova, M. A.; Zhang, G.; Leapman, R. D. *Journal of Structural Biology* **2008**, *162*, 14-28.

47. Courty, S.; Bouzigues, C.; Luccardini, C.; Ehrensperger, M. V.; Bonneau, S.; Dahan, M. *Measuring Biological Responses with Automated Microscopy* **2006**, *414*, 211-228.

48. Hainfeld, J. F.; Powell, R. D. *Journal of Histochemistry & Cytochemistry* **2000**, *48*, 471-480.

49. Jamur, M. C.; Oliver, C. 2009; Vol. 588, p 63-66.

50. Leis, A.; Rockel, B.; Andrees, L.; Baumeister, W. *Trends Biochem.Sci.* **2009**, *34*, 60-70.

51. Cortese, K.; Diaspro, A.; Tacchetti, C. *Journal of Histochemistry & Cytochemistry* **2009**, *57*, 1103-1112.

52. Midgley, P. A.; Weyland, M. *Ultramicroscopy* **2003**, *96*, 413-431.

53. Sartori, A.; Gatz, R.; Beck, F.; Rigort, A.; Baumeister, W.; Plitzko, J. M. *Journal of Structural Biology* **2007**, *160*, 135-145.

54. Bárcena, M.; Koster, A. J. *Seminars in Cell & Developmental Biology* **2009**, *20*, 920-930.

55. Koning, R. I.; Koster, A. J. *Annals of Anatomy - Anatomischer Anzeiger* **2009**, *191*, 427-445.

56. Ren, Y.; Kruhlak, M. J.; Bazett-Jones, D. P. *The Journal of Histochemistry & Cytochemistry* **2003**, *51*, 605-612.

57. Nisman, R.; Dellaire, G.; Ren, Y.; Li, R.; Bazett–Jones, D. P. *Journal of Histochemistry and Cytochemistry* **2004**, *52*, 13-18.

58. Yakushevska, A. E.; Lebbink, M. N.; Geerts, W. J. C.; Spek, L.; van Donselaar, E. G.; Jansen, K. A.; Humbel, B. M.; Post, J. A.; Verkleij, A. J.; Koster, A. J. *Journal of Structural Biology* **2007**, *159*, 381-391.

59. de Jonge, N.; Sougrat, R.; Northan, B. M.; Pennycook, S. J. *Microscopy and Microanalysis* **2010**, *16*, 54-63.

60. Aoyama, K.; Takagi, T.; Hirase, A.; Miyazawa, A. *Ultramicroscopy* **2008**, *109*, 70-80.

61. Einspahr, J. J.; Voyles, P. M. *Ultramicroscopy*, *106*, 1041-1052.

62. Ramachandra, R.; Dremers, H.; Jonge, N. d. *Appl. Phys. Lett* **2011**, In Press.

63. de Jonge, N.; Peckys, D. B.; Kremers, G. J.; Piston, D. W. *Proceedings of the National Academy of Sciences of the United States of America* **2009**, *106*, 2159-2164.

64. Reimer, L.; Kohl, H. *Transmission Electron Micrscopy: Physics of Image Formation*; Springer: New York, 2008.

65. Giepmans, B. N. G.; Deerinck, T. J.; Smarr, B. L.; Jones, Y. Z.; Ellisman, M. H. *Nature Methods* **2005**, *2*, 744-749.

66. Bakalova, R.; Zhelev, Z.; Aoki, I.; Ohba, H.; Imai, Y.; Kanno, I. *Analytical Chemistry* **2006**, *78*, 5925-5932.

67. Bridot, J. L.; Dayde, D.; Riviere, C.; Mandon, C.; Billotey, C.; Lerondel, S.; Sabattier, R.; Cartron, G.; Le Pape, A.; Blondiaux, G.; Janier, M.; Perriat, P.; Roux, S.; Tillement, O. *Journal of Materials Chemistry* **2009**, *19*, 2328-2335.

68. Cheon, J.; Lee, J. H. *Accounts of Chemical Research* **2008**, *41*, 1630-1640.

69. Gao, J. H.; Gu, H. W.; Xu, B. *Accounts of Chemical Research* **2009**, *42*, 1097-1107.

70. Manning, H. C.; Goebel, T.; Thompson, R. C.; Price, R. R.; Lee, H.; Bornhop, D. J. *Bioconjugate Chem.* **2004**, *15*, 1488-1495.

71. Prinzen, L.; Miserus, R.; Dirksen, A.; Hackeng, T. M.; Deckers, N.; Bitsch, N. J.; Megens, R. T. A.; Douma, K.; Heemskerk, J. W.; Kooi, M. E.; Frederik, P. M.; Slaaf, D. W.; van Zandvoort, M.; Reutelingsperger, C. P. M. *Nano Letters* **2007**, *7*, 93-100.

72. Koster, A. J.; Klumperman, J. *Nat. Rev. Mol. Cell Biol.* **2003**, SS6-SS10.

73. Chen, J. F.; Cheng, Y. *Optics Letters* **2009**, *34*, 1831-1833.

74. van Rijnsoever, C.; Oorschot, V.; Klumperman, J. *Nature Methods* **2008**, *5*, 973-980.

75. Giepmans, B. N. G. *Histochem. Cell Biology* **2008**, *130*, 211-217.

76. Mironov, A. A.; Beznoussenko, G. V. *Journal of Microscopy-Oxford* **2009**, *235*, 308-321.

77. Bozzola, J. J.; Russell, L. D. In *Electron Microscopy: Principles and Techniques for Biologists*; 2nd ed.; Jones and Bartlett Publishers: Boston, 1999, p 278.

78. Meißlitzer-Ruppitsch, C.; Vetterlein, M.; Stangl, H.; Maier, S.; Neumüller, J.; Freissmuth, M.; Pavelka, M.; Ellinger, A. *Histochem. Cell Biology* **2008**, *130*.

79. Takizawa, T.; Suzuki, K.; Robinson, J. M. *J. Histochem. Cytochem.* **1998**, *46*, 1097-1102.

80. Manning, H. C.; Goebel, T.; Marx, J. N.; Bornhop, D. J. *Organic Letters* **2002**, *4*, 1075-1078.

81. Faulkner, S.; Beeby, A.; Dickins, R. S.; Parker, D.; Williams, J. A. G. *Journal of Fluorescence* **1999**, *9*, 45-49.

82. Bünzli, J.-C. G. *Accounts of Chemical Research* **2005**, *39*, 53-61.

83. Beeby, A.; Botchway, S. W.; Clarkson, I. M.; Faulkner, S.; Parker, A. W.; Parker, D.; Williams, J. A. G. *Journal of Photochemistry and Photobiology B: Biology* **2000**, *57*, 83-89.

84. Crosby, G. A.; Whan, R. E.; Alire, R. M. *The Journal of Chemical Physics* **1961**, *34*, 743-748.

85. Smentek, L.; B. Andes Hess, J.; Cross, J. P.; Manning, H. C.; Bornhop, D. J. *The Journal of Chemical Physics* **2005**, *123*, 244302.

86. Hess, B. A.; Kędziorski, A.; Smentek, L.; Bornhop, D. J. *The Journal of Physical Chemistry A* **2008**, *112*, 2397-2407.

87. Thunus, L.; Lejeune, R. *Coordination Chemistry Reviews* **1999**, *184*, 125-155.

88. Caravan, P.; Ellison, J. J.; McMurry, T. J.; Lauffer, R. B. *Chemical Reviews* **1999**, *99*, 2293-2352.

89. Bornhop, D. J.; Griffin, J. M. M.; Goebel, T. S.; Sudduth, M. R.; Bell, B.; Motamedi, M. *Applied Spectroscopy* **2003**, *57*, 1216-1222.

90. Moore, E. G.; Samuel, A. P. S.; Raymond, K. N. *Accounts of Chemical Research* **2009**, *42*, 542-552.

91. Samuelson, L. E.; Dukes, M. J.; Hunt, C. R.; Casey, J. D.; Bornhop, D. J. *Bioconjugate Chem.* **2009**, *20*, 2082-2089.

92. Bornhop, D. J.; Hubbard, D. S.; Houlne, M. P.; Adair, C.; Kiefer, G. E.; Pence, B. C.; Morgan, D. L. *Analytical Chemistry* **1999**, *71*, 2607-2615.

93. André, J. P.; Geraldes, C. F. G. C.; Martins, J. A.; Merbach, A. E.; Prata, M. I. M.; Santos, A. C.; de Lima, J. J. P.; Tóth, É. *Chemistry – A European Journal* **2004**, *10*, 5804-5816.

94. William T. Anderson, J.; Macht, D. I. *Physiology* **1928**, *86*, 320-330.

95. Kim, S.; Lim, Y. T.; Soltesz, E. G.; De Grand, A. M.; Lee, J.; Nakayama, A.; Parker, J. A.; Mihaljevic, T.; Laurence, R. G.; Dor, D. M.; Cohn, L.

H.; Bawendi, M. G.; Frangioni, J. V. *Nature Biotechnology* **2004**, *22*, 93-97.

96. Kovacs, Z.; Sherry, A. D. *ChemInform* **1997**, *28*, no-no.

97. Chiron, J.; Galy, J.-P. *Synlett* **2003**, *2003*, 2349,2350.

98. Sevick-Muraca, E. M.; Houston, J. P.; Gurfinkel, M. *Curr. Opin. Chem. Biol.* **2002**, *6*, 642–650.

99. Emptage, N. J. *Current Opinion in Pharmacology* **2001**, *1*, 521-525.

100. Pawlicki, M.; Collins, H. A.; Denning, R. G.; Anderson, H. L. *Angewandte Chemie-International Edition* **2009**, *48*, 3244-3266.

101. Griffin, J. M. M.; Skwierawska, A. M.; Manning, H. C.; Marx, J. N.; Bornhop, D. J. *Tetrahedron Letters* **2001**, *42*, 3823-3825.

102. Gillies, E. R.; Frechet, J. M. J. *Drug Discovery Today* **2005**, *10*, 35-43.

103. Esfand, R.; Tomalia, D. A. *Drug Discovery Today* **2001**, *6*, 427-436.

104. Kitchens, K. M.; Kolhatkar, R. B.; Swaan, P. W.; Eddington, N. D.; Ghandehari, H. *Pharmaceutical Research* **2006**, *23*, 2818-2826.

105. Klajnert, B.; Pastucha, A.; Shcharbin, D.; Bryszewska, M. *J Appl Polym Sci* **2007**, *103*, 2036-2040.

106. Eichman, J. D.; Bielinska, A. U.; Kukowska-Latallo, J. F.; James R. Baker, J. *PSTT* **2000**, *3*, 232-245.

107. Papadopoulos, V.; Baraldi, M.; Guilarte, T. R.; Knudsen, T. B.; Lacapere, J. J.; Lindemann, P.; Norenberg, M. D.; Nutt, D.; Weizman, A.; Zhang, M. R.; Gavish, M. *Trends Pharmacol Sci* **2006**, *27*, 402-409.

108. Gavish, M.; Bachman, I.; Shoukrun, R.; Katz, Y.; Veenman, L.; Weisinger, G.; Weizman, A. *Pharmacol Rev* **1999**, *51*, 629-650.

109. Maeda, J.; Suhara, T.; Zhang, M. R.; Okauchi, T.; Yasuno, F.; Ikoma, Y.; Inaji, M.; Nagai, Y.; Takano, A.; Obayashi, S.; Suzuki, K. *Synapse* **2004**, *52*, 283-291.

110. Papadopoulos, V.; Lecanu, L.; Brown, R. C.; Han, Z.; Yao, Z. X. *Neuroscience* **2006**, *138*, 749-756.

111. Bai, M.; Wyatt, S. K.; Han, Z.; Papadopoulos, V.; Bornhop, D. J. *Bioconjugate Chem.* **2007**, *18*, 1118-1122.

112. Strable, E.; Bulte, J. W. M.; Moskowitz, B.; Vivekanandan, K.; Allen, M.; Douglas, T. *Chemistry of Materials* **2001**, *13*, 2201-2209.

113. Glauert, A. M.; Lewis, P. R. In *Biological Specimen Preparation for Trnasmission Electron Microscopy*, Glauert, A. M., Ed.; Princeton University Press: Princeton, 1998; Vol. 17, p 55-63.

114. Hell, S. W. *Science* **2007**, *316*, 1153-1158.

115. Stahlberg, H.; Waltz, T. *ACS Chem. Biol.* **2008**, *3*, 268-281.

116. Sun, M. G.; Williams, J.; Munoz-Pinedo, C.; Perkins, G. A.; Browns, J. M.; Ellisman, M. H.; Green, D. R.; Frey, T. G. *Nature Cell Biology* **2007**, *09*, 1057-1065.

117. Pombo, A.; Hollinshead, M.; Cook, P. R. *The Journal of Histochemistry & Cytochemistry* **1999**, *47*, 471-480.

118. Gaietta, G. M.; Giepmans, B. N. G.; Deerinck, T. J.; Smith, W. B.; Ngan, L.; Llopis, J.; Adams, S. R.; Tsien, R. Y.; Ellisman, M. H. *PNAS* **2006**, *103*
17777-17782.

119. Grabenbauer, M.; Geerts, W. J.; Fernadez-Rodriguez, J.; Hoenger, A.; Koster, A. J.; Nilsson, T. *Nat. Methods* **2005**, *2*, 857-862.

120. Peckys, D. B.; Veith, G. M.; Joy, D. C.; de Jonge, N. *PLoS ONE* **2009**, *4*, e8214.

121. Lidke, D. S.; Nagy, P.; Arndt-Jovin, D. J. *Current Protocols in Cell Biology Suppl. 36* **2007**, *25*, 1-25.

122. Barth, J. E.; Kruit, P. *Optik* **1996**, *101*, 101-109.

123. Lidke, D. S.; Nagy, P.; Heintzmann, R.; Arndt-Jovin, D. J.; Post, J. N.; Grecco, H. E.; Jares-Erijman, E. A.; Jovin, T. M. *Nature Biotechnology* **2004**, *22*, 198-203.

124. McKanna, J. A.; Haigler, H. T.; Cohen, S. *Proc. Natl. Acad. Sci.* **1979**, *76*, 5689-5693.

125. J. Boonstra; P. van Maurik; L.H. Defize; Laat, S. W. d.; J.L., L.; Verkley, A. J. *Eur. J. Cell Biol.* **1985**, *36*, 209– 216

126. Jonge, N. d.; Poirier-Demers, N.; Peckys, D. B.; Drouin, D. *Ultramicroscopy* **2010**, *110*, 1114-1119.

127. Keene, D. R.; Tufa, S. F.; Lunstrum, G. P.; Holden, P.; A., H. W. *Microscopy and Microanalysis* **2008**, *14*, 342-348.

128. Yu, W. W.; Qu, L.; Guo, W.; Peng, X. *Chemistry of Materials* **2003**, *15*, 2854-2860.

129. Reimer, L. *Transmission Electron Microscopy*; Springer: Heidelberg, 1984.

130. Lee, B.; Kim, Y.; Lee, S.; Kim, Youn S.; Wang, D.; Cho, J. *Angewandte Chemie International Edition, 49*, 359-363.

131. Reimer, L. *Scanning Electron Microscopy, Physics of Image Formation and Microanalysis*; Springer: Heidelberg, 1985.

132. Rose, A. *Adv. Electron.* **1948**, *1*, 131-166.

133. Iancu, C. V.; Wright, E. R.; Heymann, J. B.; Jenson, G. J. A. *J. Struct. Biol.* **2006**, *153*, 231-240.

134. Luther, P. K.; Lawrence, M. C.; Crowther, R. A. A. *Ultramicroscopy* **1988**, *24*, 7-18.

135. Tkachenko, A. G.; Xie, H.; Liu, Y. L.; Coleman, D.; Ryan, J.; Glomm, W. R.; Shipton, M. K.; Franzen, S.; Feldheim, D. L. *Bioconjugate Chem.* **2004**, *15*, 482-490.

136. Toyokuni, T.; Walsh, J. C.; Dominguez, A.; Phelps, M. E.; Barrio, J. R.; Gambhir, S. S.; Satyamurthy, N. *Bioconjugate Chem.* **2003**, *14*, 1253-1259.

137. Hohmann-Marriott, M. F.; Sousa, A. A.; Azari, A. A.; Glushakova, S.; Zhang, G.; Zimmerberg, J.; Leapman, R. D. *Nat Meth* **2009**, *6*, 729-731.

138. Resch, G. P.; Urban, E.; Jacob, S. In *Methods in Cell Biology*; Thomas, M.-R., Ed.; Academic Press: 2010; Vol. Volume 96, p 529-564.

139. Benthem, K. v.; Lupini, A. R.; Kim, M.; Baik, H. S.; Doh, S.; Lee, J.-H.; Oxley, M. P.; Findlay, S. D.; Allen, L. J.; Luck, J. T.; Pennycook, S. J. *Applied Physics Letters* **2005**, *87*, 034104.

140. Nagata, T. *Micron* **2000**, *32*, 387-404.

141. Rasband, W. S.; U.S. National Institute of Health: Bethesda, Maryland, USA, 1997-2005.

142. Meijering, E. 1996, p ImageJ Plugin.

143. de Jonge, N.; Dukes, M.; Ring, E.; Drouin, D.; Peckys, D. *Microscopy and Microanalysis* **2010**, *16*, 328-329.

144. Willingham, M. C.; Pastan, I. H. *The Journal of Cell Biology* **1982**, *94*, 207-212.

145. Schlessinger, J.; Shechter, Y.; Willingham, M. C.; Pastan, I. *Proceedings of the National Academy of Sciences of the United States of America* **1978**, *75*, 2659-2663.

146. Schreiber, A. B.; Libermann, T. A.; Lax, I.; Yarden, Y.; Schlessinger, J. *Journal of Biological Chemistry* **1983**, *258*, 846-853.

147. Leamon, C. P.; Pastan, I.; Low, P. S. *Journal of Biological Chemistry* **1993**, *268*, 24847-24854.

148. Jackowski, M. M.; Swift, L. L.; Cohen, S.; McKanna, J. A. *Journal of Cellular Physiology* **1990**, *142*, 458-468.

149. Kurokawa, K.; Matsuda, M. *Mol. Biol. Cell* **2005**, *16*, 4294-4303.

150. Ridley, A. J. *BioEssays* **1994**, *16*, 321-327.

151. Brunk, U.; Schellens, J.; Westermark, B. *Experimental Cell Research* **1976**, *103*, 295-302.

152. Chinkers, M.; McKanna, J. A.; Cohen, S. *J. Cell Biol.* **1979**, *83*, 260-265.

153. Agarwal, A.; Asthana, A.; Gupta, U.; Jain, N. K. *Journal of Pharmacy and Pharmacology* **2008**, *60*, 671-688.

154. Jevprasesphant, R.; Penny, J.; Attwood, D.; D'Emanuele, A. *Journal of Controlled Release* **2004**, *97*, 259-267.

155. Kasotakis, E.; Mossou, E.; Adler-Abramovich, L.; Mitchell, E. P.; Forsyth, V. T.; Gazit, E.; Mitraki, A. *Biopolymers* **2009**, *92*, 164-172.

156. Manning, C. H.; Bornhop, D. J.; Goebel, T. In *WO03020701* USA, 2003.

157. Peckys, D. B.; de Jonge, N. *Nano Letters* **2011**, null-null.

158. Hardwick, M.; Fertikh, D.; Culty, M.; Li, H.; Vidic, B.; Papadopoulos, V. *Cancer Research* **1999**, *59*, 831-842.

159. Yu, C. X.; Hale, J.; Ritchie, K.; Prasad, N. K.; Irudayaraj, J. *Biochemical and Biophysical Research Communications* **2009**, *378*, 376-382.

160. Jerome, W. G.; Yancey, P. G. *Microscopy and Microanalysis* **2003**, *9*, 54-67.

161. Jerome, W. G.; Cox, B. E.; Griffin, E. E.; Ullery, J. C. *Microscopy and Microanalysis* **2008**, *14*, 138-149.

162. Frens, G. *Nature-Physical Science* **1973**, *241*, 20-22.

163. Handley, D. A.; Arbeeny, C. M.; Witte, L. D.; Chien, S. *Proceedings of the National Academy of Sciences of the United States of America-Biological Sciences* **1981**, *78*, 368-371.

164. Möbius, W.; Van Donselaar, E.; Ohno-Iwashita, Y.; Shimada, Y.; Heijnen, H. F. G.; Slot, J. W.; Geuze, H. J. *Traffic* **2003**, *4*, 222-231.

165. Kremer, J. R.; Mastronarde, D. N.; McIntosh, J. R. *Journal of Structural Biology* **1996**, *116*, 71-76.

166. Ciarlo, D. R. *Biomedical Microdevices* **2002**, *4*, 63-68.

167. Williamson, M. J.; Tromp, R. M.; Vereecken, P. M.; Hull, R.; Ross, F. M. *Nat Mater* **2003**, *2*, 532-536.

168. Nishiyama, H.; Suga, M.; Ogura, T.; Maruyama, Y.; Koizumi, M.; Mio, K.; Kitamura, S.; Sato, C. *Journal of Structural Biology* **2010**, *169*, 438-449.

169. Dukes, M. J.; Peckys, D. B.; de Jonge, N. *Acs Nano* **2010**, *4*, 4110-4116.

170. Gaietta, G.; Deerinck, T. J.; Adams, S. R.; Bouwer, J.; Tour, O.; Laird, D. W.; Sosinsky, G. E.; Tsien, R. Y.; Ellisman, M. H. *Science* **2002**, *296*, 503-507.

171. Creemer, J. F.; Helveg, S.; Kooyman, P. J.; Molenbroek, A. M.; Zandbergen, H. W.; Sarro, P. M. *Microelectromechanical Systems, Journal of* **2010**, *19*, 254-264.

172. Satulovsky, J.; Lui, R.; Wang, Y.-l. *Biophysical Journal* **2008**, *94*, 3671-3683.

173. Ring, E. A.; de Jonge, N. *Microscopy and Microanalysis* **2010**, *16*, 622-629.

174. Grant, A. W.; et al. *Nanotechnology* **2004**, *15*, 1175.

175. Ibaraki, N.; Lin, L.-R.; Reddy, V. N. *Experimental Eye Research* **1996**, *63*, 683-692.

176. Driskell, O. J.; Mironov, A.; Allan, V. J.; Woodman, P. G. *Nat Cell Biol* **2007**, *9*, 113-120.

177. Hosoi, J.; Hama, K.; Kosaka, T. *Journal of Electron Microscopy* **1981**, *30*, 57-62.

178. Lidke, D. S.; Lidke, K. A.; Rieger, B.; Jovin, T. M.; Arndt-Jovin, D. J. *J. Cell Biol.* **2005**, *170*, 619-626.

179. Agronskaia, A.; Valentijn, J.; van Driel, L.; Schneijdenberg, C.; Humbel, B.; van Bergen en Henegouwen, P.; Verkleij, A.; Koster, A.; Gerritsen, H. *Journal of Structural Biology* **2008**, *164*, 183-189.

180. Klein, K. L.; Anderson, I. M.; De Jonge, N. *Journal of Microscopy* **2011**, no-no.